Universidad de Oviedo

Tesis Doctoral

Programa de Doctorado en Energía y Control de Procesos

ESTUDIO AEROELÁSTICO DE SEGUIDORES SOLARES DE UN SOLO EJE

Doctorando:

Eva Martínez García

Oviedo, a 25 de octubre del 2024

Universidad de Oviedo

Departamento de Energía

Tesis Doctoral

Programa de Doctorado en Energía y Control de Procesos

ESTUDIO AEROELÁSTICO DE SEGUIDORES SOLARES DE UN SOLO EJE

Doctoranda:

Eva Martínez García

Directores de tesis: Dr. Eduardo Blanco Marigorta

Dr. Antonio Navarro Manso

Oviedo, a 25 de octubre del 2024

RESUMEN DEL CONTENIDO DE TESIS DOCTORAL

1.- Título de la Tesis	
Español/Otro Idioma: ESTUDIO AEROELÁSTICO DE SEGUIDORES SOLARES DE UN SOLO EJE	Inglés: AEROELASTIC STUDY OF SINGLE AXIS SOLAR TRACKERS

2.- Autor	
Nombre: Eva Martínez García	
Programa de Doctorado: Energía y Control de Procesos	
Órgano responsable: Centro Internacional de postgrado	

RESUMEN en español (máximo 4000 caracteres)

El sector de las energías renovables, en particular de la solar de seguimiento a gran escala, ha experimentado un crecimiento exponencial en los últimos 15 años. La deslocalización de la producción en países fuera de la unión europea ha producido un incremento en la competitividad por el abaratamiento de costes de instalación y producción de la tecnología solares de seguimiento. La consecuencia más directa de este hecho tiene es la aparición de estructuras más ligeras y esbeltas en el mercado que favorecen el mayor LCOE de todas las tipologías renovables en el mercado.

Los seguidores solares monoeje, son estructuras sencillas constituidas por un eje de gran longitud fijado al suelo por varios pilares equidistantes. En su centro se sitúa un moto-reductora que da capacidad de giro a dicho eje. Sobre el eje, arriostradas a é, se encuentran las placas solares que capturan la energía de la radiación solar durante todo el día. Este tipo de estructuras sólo tienen una posibilidad mejorar su rentabilidad, aumentando la superficie de captación y reduciendo la inercia (o cantidad de acero) de la sección que sostiene las placas solares. El resultado directo son estructuras muy ligeras con facilidad para sufrir efectos dinámicos derivados, principalmente, de su interacción con el viento.

Esta tesis aborda el problema que en la actualidad acucia a las plantas solares a gran escala, las inestabilidades torsionales originadas por la interacción de viento y estructura, y que provoca el fallo o colapso de la misma. Mediante la creación de modelos completos 3D, se indaga sobre los parámetros que influyen en la aparición de los fenómenos aeroelásticos, se analizan y estudian qué fenómenos de interacción fluido-estructura se dan, y se define una metodología de estudio y diseño para predecir las velocidades de viento límite que soportará la estructura. Los ensayos experimentales se han llevado a cabo en túnel de viento de cámara abierta, con velocidades desde 2 m/s hasta 50 m/s. Los modelos a escala para los ensayos, se han construido mediante fabricación aditiva.

Se ha estudiado la influencia de parámetros estructurales y dimensionales como la inercia y la relación de aspecto, en la respuesta dinámica a la inestabilidad torsional. Se ha descrito por primera vez un Diagrama de estabilidad, que es una herramienta fiable para ayudar al diseño de seguidores solares estables ante los efectos del viento. En ellos se identifican los ángulos de inclinación del seguidor solar y la velocidad crítica de viento que son capaces de soportar sin sufrir oscilaciones.

Se han identificado varios fenómenos aeroelásticos que aparecen en la estructura solar, derivados de la acción del viento. El principal y más dañino es el galope torsional. A él se deben las imágenes de filas enteras de seguidores solares oscilando intensamente hasta que son arrancados. El viento incidente, provoca una torsión en el eje del seguidor que inicia un aleteo de la superficie solar, éste aleteo se amplifica por su interacción continuada con el viento, dando lugar a desplazamientos radiales de las placas solares que aumentan su amplitud. En muchas de las situaciones, este fenómeno de galope torsional aparece súbitamente, pero en otras es precedido de otro fenómeno aeroelástico llamado vibración inducida por vórtices. En este caso, y para pequeños ángulos de inclinación y varias filas consecutivas de seguidores, aparece una pequeña vibración debido a la sincronización de la frecuencia de desprendimiento de vórtices, en los extremos superior e inferior de la placa solar, con la frecuencia natural de la estructura. Esto ocasiona la aparición de una resonancia fluido-estructura que da lugar inestabilidad aeroelástica.

Por último, se construye un modelo estructural para ensayo en túnel de viento y que proporciona una metodología genérica de creación de modelos de seguidores solares y cómo ensayarlos para poder obtener el diagrama de estabilidad que permita extrapolar a un prototipo real los resultados obtenidos en túnel de viento. Además, se valida por pares mediante la replica de la metodología en túnel de viento de otra universidad con otro equipo de investigación.

En estadios iniciales de esta tesis, se crean modelos numéricos estáticos con mecánica de fluidos computacional (CFD), pero una ampliación y exploración profunda de las posibilidades que estos modelos ofrecen, debe ser explorada en trabajos posteriores.

RESUMEN en inglés

The renewable energy sector, particularly large-scale solar tracking, has experienced exponential growth over the past 15 years. The relocation of production to countries outside the European Union has increased competitiveness by lowering installation and production costs of solar tracking technologies. The most immediate consequence of this phenomenon is the emergence of lighter, more streamlined structures in the market, which contribute to the highest LCOE (Levelized Cost of Energy) among all renewable types in the market.

Single-axis solar trackers are simple structures comprised of a long axis anchored to the ground by several equidistant pillars. At its centre, a motor-reducer enables the rotation of this axis. Solar panels, braced to the axis, capture solar radiation throughout the day. This type of structure has only one way to enhance its profitability: by increasing the collection surface and reducing the inertia (or amount of steel) of the section that supports the solar panels. This results directly in very lightweight structures susceptible to dynamic effects, mainly due to their interaction with wind.

This thesis addresses the pressing problem faced by large-scale solar plants: torsional instabilities caused by wind-structure interactions, which lead to structural failure or collapse. Through the development of complete 3D models, the study investigates parameters influencing aeroelastic phenomena, analyses and examines fluid-structure interaction mechanisms, and establishes a study and design methodology to predict the wind speed limits the structure can withstand. Experimental tests were conducted in an open-jet wind tunnel, with wind speeds ranging from 2 m/s to 50 m/s. Scale models for the tests were constructed through additive manufacturing.

The influence of structural and dimensional parameters, such as inertia and aspect ratio, on dynamic response to torsional instability has been studied. For the first time, a Stability Diagram has been described as a reliable tool to aid in the design of wind-stable solar trackers. This diagram identifies the inclination angles and critical wind speeds solar trackers can withstand without oscillation.

Several aeroelastic phenomena induced by wind action have been identified in solar tracker structures. The most significant and damaging phenomenon is torsional galloping, which explains the images of entire rows of solar trackers oscillating intensely until being torn apart. Incident wind causes torsion on the tracker’s axis, initiating a flapping motion of the solar surface; this flapping is amplified by continuous interaction with the wind, resulting in radial displacements of the solar panels that increase in amplitude. In many cases, this torsional galloping occurs suddenly, though it may also be preceded by another aeroelastic phenomenon known as vortex-induced vibration. In this case, and with small inclination angles and multiple consecutive rows of trackers, a slight vibration occurs due to the synchronization of vortex shedding frequencies at the top and bottom edges of the solar panel with the natural frequency of the structure. This results in a fluid-structure resonance, leading to aeroelastic instability.

Finally, a structural model was constructed for wind tunnel testing, providing a generic methodology for creating and testing solar tracker models to obtain stability diagrams that allow results from the wind tunnel to be extrapolated to a real prototype. Additionally, this methodology was validated by replication in a wind tunnel study at another university with a different research team.

In the early stages of this thesis, static numerical models were created using computational fluid dynamics (CFD). However, a more extensive exploration of the potential these models offer remains an avenue for future research.

SR. PRESIDENTE DE LA COMISIÓN ACADÉMICA DEL PROGRAMA DE DOCTORADO EN ENERGÍA Y CONTROL DE PROCESOS

A mis padres, Antonio y Gloria.

AGRADECIMIENTOS

En primer lugar, quiero agradecer de corazón mi director de tesis Eduardo Blanco Marigorta, por adoptarme bajo su tutela y con su característica paciencia, enseñarme y orientarme, escuchando mis divagaciones y guiándome por la vía correcta. Gracias por tu ayuda y confianza.

A mi amado compañero de vida, Juan Pedro, que me ha motivado a conseguir este hito desde el mismo día en que me conoció.

A mis compañeros de laboratorio con los que coincidí durante mi estancia en Asturias y quienes me brindaron momentos de amistad y compañerismo, Ahmed Gharib y Andrés Meana. Allá donde estéis seréis queridos y valorados.

Por último, quiero extender mis agradecimientos a los técnicos de laboratorio Fran y Charo, que siempre me asistieron con amistad, cariño y una sonrisa.

Tabla de contenidos

Resumen

El sector de las energías renovables, en particular de la solar de seguimiento a gran escala, ha experimentado un crecimiento exponencial en los últimos 15 años. La deslocalización de la producción en países fuera de la unión europea ha producido un incremento en la competitividad por el abaratamiento de costes de instalación y producción de la tecnología solares de seguimiento. La consecuencia más directa de este hecho tiene es la aparición de estructuras más ligeras y esbeltas en el mercado que favorecen el mayor LCOE de todas las tipologías renovables en el mercado.

Los seguidores solares monoeje, son estructuras sencillas constituidas por un eje de gran longitud fijado al suelo por varios pilares equidistantes. En su centro se sitúa un moto-reductora que da capacidad de giro a dicho eje. Sobre el eje, arriostradas a é, se encuentran las placas solares que capturan la energía de la radiación solar durante todo el día. Este tipo de estructuras sólo tienen una posibilidad mejorar su rentabilidad, aumentando la superficie de captación y reduciendo la inercia (o cantidad de acero) de la sección que sostiene las placas solares. El resultado directo son estructuras muy ligeras con facilidad para sufrir efectos dinámicos derivados, principalmente, de su interacción con el viento.

Esta tesis aborda el problema que en la actualidad acucia a las plantas solares a gran escala, las inestabilidades torsionales originadas por la interacción de viento y estructura, y que provoca el fallo o colapso de la misma. Mediante la creación de modelos completos 3D, se indaga sobre los parámetros que influyen en la aparición de los fenómenos aeroelásticos, se analizan y estudian qué fenómenos de interacción fluido-estructura se dan, y se define una metodología de estudio y diseño para predecir las velocidades de viento límite que soportará la estructura. Los ensayos experimentales se han llevado a cabo en túnel de viento de cámara abierta, con velocidades desde 2 m/s hasta 50 m/s. Los modelos a escala para los ensayos, se han construido mediante fabricación aditiva.

Se ha estudiado la influencia de parámetros estructurales y dimensionales como la inercia y la relación de aspecto, en la respuesta dinámica a la inestabilidad torsional. Se ha descrito por primera vez un Diagrama de estabilidad, que es una herramienta fiable para ayudar al diseño de seguidores solares estables ante los efectos del viento. En ellos se identifican los ángulos de inclinación del seguidor solar y la velocidad crítica de viento que son capaces de soportar sin sufrir oscilaciones.

Se han identificado varios fenómenos aeroelásticos que aparecen en la estructura solar, derivados de la acción del viento. El principal y más dañino es el galope torsional. A él se deben las imágenes de filas enteras de seguidores solares oscilando intensamente hasta que son arrancados. El viento incidente, provoca una torsión en el eje del seguidor que inicia un aleteo de la superficie solar, éste aleteo se amplifica por su interacción continuada con el viento, dando lugar a desplazamientos radiales de las placas solares que aumentan su amplitud. En muchas de las situaciones, este fenómeno de galope torsional aparece súbitamente, pero en otras es precedido de otro fenómeno aeroelástico llamado vibración inducida por vórtices. En este caso, y para pequeños ángulos de inclinación y varias filas consecutivas de seguidores, aparece una pequeña vibración debido a la sincronización de la frecuencia de desprendimiento de vórtices, en los extremos superior e inferior de la placa solar, con la frecuencia natural de la estructura. Esto ocasiona la aparición de una resonancia fluido-estructura que da lugar inestabilidad aeroelástica.

Por último, se ha construido un modelo estructural para ensayo en túnel de viento y que proporciona una metodología genérica de creación de modelos de seguidores solares y

cómo ensayarlos para poder obtener el diagrama de estabilidad que permita extrapolar a un prototipo real los resultados obtenidos en túnel de viento. Además, se valida por pares mediante la réplica de la metodología en túnel de viento de otra universidad con otro equipo de investigación.

En estadios iniciales de esta tesis, se han creado modelos numéricos estáticos con mecánica de fluidos computacional (CFD), que han permitido mejorar el conocimiento de los fenómenos implicados. Aunque no se ha profundizado en ellos, se prevé que pueden ser una herramienta fundamental en estudios posteriores

Abstract

The renewable energy sector, particularly large-scale solar tracking, has experienced exponential growth over the past 15 years. The relocation of production to countries outside the European Union has increased competitiveness by lowering installation and production costs of solar tracking technologies. The most immediate consequence of this phenomenon is the emergence of lighter, more streamlined structures in the market, which contribute to the highest LCOE (Levelized Cost of Energy) among all renewable types in the market.

Single-axis solar trackers are simple structures comprised of a long axis anchored to the ground by several equidistant pillars. At its centre, a motor-reducer enables the rotation of this axis. Solar panels, braced to the axis, capture solar radiation throughout the day. This type of structure has only one way to enhance its profitability: by increasing the collection surface and reducing the inertia (or amount of steel) of the section that supports the solar panels. This results directly in very lightweight structures susceptible to dynamic effects, mainly due to their interaction with wind.

This thesis addresses the pressing problem faced by large-scale solar plants: torsional instabilities caused by wind-structure interactions, which lead to structural failure or collapse. Through the development of complete 3D models, the study investigates parameters influencing aeroelastic phenomena, analyses and examines fluid-structure interaction mechanisms, and establishes a study and design methodology to predict the wind speed limits the structure can withstand. Experimental tests were conducted in an open-jet wind tunnel, with wind speeds ranging from 2 m/s to 50 m/s. Scale models for the tests were constructed through additive manufacturing.

The influence of structural and dimensional parameters, such as inertia and aspect ratio, on dynamic response to torsional instability has been studied. For the first time, a Stability Diagram has been described as a reliable tool to aid in the design of wind-stable solar trackers. This diagram identifies the inclination angles and critical wind speeds solar trackers can withstand without oscillation.

Several aeroelastic phenomena induced by wind action have been identified in solar tracker structures. The most significant and damaging phenomenon is torsional galloping, which explains the images of entire rows of solar trackers oscillating intensely until being torn apart. Incident wind causes torsion on the tracker’s axis, initiating a flapping motion of the solar surface; this flapping is amplified by continuous interaction with the wind, resulting in radial displacements of the solar panels that increase in amplitude. In many cases, this torsional galloping occurs suddenly, though it may also be preceded by another aeroelastic phenomenon known as vortex-induced vibration. In this case, and with small inclination angles and multiple consecutive rows of trackers, a slight vibration occurs due to the synchronization of vortex shedding frequencies at the top and bottom edges of the solar panel with the natural frequency of the structure. This results in a fluid-structure resonance, leading to aeroelastic instability.

Finally, a structural model was constructed for wind tunnel testing, providing a generic methodology for creating and testing solar tracker models to obtain stability diagrams that allow results from the wind tunnel to be extrapolated to a real prototype. Additionally, this methodology was validated by replication in a wind tunnel study at another university with a different research team.

In the early stages of this thesis, static numerical models were created using computational fluid dynamics (CFD), that have allowed us to improve our knowledge of the phenomena

involved. Although they have not been studied in depth, it is foreseen that they may be a fundamental tool in subsequent studies.

ESTUDIO AEROELÁSTICO DE SEGUIDORES SOLARES DE UN SOLO EJE

Introducción

Un futuro sostenible, en el que prevalezca la seguridad energética y se abogue por la conservación del planeta, en el que se creen apliquen políticas que fomenten un uso responsable de los recursos existentes, es un gran reto al que se enfrentan los gobiernos, la comunidad científica y el resto de los seres humanos.

La Asamblea General de las Naciones Unidas adoptó en 2015 la agenda 2030 para el desarrollo sostenible. Se basa en 17 objetivos encaminados a lograr ese desarrollo de todos los pueblos y naciones del planeta. En particular, los objetivos 7 (Energía Asequible y no Contaminante), 11 (Ciudades y Comunidades Sostenibles), 12 (Producción y consumos responsables), están más enfocados hacia la producción energética (limpia) y su consumo, de una forma responsable y garante de la durabilidad de los recursos para generaciones venideras (esto es sostenibilidad).

Figura 1. Principales Objetivos de Desarrollo Sostenibles relacionados con la producción energética sostenible.

Señalada la relevancia de la seguridad energética, fundamental para prevenir enfermedades y luchar contra pandemias, cada país estructura su *pull* energético en base a sus recursos naturales y sus capacidades de compra. Las principales fuentes de energía renovables son 3: viento, agua, radiación solar. En función de las características geofísicas y la abundancia de estos tres recursos (simultáneamente) en su territorio, los países fomentan políticas para instalar tecnologías que sean capaces de extraer el mayor rendimiento posible a esos recursos.

Es por ello, que muchos países poseen un mercado de producción eléctrica con una importante contribución renovable, constituida por distintos tipos de tecnología: eólica, solar fotovoltaica, hidráulica, biogás, o biomasa.

En la conferencia sobre el cambio climático COP28 (2023) celebrada en Dubai, más de 130 gobiernos nacionales, incluida la Unión Europea, acordaron colaborar para triplicar la capacidad mundial instalada de energías renovables hasta alcanzar al menos 11 000 GW en 2030.

Marcando de este modo las tendencias políticas que impulsan el despliegue, la fabricación de energía solar fotovoltaica, la competitividad de las tecnologías renovables, el almacenamiento de energía y la capacidad de energía renovable para la producción de hidrógeno. En 2023, la energía solar fotovoltaica representará por sí sola las tres cuartas partes de la potencia renovable añadida en todo el mundo.

En los próximos cinco años se espera que sigan aumentando las adiciones de capacidad de energía renovable, y la solar fotovoltaica y la eólica representarán un récord del 96% de ellas, porque sus costes de generación son más bajos que los de las alternativas fósiles y no fósiles en la mayoría de los países y las políticas siguen apoyándolas.

La consultora Wood Mackenzie afirma que la industria solar ha alcanzado una nueva etapa en su evolución y prevé alrededor de 350 GW anuales de instalaciones solares en todo el mundo durante los próximos ocho años. La empresa de investigación también pronostica retos para el sector de la fabricación solar y los tan esperados beneficios de la Ley de Reducción de la Inflación en Estados Unidos.

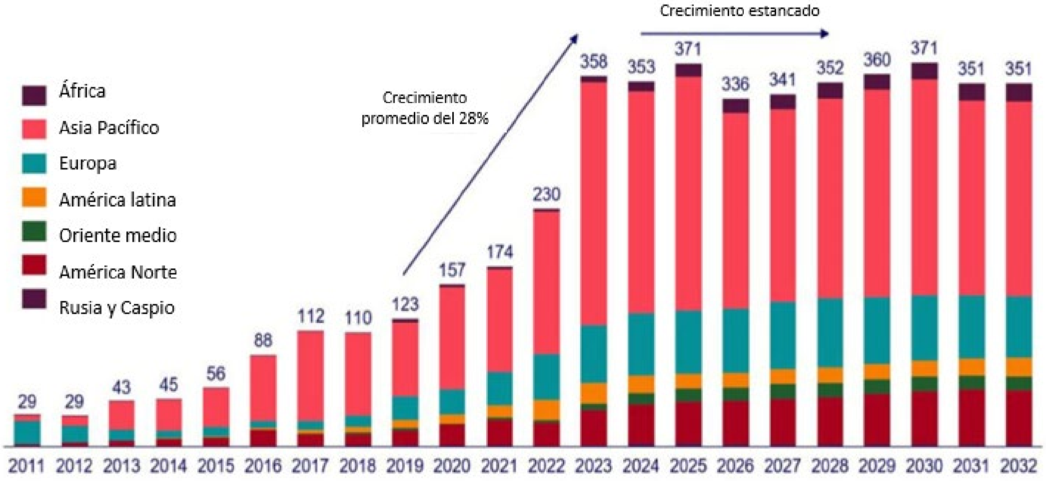

Figura 2. Estimación del crecimiento de la potencia solar instalada anual durante los próximos ocho años.

Se prevé que el crecimiento medio anual será plano durante los próximos ocho años, rompiendo una tendencia de rápido crecimiento durante la última década. Entre 2024 y 2032, se espera que las instalaciones solares mundiales alcancen una media de 350 GW cada año, alcanzando un máximo de 371 GW de energía solar instalada en 2025 y 2030.

El caso de la energía solar, es un recurso muy abundante en la mayoría del planeta. La Figura 3, muestra la radiación solar media anual de la tierra, expresada en kilovatios hora por cada kilovatio pico (kWh/kWp), que es al valor medio de las horas diarias efectivas de aprovechamiento.

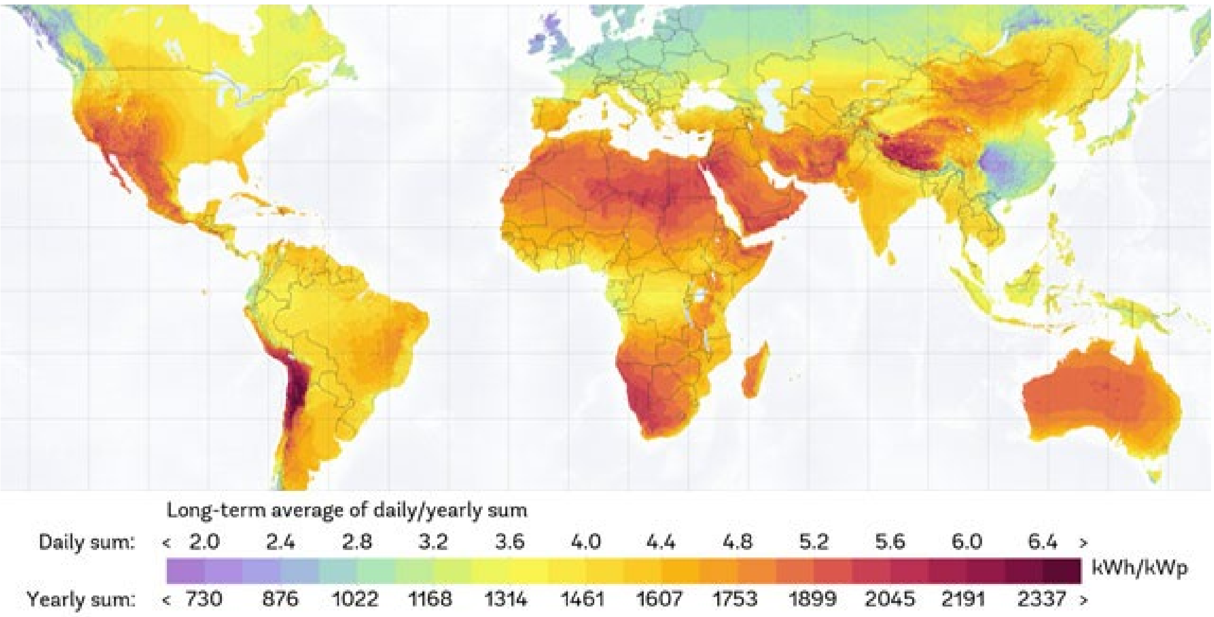

Figura 3. Distribución de la radiación solar por unidad de superficie y valor máximo de producción potencia efectiva

Una mejora de los procesos de fabricación y el abaratamiento notable de los procesos de los materiales básicos, así como creación de diseños innovadores para estructuras de captación solar, consiguen seguidores solares que aprovechan al máximo la eficiencia de la superficie de captación, y la reducción del material en la construcción de las mismas. Esta metodología de mejora del sistema de producción consigue una reducción del LCOE, conocido como *Levelized Cost of Energy* (coste energético nivelado en castellano). El LCOE es un parámetro desarrollado para calcular el coste por kilovatio hora para cada tipo de tecnología energética destinada a la generación eléctrica. Este parámetro, tienen en cuenta para su cálculo todos los costes que tiene cada sistema de generación a lo largo de su vida útil (inversiones, combustible, emisiones, operación y mantenimiento, desmantelamiento...) y lo divide entre la producción de energía total, para posteriormente, actualizarlo al valor presente. Finalmente, devuelve una métrica del coste por kilovatio hora. A través de este cálculo podemos comparar los costes de todas las tecnologías de generación energética con un solo dato, y encontrar las tecnologías más eficientes para cada región.

La tecnología de producción eólica, junto con las instalaciones de campos solares, son las más rentables actualmente. Como ventaja significativa, no son dependientes de la evolución de las materias primas (recursos fósiles o nucleares), aspecto que aporta estabilidad a la rentabilidad de las generadoras.

Si se analiza detalladamente la Figura 4, se aprecia que la tecnología solar de seguimiento, en los últimos 15 años, mejora su LCOE de 300 $/MWh a 45.5 $MWh, posicionándose la producción de campos de seguidores solares a gran escala, como la energía más barata de producir. Seguida por la solar fotovoltaica fija y la Eólica *onshore*

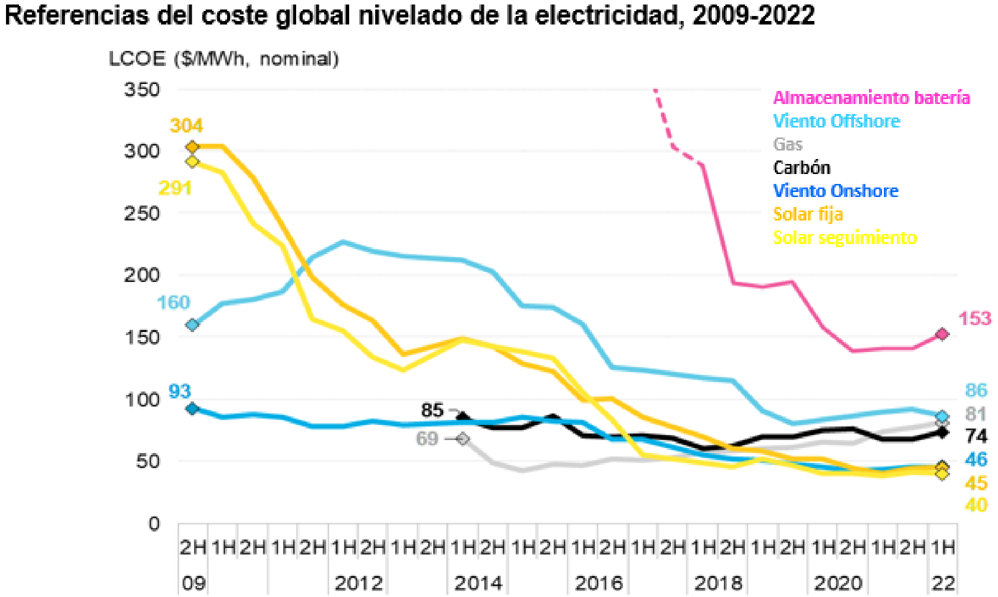

Referencias del coste global nivelado de la electricidad, 2009-2022

Fuente: BloombergNEF. Nota: Las referencias globales para PV, viento y almacenamiento son un promedio anual por país usando los valores de las últimas adiciones de capacidad. El LCOE de almacenamiento es para un sistema de almacenamiento de Li-ion a gran escala de 4 hrs de duración por ciclo diario e incluye los costes de carga.

Figura 4. Estado de la tendencia del LOCE por tipo de vector energético, 2009-2022. Fuente propia basada en previsión de Bloomberg NEF (2023).

Particularizando en la energía solar fotovoltaica, se puede establecer una clasificación general en base a los tipos de estructuras existentes en el mercado, recogida en la Figura 5.

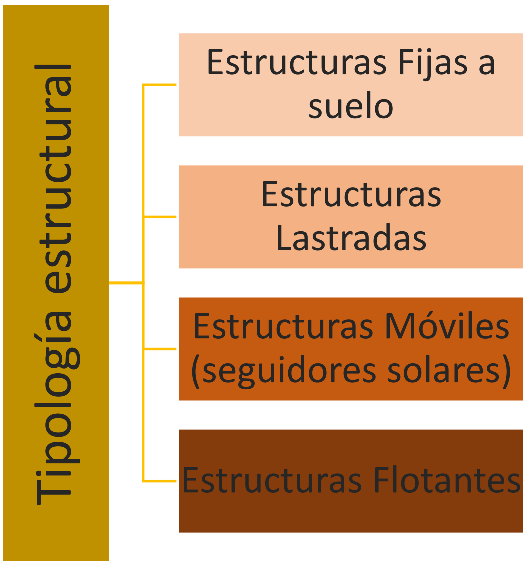

Figura 5. Tipologías estructurales para instalaciones solares fotovoltaicas.

La Tecnología solar fotovoltaica de seguimiento a escala industrial, es la más apropiada para constituir el mercado energético actual. El diseño estructural de los seguidores solares, juega un papel muy importante en la LCOE, ya que optimiza la cantidad de material empleado en su fabricación y por tanto reduce el coste estructural.

En particular, destacan los seguidores solares fotovoltaicos de monoeje, capaces de aumentar la eficiencia de captación entre el 10% y el 30% respecto a los paneles fijos. Dependiendo, por supuesto, de las condiciones geográficas y climáticas específicas del lugar de instalación (B, A. et al, 2017; K, M.et al, 2011; L, M. et al, 2011).

La disposición estructural de estos seguidores solares consiste en varios paneles solares alineados sobre un eje de torsión. El tubo de torsión está soportado por varios pilares que sólo permiten el movimiento de rotación. Un extremo del eje está libre, y el otro está fijado a un motorreductor (driver) que controla la posición angular. Normalmente, estas estructuras son simétricas respecto al conductor, con una fila de paneles a cada lado. La Figura 6 muestra un ejemplo de esquema estructural para este tipo de seguidor solar.

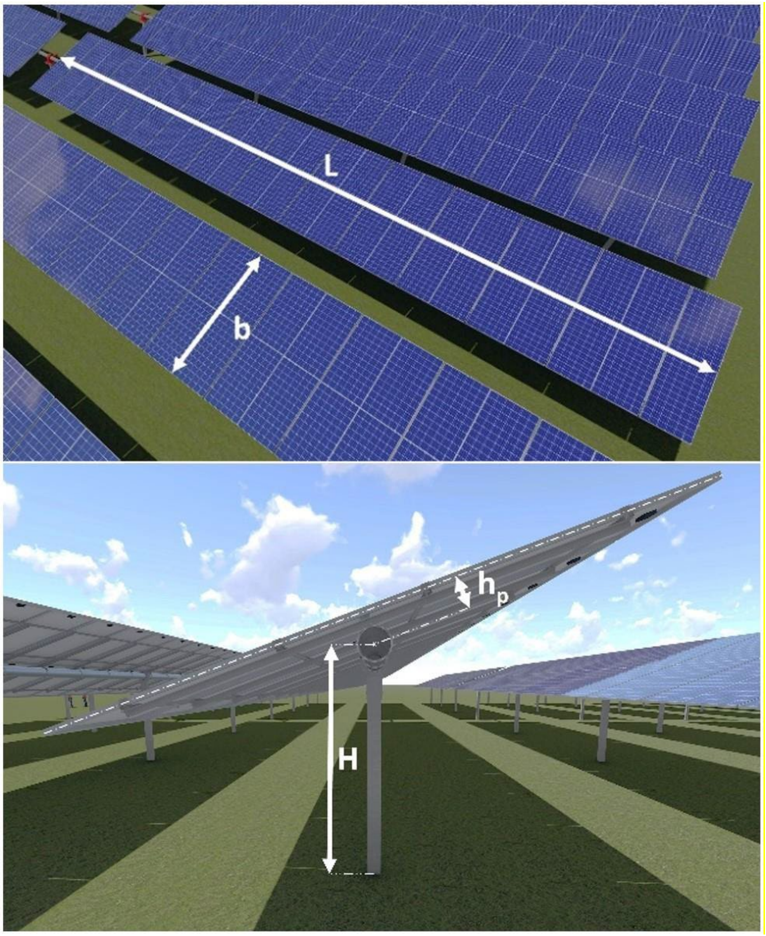

Figura 6. Estructura básica de seguidor solar monoeje. Dimensiones básicas de diseño, b (longitud de cuerda), L (longitud de brazo o eje), H (altura del eje respecto al suelo) y h_p (distancia del eje a la superficie solar).

La necesidad de reducir costes en un sector industrial tan competitivo ha llevado a diseños de eje de torsión más de menor diámetro. Estos últimos, combinados con grandes placas planas que pueden estar expuestas a la carga del viento, suelen dar lugar a seguidores solares que presentan inestabilidad aerodinámica (Martínez-García et al., 2021b). Esto implica que los criterios habituales de diseño estático no son válidos cuando la estructura comienza a presentar oscilaciones, ni siquiera si se considera un factor de amplificación dinámica (DAF) (R, C. et al, 2015; J, J. et al,2011). Además, las normas internacionales aún no incluyen específicamente este tipo de estructuras ni los fenómenos aeroelásticos que pueden afectarlas.

Capítulo 1. Caracterización del estudio de los seguidores solares monoeje

1.1 Particularidades estructurales de los seguidores solares monoeje.

Un seguidor solar monoeje es una estructura compleja formada por varios paneles fotovoltaicos de dimensión y disposición variable, sobre un eje horizontal, normalmente tubo circular o cuadrangular trabajando a torsión, accionado por un motor central. La estructura es simétrica respecto a la moto-reductora, que hace girar el eje del seguidor provocando que la orientación de los paneles varíe respecto al azimut solar. De esta forma, la superficie solar (placas) hacen un seguimiento este-oeste de la radiación solar incidente. Este método maximiza la cantidad de horas diarias de radiación solar directa que reciben los paneles solares, y optimiza el ángulo de incidencia de esos rayos solares sobre la superficie del captador, haciendo el proceso de captación más eficiente. El eje está soportado a una distancia fija del suelo, por varios pilares intermedios que impiden el movimiento horizontal y vertical, pero permiten la rotación libre. Desde el punto de vista estructural, los seguidores solares monoeje poseen un grado de libertad 1DOF (por sus siglas en inglés, one degree of freedom), y corresponde a la rotación torsional.

Esta estructura se comporta como una viga empotrada a torsión, cuya constante de torsión viene definida por el eje; los ejes, normalmente son de sección circular, rectangular o hexagonal con diámetros relativamente grandes y espesores pequeños para aumentar la rigidez. La inercia, sin embargo, viene definida por los propios paneles más el armazón que los une, vigas y puntales (G, L. et al, 2020). La altura del tubo sobre el suelo es aproximadamente la mitad de la anchura total del panel del seguidor.

En estos sistemas estructurales, el primer modo de vibración suele ser una torsión helicoidal de baja frecuencia (en torno a 1 Hz), que no genera deflexión alguna en el eje motor, pero sí provoca una rotación opuesta en ambos extremos del mismo (R, C. et al., 2015).

La búsqueda de máxima eficiencia y competitividad deriva en la necesidad de abaratamiento de costes para la producción industrial de estas estructuras, y ello supone que los diseños de los seguidores reduzcan sus espesores de tubo y amplíen la superficie de captación (placas solares), dando lugar a estructuras más esbeltas y menos robustas. El resultado es que estructuras de hasta 2m de altura con grandes superficies solares (hasta 4 y 6 m) dispuestas sobre un solo eje, quedan frágilmente expuestas a los efectos del viento. Estos efectos son la aparición de fenómenos aeroelásticos (interacción fluido-estructura) provocando inestabilidades oscilatorias en la estructura que la hacen colapsar (M-G, E et al., 2021b). En particular, este tipo de estructuras pueden estar sujetas a diferentes tipos de fenómenos aeroelásticos, incluyendo galope torsional o flameo de un grado de libertad, vibraciones inducidas por vórtices y bataneo.

1.2 Fundamentos teóricos de los fenómenos aeroelásticos

Para poder explicar los fenómenos que se producen por los efectos del viento sobre una estructura, es preciso retroceder al origen de la disciplina científica de la aeroelasticidad que fue descrita por primera vez en 1947 por Arthur R. Collar (véase Figura 7). La aeroelasticidad es una rama de la aerodinámica que estudia la interacción entre las fuerzas aerodinámicas, las fuerzas elásticas y las fuerzas de inercia. Analiza las respuestas estáticas y dinámicas de una estructura elástica frente a las fuerzas aerodinámicas (P. W, H, 1985). Fue descrita por primera vez en 1947 por Arthur R. Collar (véase Figura 7).

Figura 7. Diagrama de Collar de la aeroelasticidad.

El caso de estudio objeto de esta tesis abarca varios fenómenos aeroelásticos como: flameo, galope torsional y vibraciones inducidas por desprendimiento de vórtices. Las funciones de flameo se utilizan para definir las fuerzas aeroelásticas que actúan sobre un perfil con un movimiento armónico. Las inventaron Scanlan y Tomko en 1971, como una generalización de la teoría de Theodorsen que resuleve el problema de un ala inmersa en un flujo bidimensional oscilando armónicamente alrededor de un eje que pasa por su centro (León Alonso,A. et al., 2007).

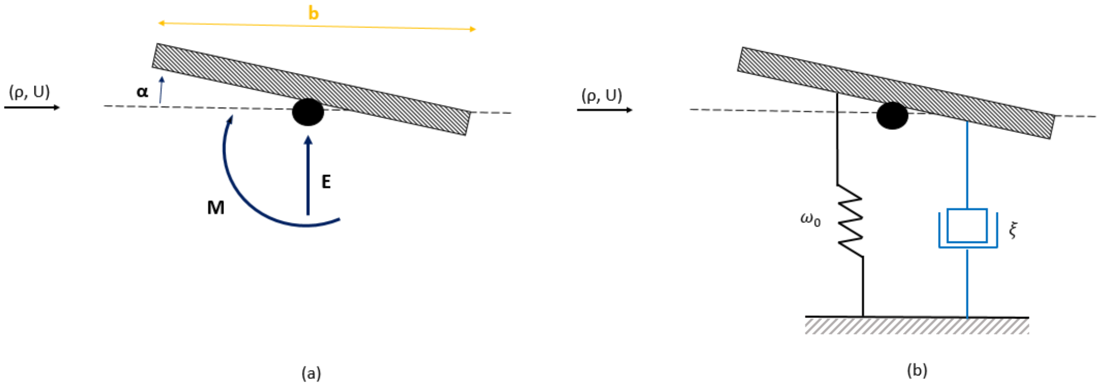

Figura 8. Esquema del modelo de flameo de una placa plana: Actuación de las fuerzas de empuje y momento torsor sobre placa y eje (a). Esquema mecánico muelle-amortiguador (b).

Al manifestarse estos fenómenos las principales fuerzas que intervienen son: E, sustentación; M, momento torsor, y V, la velocidad del viento (o frecuencial de desprendimiento de vórtices). Estas fuerzas dan origen a oscilaciones que causan desplazamientos verticales y desplazamientos angulares rotacionales, α. En la Figura 8, se muestra el esquema de fuerzas que aparecen en una placa plana sometida a la acción del viento, momento torsor sobre su eje y empuje sobre la placa. Así mismo, en el segundo esquema se representa mecanismo muelle-amortiguador, que explica la reacción de la estructura al fenómeno de desprendimiento de vórtices derivado de la interacción entre el viento y la estructura.

Los primeros estudios de esta tipología se implementaron en el ámbito aeroespacial, poniendo especial énfasis en los fenómenos aeroelásticos que aparecían en alas de avión y toberas. A medida que la rama de conocimiento avanzaba, comenzó a aplicarse a estructuras civiles que mostraron sensibilidad a los efectos del viento, como puentes (el caso del puente de Tacoma en 1940) o cables eléctricos. La mayoría de estudios realizados en el área de aerodinámica civil, se han centrado en la predicción de los mecanismos de oscilaciones autoexcitadas (flameo y divergencia torsional) y el movimiento de bataneo (T.N, J.M., 2008). Los estudios iniciales y de significativa importancia son los ensayos dimensionados en base al número de Strouhal. En estos se varían las dimensiones de la geometría expuestas a la normal del flujo incidente (ángulo inclinación placa plana), y la velocidad del flujo (Reynolds). Como conclusión, se aprecia un comportamiento repetitivo en todos los estudios, los ángulos de inclinación entre 10°-90°, implican una sección de la superficie de la placa que facilita un flujo completamente separado de la superficie, permaneciendo el valor de St dentro de un rango estable. En cambio, para ángulos menores, entre 0°-5°, la influencia del valor de Re es significativa ya que favorece el readherencia del flujo a la placa provocando inestabilidades (C, J. et.al, 1996). En el caso de cilindros sometidos a las mismas condiciones de St y Re, aparece el mismo comportamiento que con placa plana (K, C.W, 1989). Un flujo que se re-adhiere para ángulos de incidencia del flujo menores de 10°. Así mismo, se observa como la intensidad de turbulencia mayor del 10% no afecta la frecuencia de desprendimiento de vórtices, situación que se apreciará en los resultados de los ensayos del presente trabajo. Los fenómenos aeroelásticos que aparecen en las estructuras solares actuales, cada vez más esbeltas y flexibles suelen ser de naturaleza dinámica no estacionaria:

- Vibraciones inducidas por vórtices (VIV)
- Flameo clásico y flameo de un grado de libertad

El fenómeno de VIV aparece cuando la frecuencial de desprendimiento de vórtices en el frente de la placa solar, es igual a la frecuencial natural de la estructura. Da lugar a la aparición de vibraciones en esta última que al aumentar o disminuir la velocidad del viento desaparecen.

El flameo de un grado de libertad aparece en estructuras alargadas y rectas que guardan cierta similitud con los perfiles alares aeronáuticos. La aparición del fenómeno en seguidores solares monoeje se caracteriza por el desplazamiento a torsión.

1.3 Estudio de los fenómenos aeroelásticos en estructuras solares

Este tipo de fenómenos aeroelásticos se han estudiado durante décadas en distintos tipos de estructuras flexibles (Scanlan y Sabzevarit, 1969) pero, en el caso de los seguidores solares de un eje (SAT), su potencial de daño sólo se ha comunicado recientemente (Valentín et al., 2022). Se desconocen las causas y efectos de estos fenómenos, y es preciso realizar el estudio de cómo pueden interactuar (Enshaei et al., 2023). Comprender los fenómenos implicados es crucial para mejorar el rendimiento aeroelástico de los SAT mediante diseños más eficientes (Gross et al., 2020), así como para evitar posibles fallos derivados del uso de normativa no específica en la fase de planificación (Cheruku et al., 2020). Es por ello que, en la actualidad se están desarrollando diversos proyectos relacionados con el estudio de esta fenomenología en todo el mundo (Bruner et al., 2022).

Durante las últimas décadas, la captación de energía solar se ha basado en distintas tipologías estructurales con diversas geometrías: heliostatos, seguidores solares, colectores, paneles suspendidos por cables, estructuras fijas, etc. Fue Roschlke, en 1984, el primero en resaltar la relevancia de estudiar adecuadamente las cargas de viento en sobre la estructura de concentradores solares, y la aparición de fenómenos aeroelásticos. En el caso de los helióstatos, las investigaciones recientes se han centrado en los picos de carga de viento y en el uso de elementos pasivos, como vallas y alerones, para mitigar dicha carga (Pfahl, 2018; Pfahl et al., 2011). Los módulos fotovoltaicos soportados por cables en suspensión, pueden ser especialmente propensos a vibrar bajo cargas de viento. Las condiciones de estabilidad en estos fueron estudiadas por He et al. (2020). Además, Chen et al. (2023) presenta una revisión exhaustiva centrada en la respuesta inducida por el viento de los sistemas fotovoltaicos flexibles. Sin embargo, los resultados y conclusiones extraídos de estos estudios no pueden aplicarse directamente a los SAT debido a la peculiaridad de su geometría y diseño estructural, por lo que es necesario llevar a cabo investigaciones específicas sobre esta tipología estructural.

1.4 Metodologías y modelos utilizados para el estudio de los fenómenos aeroelásticos en estructuras solares.

1.4.1 Cargas estáticas

En los últimos 10 años, se han desarrollado varias técnicas para estudiar estas estructuras flexibles, tanto en configuraciones de una fila como de varias filas. El procedimiento más sencillo en la industria es la ejecución de ensayos estáticos en túnel de viento, que ayudan a diseñar las estructuras SAT en base a las cargas estáticas del viento sobre la misma, pero este método está obsoleto y es inexacto, ya que no evalúa la carga aeroelástica y la respuesta dinámica de la estructura. En lugar de los datos del túnel de viento, McBean (1985) utilizó una distribución simplificada de la presión del viento para obtener un diseño conservador de las estructuras, excepto en el caso de los colectores sometidos a graves efectos de turbulencia cerca del borde del campo solar. Así mismo, anotó que el comportamiento aeroelástico debería evaluarse en túneles de viento para valorar la posibilidad de vibraciones inaceptables debidas al desprendimiento de vórtices o el aleteo. Más recientemente, Strobel et al. (Strobel y Banks, 2014) demostraron que la norma convencional de "umbral de 1 Hz" no es adecuada para los conjuntos de paneles fotovoltaicos montados en el suelo en configuración de varias hileras, ya que estas pequeñas estructuras pueden presentar tanto autoexcitación como golpeteo de los paneles contra el viento a frecuencias muy superiores a ese valor tanto durante los eventos de viento de servicio como de diseño.

1.4.2 Consideraciones dinámicas

Posteriormente, Cain et al. (2015) demostraron que los códigos habituales no consideraban adecuadamente la excitación por amortiguamiento y desprendimiento de vórtices, por lo que intentaron determinar las velocidades del viento límite para un funcionamiento seguro combinando varias variables dinámicas tanto del viento como de la estructura, entre ellas el factor de ráfaga, el factor de amplificación dinámica (DAF), la velocidad reducida y la amortiguación estructural. Desde entonces, varios estudios sobre modelos rígidos a escala han considerado ensayos de configuraciones de varias filas en túneles de viento de capa límite atmosférica (ABL), con el fin de incluir la excitación del viento fluctuante. En general, los resultados muestran que las fuerzas y el par aerodinámico dependen de la separación entre filas y son mayores en la región perimetral, por lo que es necesario considerar el efecto del apantallamiento. Sin embargo, en lugar de abordar los fenómenos aeroelásticos reales, estos estudios seguían basándose principalmente en el concepto DAF (Kray y Markus, 2019) y en las relaciones de recubrimiento, la relación de aspecto del panel y los coeficientes de fuerza y par para estructuras estáticas (Y, et al., 2018). Con este mismo tipo de supuestos, Wittwer et al. (2022) combinaron estudios experimentales sobre modelos rígidos con simulaciones FEM para determinar los peores escenarios tanto para configuraciones de una fila como de varias filas, señalando que las normas no pueden aplicarse a todas las situaciones individuales. Estudios más recientes se han centrado en los puntales de la estructura subyacente, de los que se ha determinado que desempeñan un papel en la respuesta dinámica, especialmente cuando los ángulos de inclinación son pequeños (C, , 2022), o en los efectos de interferencia entre filas SAT (M, 2023).

También se han realizado ensayos dinámicos para caracterizar el comportamiento aeroelástico de los SAT y las condiciones que conducen a la inestabilidad fluido-estructura. En este tipo de ensayos, la extrapolación de los resultados está sujeta a la verificación de las condiciones de semejanza habituales para el flujo viscoso no estacionario, como los números de Strouhal y de Reynolds, pero también para los parámetros dinámicos de la estructura, como la frecuencia y los coeficientes de amortiguación, como se recogen la American Society of Civil Engineers - ASCE, 2021 y Hao (2020). Un objetivo básico de estos estudios es determinar el umbral o la velocidad crítica del viento para el inicio de la inestabilidad, que equivale a la velocidad crítica para el flameo de un sistema 1DOF (también denominado galope en la bibliografía de referencia).

1.4.3 Modelos seccionales en túnel de viento. Derivadas de flameo

Un procedimiento habitual es implementar ensayos dinámicos seccionales (2D) en túnel de viento para estudiar la variación del ángulo de ataque del seguidor cuando se somete a flujo cruzado (Franchini et al., 2019). Inicialmente, estos estudios se basaban en ensayos clásicos sobre formas bidimensionales de sección rectangular rectangulares sometidos a vibraciones inducidas por vórtices (VIV) o galopes (Mannini et al., 2014), considerando así el número de Strouhal (St) y el número de Scruton (Sc) como otros parámetros adimensionales para modelizar los fenómenos. Pigolotti et al (2017), la influencia de estos parámetros en la velocidad crítica para la inestabilidad y también en la respuesta en el régimen pos-crítico, determinando la relación de amortiguamiento neto del sistema acoplado flujo-estructura. Quintela et al (2020), realizaron ensayos experimentales seccionales en túnel de viento e integración numérica asistida por ordenador para estimar las denominadas derivadas de flameo, que están relacionadas con los coeficientes de fuerza y par no estacionarios, para explicar el desarrollo del desprendimiento de vórtices, la divergencia torsional y el flameo de los SAT. También exploraron el uso de amortiguadores mecánicos para controlar el desarrollo de la inestabilidad flutter (Quintela, J. et al., 2020). Más recientemente, (Frontini et al., 2022; Martínez-García et al., 2021b) presentaron diagramas de estabilidad para galopante o flutter de 1 DOF, que muestran la dependencia de la velocidad crítica con el ángulo de inclinación de los paneles. La influencia de la intensidad de la turbulencia también se ha analizado en un modelo seccional (Ma et al., 2023) mostrando dos comportamientos diferentes para grandes vibraciones torsionales en varios ángulos de inclinación: acoplamiento fuerte y débil. El mismo modelo se utilizó para el estudio de la configuración de varias filas (Zhang et al., 2023) y se observó que la interferencia entre las filas es débil cuando los seguidores están casi horizontales, y se desarrolla una inestabilidad de aleteo para cada fila; sin embargo, para inclinaciones mayores la interferencia aumenta, y la vibración se acerca más al tipo de vibración inducida por vórtice. Las condiciones de estabilidad para la inestabilidad torsional en función de la altura del SAT sobre el suelo han sido expuestas recientemente por (Cárdenas-Rondón et al., 2023).

1.4.4 Modelos aeroelásticos 3D

Sin embargo, el primer diagrama de estabilidad para un amplio rango de dimensiones de seguidores fue publicado por Martínez-García et al. (Martínez-García et al., 2021b), utilizando otro enfoque, que consiste en considerar un modelo 3D completo de un seguidor bajo condiciones estrictas de similitud aeroelástica (Martínez-García et al., 2021a). Esto también puede extenderse a configuraciones multi-fila para estudiar el comportamiento de las filas internas y las posibles interacciones entre ellas, así como para analizar el efecto de la dirección del viento. Enshaei (2023) publicó un estudio sobre los métodos utilizados para estudiar la inestabilidad torsional y los resultados sobre los mecanismos de excitación.

Dada la complejidad de realizar mediciones precisas en modelos completamente aeroelásticos, Taylor et al (2020) propusieron un enfoque híbrido basado en ensayos en túnel de viento de modelos rígidos seccionales, para medir las distribuciones de presión, combinado con datos de fase relativos al movimiento del seguidor obtenidos a partir de cálculos numéricos (FEM y CFD). Con este procedimiento, es posible obtener los coeficientes aerodinámicos y las derivadas aeroelásticas del seguidor, de modo que se pueda reproducir el comportamiento aeroelástico completo y tenerlo en cuenta para el diseño estructural de los seguidores.

1.4.5 Modelos numéricos

El cálculo numérico mediante programas de simulación de dinámica de fluidos computacional (CFD) se han utilizado en paralelo con la investigación experimental, y a menudo de forma complementaria como en algunas de las referencias mencionadas.

De hecho, a pesar de los enormes avances de las últimas décadas tanto en capacidad computacional como en herramientas de análisis numérico, la validación experimental de las predicciones sigue siendo incuestionablemente necesaria. Para describir los flujos de interés en problemas aeroelásticos, como los flujos altamente inestables que involucran estelas 3D y estructuras vorticales que fluctúan junto con el movimiento del seguidor, se pueden utilizar modelos de flujo no estacionario que van desde el básico URANS hasta las formulaciones LES más completas (Breuer y Jovicic, 2001). Sin embargo, los costes computacionales asociados a los modelos 3D siguen siendo elevados, por lo que frecuentemente se han considerado modelos 2D de placas planas (Barrero-Gil y Sanz-Andrés, 2009) para simular inestabilidades aeroelásticas tanto lineales como no lineales. Young et al (2020) analizaron la posición de estiba de un SAT y descubrieron que la inestabilidad de galope está relacionada con el desprendimiento cíclico de vórtices en el borde de sotavento y las propiedades elásticas del tubo de torsión. También se han realizado simulaciones numéricas con amortiguadores hidráulicos (Watwe y Kartik, 2021).

1.4.6 Modelos combinados

Un enfoque diferente, ha sido el de algunos estudios que han utilizado datos de mediciones de plantas a escala real con condiciones reales de viento, contrastando así las predicciones de modelos teóricos o numéricos, e incluso comprobando la extrapolación de datos de túneles de viento, ya que estos últimos se obtuvieron en un entorno controlado de laboratorio. Es el caso de Dana (2020), que realizó mediciones de carga y aceleración en prototipos SAT ubicados en una planta fotovoltaica real, con el objetivo de contrastar las características de estabilidad predichas a partir de simulaciones 3D y obtener un mapa de estabilidad. Tras ensayar paneles con diferentes ángulos de inclinación y diversas condiciones de viento, concluyeron que los paneles son más estables cuando se orientan con un ángulo negativo (es decir, con el borde de ataque más cerca del suelo), debido a los efectos de bloqueo del suelo. Además, se utilizaron sensores de fibra óptica para medir la distribución de la tensión y la temperatura a lo largo de una estructura SAT (Mariñelarena et al., 2019), y para monitorizar la torsión estructural en condiciones de campo (Leandro et al., 2020).

También se han realizado ensayos en instalaciones reales con otros tipos de captadores solares que, al igual que los SAT, también involucran paneles fotovoltaicos bajo carga de viento. Bhaduri y Murphy (1985) publicaron un extenso informe sobre los perfiles de velocidad del viento sobre los paneles fotovoltaicos y los coeficientes de fuerza resultantes sobre los paneles en función de la relación de aspecto y el ángulo de inclinación, incluyendo una comparación con el enfoque estático del código ASCE y aspectos de validación con experimentos a gran escala. También estudiaron los espectros de las fluctuaciones de la velocidad turbulenta, remarcando la importancia de los aspectos topográficos. Más recientemente, Adelake (2016) combinó mediciones de galgas extensiométricas in situ con un modelo FEM de un seguidor solar de dos ejes, para predecir desplazamientos a velocidades de viento más altas. Kaabia et al. (2017) realizaron pruebas a escala real en paneles fotovoltaicos de concentración (CPV) en condiciones de velocidad de viento moderada (en consecuencia, las fuerzas obtenidas no pueden extrapolarse a eventos de viento extremo).

1.4.7 Otros estudios relacionados

Es recomendable llevar a cabo investigaciones teóricas u otro tipo de ensayos que analicen el mismo fenómeno de forma diferente; así como explorar otros fenómenos y sus posibles interacciones. Entre los primeros, se desarrolla la influencia de las propiedades mecánicas de un panel de señalización en las fuerzas inducidas por el viento (Barrero-Gil y Sanz-Andrés, 2009). Y respecto a las segundas, Armandei (2 014) observó que una placa plana rectangular con 1DOF (torsional) se vuelve inestable cuando la velocidad de la corriente supera un valor crítico; se realizaron experimentos en un canal de agua a Re = 1-105, se extrajo el momento en la placa a partir de las derivadas del flameo (experimentos de vibración libre) y se analizó la bifurcación de Hopf. Existen varios estudios del fenómeno del fluido oscilante a través del número de Strohual, aunque la mayoría de ellos se realizan en cuerpos estáticos. Por ejemplo, son bien conocidas las explicaciones de la separación y reacoplamiento de la capa límite en formas bidimensionales de sección cilíndrica (Knisely, 1990) y placas planas (Chen y Fang, 1996), en función del ángulo de ataque. Rostami et al (2019) realizaron una prueba en un canal de agua y ofrecieron una interesante contribución sobre cómo la fuerza del vórtice podría desencadenar el galope en una placa plana y aleteada. Marra (2015), mencionó el interés de estudiar la vibración inducida por vórtices en cilindros rectangulares y la necesidad de verificación para otras estructuras en las que la amortiguación es incierta, o es necesario diseñar amortiguadores. Se ha identificado la interacción entre algunos fenómenos aeroelásticos: la investigación sobre cilindros esbeltos montados sobre muelles concluyó que las estructuras con propiedades de amortiguación de masa ordinaria pueden mostrar vibraciones sostenidas en rangos de velocidad de flujo en los que no se predice ninguna excitación mediante las teorías clásicas de vibración inducida por vórtices y galope (Mannini et al., 2016).

1.5 Breve introducción al compendio de los artículos incluidos en esta tesis.

Esta tesis doctoral está constituida por la compilación de tres artículos científicos derivados de la necesidad de atender los fenómenos de inestabilidad aeroelástica que sufren los campos de seguidores solares monoeje. La Tecnología solar de seguimiento de un solo eje, es la tecnología predominante en instalaciones solares a gran escala debido a su eficiencia y relativa rentabilidad.

Estos seguidores, diseñados para seguir el sol a lo largo del día y así maximizar la captación de energía solar, son estructuras que, debido a sus grandes dimensiones y reducida rigidez, son susceptibles a fenómenos de inestabilidad como el galope torsional. Este tipo de inestabilidad es especialmente problemático dado que, bajo ciertas velocidades de viento y configuraciones estructurales, puede desencadenar oscilaciones críticas que lleven al fallo estructural, como describen los artículos de Martínez-García (2021a y 2021b).

En el tercer artículo (Martínez-García et al, 2024) se proporciona un modelo de referencia para ensayos en túneles de viento, que permite reproducir y comparar resultados de manera estandarizada. Esta iniciativa responde a la falta de criterios confiables y estándares en ingeniería para asegurar condiciones seguras de operación y diseño.

Los estudios emplean metodologías tanto analíticas como experimentales para abordar la cuestión de la inestabilidad torsional en los seguidores solares. En el primer artículo (Martínez-García et al, 2021a), se desarrolla un modelo aeroelástico simplificado de un seguidor solar, y mediante el análisis adimensional de las variables que intervienen en el fenómeno físico y con la ayuda de ensayos experimentales en túnel de viento, se demuestra la aparición del fenómeno aeroelástico de galope torsional. Este galope y la vibración inducida por vórtices, son dos fenómenos que aparecen durante los ensayos en función del ángulo de inclinación del seguidor.

A partir de estos primeros hallazgos, en el segundo artículo se propone un avance en el estudio analizando las propiedades estructurales que favorecen la aparición de las inestabilidades aeroelásticas. La metodología experimental es la misma que en el caso anterior, pero esta vez los modelos utilizados varían su relación geométrica de aspect y la rigidez torsional del eje del seguidor. El estudio revela que la velocidad crítica para el galope torsional depende del ángulo de inclinación y, en menor medida, de parámetros estructurales como la rigidez torsional y la inercia de los modelos. Los resultados dan lugar a un diagrama de estabilidad que proporciona una guía de dimensionamiento óptimo para evitar inestabilidades estructurales en seguidores solares monoeje (Martínez-García et al, 2021b).

El tercer artículo establece un modelo de referencia para la experimentación, lo que permite una caracterización detallada de los efectos aeroelásticos bajo condiciones controladas en túnel de viento. El modelo tiene en cuenta la rigidez torsional y flexional de los seguidores, y el procedimiento experimental es validado en dos instalaciones experimentales diferentes (Universidad de Oviedo y Universidad Politécnica de Madrid), demostrando que el método planteado y el modelo genérico poseen la capacidad de reproducir las condiciones de inestabilidad torsional que aparecen en campo, mediante un prototipo físico a escala en el laboratorio (Rodríguez-Casado et al, 2024).

Los tres estudios son complementarios para abordar los fenómenos que provocan las inestabilidades aeroelásticas y recogen las recomendaciones para un diseño estructural eficiente y seguro en seguidores solares monoeje. Mientras que el primero y segundo artículo se enfocan en modelar y entender el fenómeno de inestabilidad torsional mediante una combinación de teoría y experimentación en túnel de viento, el tercero amplía este conocimiento al proponer un modelo experimental de referencia para futuras investigaciones. Los hallazgos sobre la velocidad crítica y los factores que influyen en la inestabilidad torsional son comunes en todos. Los tres estudios, ofrecen una solución a uno de los problemas más graves que afectan la industria del seguimiento solar. Además, proporcionan una metodología de análisis y cálculo que no está considerada en los códigos y estándares de diseño.

Capítulo 2: Determinación experimental de la resistencia al galope torsional de un seguidor solar monoeje

2.1. Descripción del artículo

En este trabajo se analiza el fenómeno de inestabilidad aeroelástica, específicamente el galope torsional, en seguidores solares de un solo eje. Mediante un enfoque experimental y analítico, se identifican las velocidades críticas a las que se desencadenan oscilaciones peligrosas, particularmente en ángulos de inclinación entre -45° y -15° y de 20° a 40°. El estudio propone un diseño más robusto para aumentar la rigidez del eje de torsión y evitar el colapso estructural en condiciones de viento moderado, sugiriendo que un aumento en el grosor del eje podría soportar vientos de hasta 100 km/h. Se puede decir que el galope torsional es el principal factor de inestabilidad en seguidores solares de un solo eje. Los resultados, basados en modelos a escala y pruebas en túnel de viento, ofrecen una metodología para predecir y mitigar el riesgo de inestabilidad en estructuras de seguidores solares, aunque se recomienda más investigación en condiciones de viento turbulento y en plantas de filas múltiples. Además, se destaca que el fenómeno se puede mitigar mediante ajustes en el diseño estructural como el aumento de la rigidez del eje.

2.2. Publicación en revista revisada por pares

Determinación experimental de la resistencia al galope torsional de un seguidor solar monoeje

Structural Engineering and Mechanics, *Vol. 78, No. 5 (2021) 519-528*
DOI: https://doi.org/10.12989/sem.2021.78.5.519

Experimental determination of the resistance of a single-axis solar tracker to torsional galloping

Eva Martínez-García, Eduardo Blanco Marigorta, Jorge Parrondo Gayo and Antonio Navarro-Manso*

Department of Energy, University of Oviedo, Engineering Polytechnic School of Gijón,
C/ Wifredo Ricart, s/n, Edificio Departamental Este, Campus Universitario de Viesques, 33204 Gijón, Asturias, Spain

(*Received August 18, 2020, Revised November 15, 2020, Accepted March 13, 2021*)

Abstract. One of the most efficient designs of solar trackers for photovoltaic panels is the single-axis tracker, which holds the panels along a torque tube that is driven by a motor at the central section. These trackers have evolved to become extremely slender structures due to mechanical optimization against static load and the need of cost reduction in a very competitive market. Owing to the corresponding decrease in mechanical resistance, some of these trackers have suffered aeroelastic instability even at moderate wind speeds, leading to catastrophic failures. In the present work, an analytical and experimental approach has been developed to study that phenomenon. The analytical study has led to identify the dimensionless parameters that govern the motion of the panel-tracker structure. Also, systematic wind tunnel experiments have been carried out on a 3D aeroelastic scale model. The tests have been successful in reproducing the aeroelastic phenomena arising in real-scale cases and have allowed the identification and a close characterization of the phenomenon. The main results have been the determination of the critical velocity for torsional galloping as a function of tilt angle and a calculation methodology for the optimal sizing of solar tracker shafts.

Keywords: single-axis tracker; wind load; aeroelastic model; torsional galloping; stability diagram; wind tunnel

1. Introduction

Nowadays a wide-spread trend in the sector of solar photovoltaic farms is the use of single-axis solar trackers with one degree of freedom (Lave and Kleissl 2011). According to the common design of these trackers, the solar panels are held along a horizontal torque tube that can rotate up to a finite angle about a vertical axis by means of a motor located at the central section. Hence, this system allows to control the azimuth but not the altitude. Although the energy obtained is lower than with a two-degree-of-freedom (2DOF) solar tracker, it is still 30% higher than the one obtained with fixed solar panels (Talavera *et al.* 2019).

The structural arrangement of these solar trackers consists in several solar panels aligned on a torsional shaft. The torque tube is supported by several pillars that allow only for rotational motion. One end of the shaft is free, and the other one is fixed to a gearmotor (driver) that controls the angular position. Usually, these structures are symmetrical about the driver, with a row of panels at each side. Fig. 1 shows an example of structural scheme for this type of solar tracker.

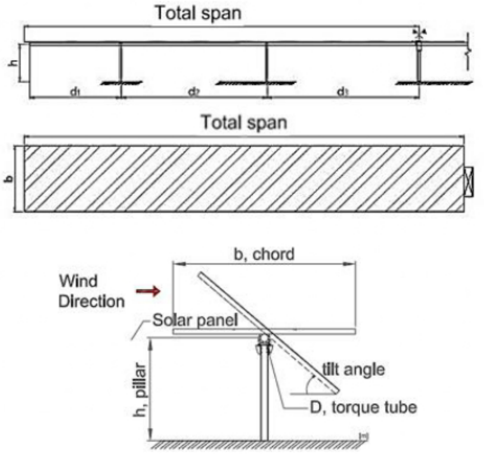

Fig. 1 Scheme of the single-axis solar tracker

Due to the progressive mechanical optimization against static loads and non-extreme accidental events, plus the continuous search for cost reduction in a very competitive market as the photovoltaic sector, those structures have evolved to become very slender. In the last years, however, that has led to multiple cases of aeroelastic instability phenomena under different conditions (Taylor and Browne 2020), which are attributed to torsional galloping, flutter or torsional divergence.

Frequently, those aeroelastic phenomena provoke the failure of the structure. Components commonly subjected to fatigue and collapse are the positioning motor, the driver supports and the main shaft, though the solar panels become frequently destroyed as well (Fig. 2).

While current construction standards are intended to account for basic aeroelastic effects (Blevins 1990, Païdoussis *et al.* 2011) by means of dynamic amplification

---

*Corresponding author, Professor
E-mail: navarroantonio@uniovi.es

http://www.techno-press.com/journals/sem&subpage=7

ISSN: 1225-4568 (Print), 1598-6217 (Online)

Fig. 2 Collapse of a single-axis solar tracker facility (rendering)

factors (Dyrbye and Hansen 1997, Taylor and Browne 2020), it is clear that they are not capable to include the specific effects of wind on single-axis trackers with solar panels. Indeed, an appropriate calculation of these structures has to be based on a deeper understanding of the aeroelastic phenomena involved, which usually requires wind tunnel tests (Taylor and Browne 2020).

Many studies have been conducted on the aerodynamics of flat plates, including analytical (Yang 2010), computational (Jubayer and Hangan 2015) and experimental methodologies (Strobel and Banks 2014). The object of study has ranged from the case of panels with single-degree-of-freedom models to complete photovoltaic farms with panels on solar trackers. The latter have usually been designed with static models in order to study the effect of wind directionality and the resulting interferences between different rows of trackers. However, few investigations have been based on full aeroelastic tests (Roedel and Upfill-Brown 2018).

Following that line of work, this paper presents a new study intended to develop a method of analysis and calculation of the mechanical characteristics of solar panel trackers that allows avoiding structure failures due to aeroelastic phenomena. As the state of knowledge for that structure typology is still at an early phase (Rhor *et al.* 2015), this study began with an inspectional analysis of the differential equation for shaft torsional motion, so that appropriate non-dimensional parameters could be established for both aerodynamic and structural phenomena. Similarity conditions were then applied for the design of small-scale models of solar panel trackers with full aeroelastic characteristics. Then, wind tunnel tests were extensively conducted under a variety of conditions.

As expected, several aeroelastic phenomena were observed, including vibrations induced by vortex shedding, torsional galloping or flutter. The main results obtained can be summarized as:

- Physical explanation of the aeroelastic phenomena causing instability in the solar tracker structure.
- Determination of the critical velocities for different tilt angles (azimuthal orientation).
- Proposal of a safe design criterion for the analyzed case in terms of project wind velocities and structure rigidity.

2. Methodology

2.1 Non-dimensional analysis

Nine variables were initially considered to configure the flow-structure system that represents solar panel trackers with a given geometrical pattern. Three of them correspond to the fluid: velocity, density and viscosity (U, ρ, μ). Four are related to the structure: characteristic length (L) - typically span or chord -, torsional stiffness (K), moment of inertia with respect to the shaft axis (I), and structural damping (c). The last variables refer to the aerodynamic forces, which in this case can be reduced to a torque magnitude (T), and an excitation frequency (ω).

The variables corresponding to the fluid and the aerodynamic forces, lead to the typical dimensionless numbers of Torque coefficient (C_T), in this case as the moment coefficient, Strouhal (St), and Reynolds (Re), Eqs. (1)-(3)

$$C_T = \frac{T}{{}^1\!/_2\, \rho U^2 L^3} \tag{1}$$

$$S_t = \frac{\omega L}{U} \tag{2}$$

$$R_e = \frac{\rho U L}{\mu} \tag{3}$$

Non-dimensional numbers that collect the properties of the structure can be derived from the equation of torsional motion as given by Eq. (4), where θ is the angular displacement:

$$I\frac{d^2\theta}{dt^2} + c\frac{d\theta}{dt} + K\theta = T \tag{4}$$

Analysis of Eq. (4) brings about three dimensionless parameters, which can be formulated as a torsional stiffness coefficient (C_k), a reduced natural frequency (ω^*) and the damping ratio (ξ), i.e., the ratio between structural and critical damping (Eqs. (5)-(7)). The meaning of the reduced frequency (ω^*) is analogous to that of the Strouhal number, except the former is relative to the natural frequency of the structure without flow effects and the latter is relative to the characteristic frequency of the aerodynamic phenomena.

$$C_K = \frac{K}{{}^1\!/_2\, \rho U^2 L^3} \tag{5}$$

$$\omega^* = \frac{L}{U}\sqrt{{}^K\!/_I} \tag{6}$$

$$\xi = \frac{c}{2\sqrt{KI}} \tag{7}$$

A conventional inspectional analysis of the basic flow equations can be used to deduce dependence relationships among those dimensionless parameters. In particular the magnitude of the aerodynamic forces as well as the characteristic frequency of the fluid-dynamic excitation, which are represented by C_T and St, can be considered to be dependent on the other four parameters, Eqs. (8)-(9)

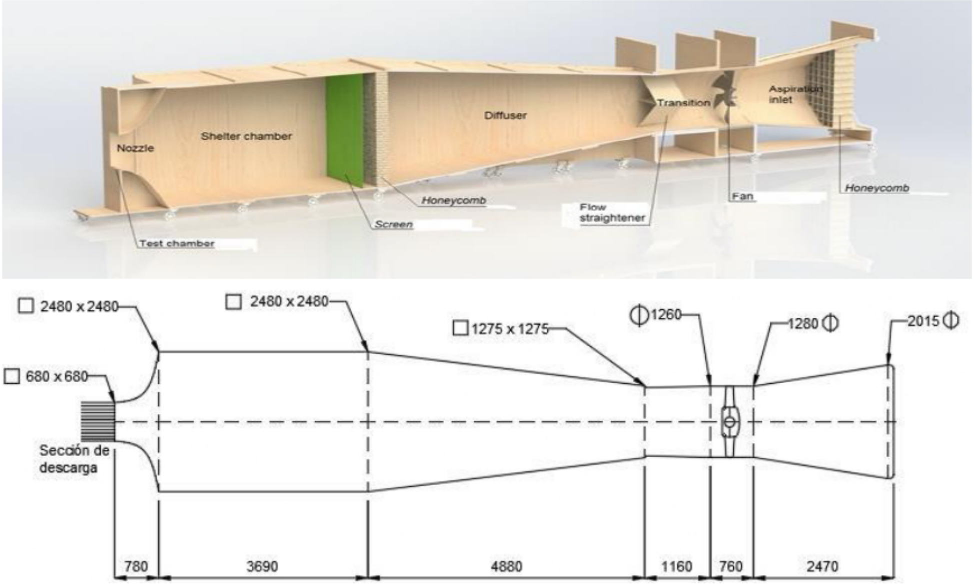

Fig. 3 Overview (up) and elevation (down) of the wind tunnel EB40-oWT

$$C_T = f(Re, C_K, \omega^*, \xi) \tag{8}$$

$$St = g(Re, C_K, \omega^*, \xi) \tag{9}$$

Therefore, if a prototype and a scaled model possessed the same values for those four dimensionless numbers, then the aerodynamic phenomena of interest would verify the conditions for similarity, and hence the parameters C_T and St of the scaled model would be equal to those of the prototype.

Regarding wind tunnel tests on reduced scale models, however, trying to impose exact similarity for the Reynolds number is usually incompatible with similarity for the other dimensionless parameters. Nonetheless, in this specific case the most important aerodynamic effects can be assumed to be related to dynamic bluff body separation and subsequent vortex shedding, rather than to boundary layer development and detachment. Because of that, the influence of the Reynolds number can be expected to be very small, especially when dealing with fully developed turbulent flows, and the Reynolds condition can be relaxed.

Hence, the design of the scale model should ensure that the other three dimensionless numbers, C_k, ω^* and ξ, are equal to those of the prototype. In the case of the damping ratio (ξ), that condition can be achieved by selecting materials with adequate mechanical properties, Eq. (10).

$$\xi_m = \xi_p \tag{10}$$

The moments of inertia of model and prototype are related through the length and density ratios. If their densities are equal, then the moment of inertia of the scale model must verify Eq. (11)

$$I_m = I_p \left(\frac{L_m}{L_p}\right)^5 \tag{11}$$

Identity of the torsional stiffness coefficient (C_k) between prototype and scale model brings about the following condition for the torsional stiffness of the model

$$K_m = K_p \left(\frac{U_m}{U_p}\right)^2 \left(\frac{L_m}{L_p}\right)^3 \tag{12}$$

Eq. (12) allows to determine the flow velocity to be imposed in wind tunnel on the scale model for given values of the torsional stiffness. And the latter can be conveniently modified by changing the shaft material or varying its diameter and thickness. In this way, there is a certain freedom between the scale and the torsional stiffness ratio in the model and prototype.

2.2 Wind tunnel and instrumentation

The experimental tests were developed in the aerodynamic wind tunnel denoted as EB40-oWT, which is located at the Energy Department building of the University of Oviedo. It is an open wind tunnel, the maximum air velocity at the test section is 35 m/s, the nominal power is 30 kW, 14.25 m in length and a test cross section of 0.68 x 0.68 m^2. Fig. 3 reproduces the elements of the wind tunnel. Other details as well as nozzle assembling can be seen in Rodríguez Lastra *et al.* (2013).

Figs. 4 (a)-(b) show the velocity profile (U/U_{max}) and turbulence intensity (TI) at the nozzle outlet of the wind tunnel. They correspond to the mid vertical plane and have been plotted as a function of the vertical coordinate y/z, with z=height of the nozzle outlet. Note that the same distribution is obtained in the mid horizontal plane due to the symmetry of the nozzle. It can be seen that the velocity profile is mostly uniform, since velocity values are higher than 98% of the maximum velocity except at the first 10 mm, which correspond to the thin boundary layer developed on the bottom surface. Besides, the turbulence intensity is

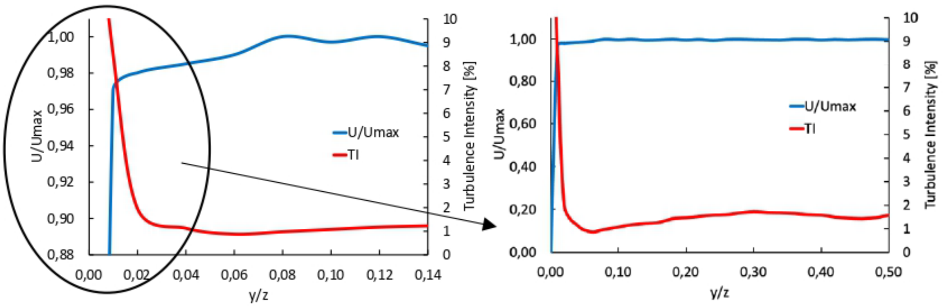

(a) Low half section (b) Detail on bottom wall (boundary layer effect)

Fig. 4 Profiles of velocity and turbulence intensity at the nozzle outlet (vertical direction)

Table 1 Prototype solar tracker dimensions

Description	Value
Tracker shaft length [m]	30
Shaft diameter [m]	0.2100
Shaft thickness [mm]	6
Shaft stiffness [N·m]	113450
Inertia [kg·m²]	1668
Panel chord [m]	3
Panel thickness [m]	0.0135

below 1,7% except for the first 15 mm above the side and bottom walls.

For the current tests, the scale models were placed close to that bottom wall to resemble the proximity of the floor in real situations, but nonetheless the tracker board was well within the zone of uniform speed and turbulence.

During the tests, two main variables were measured: the rotation amplitude at the free end of the tracker and the torque at the driver, which was located at the other end.

For the rotation measurements, digital photography and video were used, together with an image analysis software. Video recording speeds of 300 and 1000 frames per second were used for the unsteady measurements. The estimated accuracy of the angle measurement was 1 degree.

The torque at the driver was measured with a torsion balance that has an accuracy better than 1%, and a signal acquisition system whose frequency range is above 1 kHz.

2.3 Solar tracker scale models

The single-axis solar tracker prototype studied has the basic arrangement of this kind of structures, with the features indicated in the Table 1.

In this kind of solar trackers, damping ratios are low and correspond to the natural value of the materials, mostly of the shaft.

The torsion values of the structure are determined only by the shaft because the stiffness of the panel has little influence on this property of the structure (Katariya and Panda 2019, Aydogdu *et al.* 2018, Ebrahimi *et al.* 2020).

However, the inertia of the system comes determined by the surface and cross section of the panels because the shaft mass is small and concentrated on the axis.

The solar tracker is supported by four pillars and the height from the torsional axis respect to the floor is 20% bigger than half of the panel chord.

Fig. 5 Aeroelastic scale model

Table 2 Solar tracker model: main geometrical dimensions of panels and supports

Description	Value
Tracker shaft length [m]	0.670
Panel chord [m]	0.067
Support height [m]	0.040
Purlin thickness [m]	0.003

Table 3 Structural properties of models with different shafts

Concept	Brass	Steel
K [Nm]	0.092	0.200
I [kg·m²]	9.02e-6	9.02e-6
ξ [%]	1.600	2.400
ω_0 [Hz]	25.300	37.000

Fig. 5 shows an experimental model installed on the test section. Considering the symmetry of the solar tracker, the experimental model represents only half of the structure from the driver (fixed end) to the free end. In order to take full advantage of the test section, the scale is 1/45, meaning a blockage below 7 or 8% in any tilt position.

The models have been built mostly with PLA material, using additive manufacturing technologies. Table 2 contains the main information of the scaled structure.

Two types of models have been employed. Both have the same features except for the torsional stiffness of their shaft, in order to study its influence on the critical velocity. One is made of steel, resulting in a torsional stiffness K=0.2 N·m, the other is made of brass, giving a K=0.092 N·m. Table 3 collects the properties based on the type of shaft.

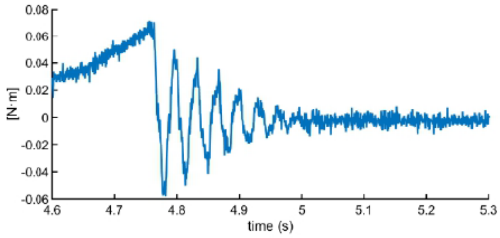

Fig. 6 Torque signal at the driver (fixed) section (impact test)

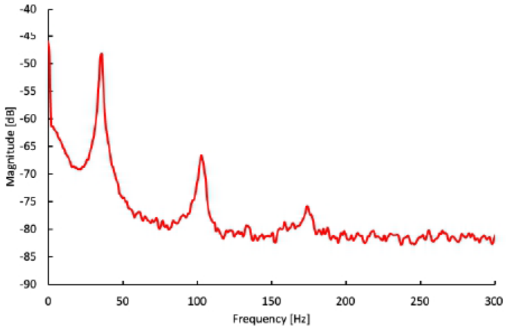

Fig. 7 Frequency spectrum of torque signal (impact test)

Impact tests were performed to obtain the natural frequencies and damping ratio of the models. As an example, Fig. 6 shows a typical time signal of the drive torque after an initial displacement under no airflow conditions, exhibiting an amplitude decay from which the damping coefficient can be obtained.

Fig. 7 presents the frequency spectrum of the torque signal from another impact test. The peak at 37 Hz, the one with highest amplitude, corresponds to the main natural frequency of the structure with the steel shaft. The logarithmic scale used for the torque axis allows to appreciate that there is also low amplitude excitation at higher frequencies, which are associated to harmonics of the first natural frequency and, to a lesser extent, to higher order vibration modes.

Since the inertia of the structure is uniformly distributed along the axis, the natural frequencies of the vibration correspond to the expression shown in Eq. (13) (Rao 2007, see Mohammadnejad 2015 for a more precise calculation)

$$\omega_n = \frac{(2n+1)\pi}{2}\sqrt{\frac{K}{I}} \qquad (13)$$

3. Experimental results

In this section, experimental tests are explained and discussed.

3.1 Description and classification of the phenomenon

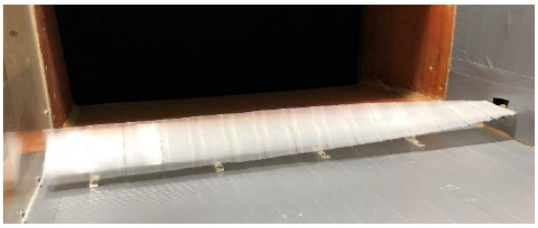

Fig. 8 Non-linear deformation of the structure during torsional galloping

Fig. 9 Oscillation of the free end of the panel during torsional galloping

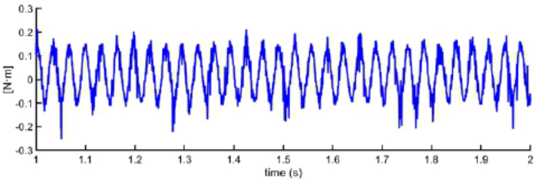

Fig. 10 Torque at the driver section of the scale model during the torsional galloping (tilt angle 20° and wind velocity 9.2 m/s)

According to different models tested, as the velocity increases, small vibrations can may occasionally be observed; maybe due to turbulence or to sporadic vortex separation. Anyway, these are normally random and small amplitude oscillations. Nevertheless, a much more intense vibration develops from a certain velocity upwards.

Figs. 8-9 show the oscillations of the models under the wind load. As will be discussed below, these oscillations are believed to correspond to the phenomenon of torsional galloping, or one degree of freedom (1DOF) torsional flutter.

As stated in the Section 2, it has been possible to measure the angles rotated by the free end of the tracker and the torque on the driver. For instance, Fig. 10 shows the time signal of the torque during a galloping event. It corresponds to the tracker at a tilt angle of 20° and a 9.2 m/s wind speed. In this case, the amplitude of the torque oscillation is about five times greater than the average value. The average value is roughly speaking the one supported by the tracker just before galloping.

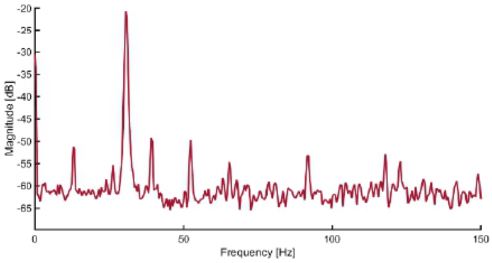

Fig. 11 Frequency analysis corresponding to the torque on the driver section of the scale model during the torsional galloping (tilt angle 20° and wind velocity 9.2 m/s)

Fig. 11 depicts the FFT of the time signal. The main frequency of the oscillation is somewhat less than the first natural frequency of torsion of the tracker structure (due to the added aerodynamic stiffness). Also, for this case, the free end average angle is about 27°, seven more degrees than on the driver. The amplitude is about 72°, from -9° to 63°.

This phenomenon seems to be caused by the aeroelastic interaction of vortex shedding at the leading and trailing edges of the panel, and the torsion of the structure. In simplified terms, vortex shedding causes the torque to fluctuate and the panel to rotate cyclically on its axis. At the same time, when the amplitude of the rotation is large enough, the oscillation of the panel causes the separation of the vortexes at the location of the extreme rotations. In this way, the frequency of vortex separation is "locked in" to the natural frequency of the structure, and the fluid dynamic and mechanical phenomena feedback on each other.

As an example, in order to better understand and visualize the mechanism of the vortices that take part in the instability, Fig. 12 represents a numerical simulation of this phenomenon. The numerical model has been solved with the finite volume FLUENT code. It corresponds to an unsteady 2D simulation, including the ground effect. Up to 100.000 triangle unstructured cells have been used, together with a 0.001 s time step. The turbulence has been included using an RNG model and the boundary conditions were the atmospheric pressure and uniform velocity inlet (20 m/s in Fig. 12).

Essentially, the oscillation occurs centered on the original tilt angle and the separation of the vortices occurs near the location of extreme rotations. In a strong galloping there is vortex shedding at both the leading and trailing edges, although the one at the leading edge is larger and seems to be the main factor in the phenomenon (Rhor *et al.* 2015). In addition, some factors complicate even more the interaction between the flow and the motion of the structure. Consider, for instance, that there is no symmetry between the top and bottom due to the tilt angle and the proximity to the ground.

With regard to the identification of the phenomenon, its characteristics make it difficult to classify. On the one hand, torsional divergence, buffeting and wake induced vibrations can easily be ruled out: torsional divergence because it is a static phenomenon, the buffeting and the wake induced vibrations, because of the characteristics of the wind tunnel and because, as studied, the tracker would correspond to the first row in the column. This does not mean that these phenomena cannot be factors that facilitate the instability in subsequent rows.

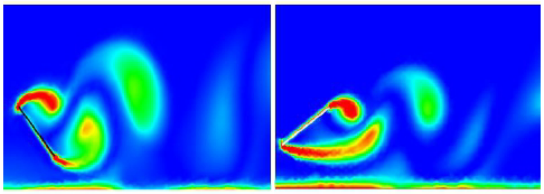

Fig. 12 Numerical simulation of the torsional galloping (contours of vorticity)

On the other hand, the phenomenon seems to share some of the characteristics of vortex induced vibrations, flutter and galloping, although with reservations. With respect to the first one, as it has been commented, there is vortex shedding, but it does not behave like a bluff body. It has also been proven that it can be triggered at any speed that exceeds a certain value, regardless of the number of Strouhal.

Although the galloping is typically related to a bending movement, due to the stiffness of the cross section and changes in the lifting and drag forces during the rotation, this instability could be classified as a type of torsional galloping. However, it does not correspond to the formulas defined in the standards for this phenomenon (see, for example, Eurocode: EN1991-1-4 - Annex E: Vortex shedding and aeroelastic instabilities). Furthermore, the galloping should respond in a linear manner with the damping but, as it will be seen, this does not seem to be the case.

The similarity to flutter lies in the feedback between the deformation and the fluid dynamic forces produced by the air. Classical flutter requires the interaction of torsion and bending, and there is no appreciable deformation in the case we are studying, either along the longitudinal axis, or in the cross section. However, it is admitted that there are other types of flutter (Simiu and Scanlan 1996). For instance, as the field of aeronautics states, stall flutter bending is of little importance with respect to torsion. The difference with the behavior of this instability in wings and blades is that the flow separation is more like vortex shedding than a normal airfoil stall.

In view of the above, this phenomenon could be classified as a special type of one degree of freedom torsional flutter. Despite that, some authors prefer to refer to this phenomenon as torsional galloping, and that seems to be the most accepted name in the industry.

3.2 Critical velocity of the torsional galloping

Fig. 13 shows the behavior of the free end of the tracker (with a horizontal starting position, 0° tilt angle) as a function of speed. This behavior is directly related to the momentum in the driver by the stiffness of the structure. The mean value of the angle at the free end of the tracker and the amplitude of the oscillation over this mean value are depicted.

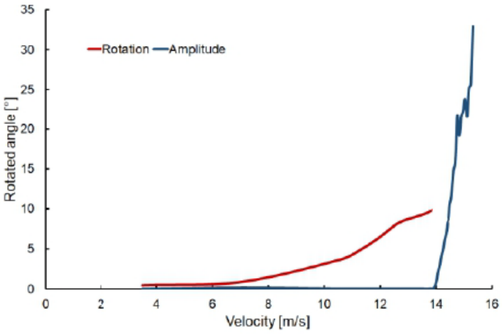

Fig. 13 Mean rotation and amplitude of the angular oscillation at the free end (tilt angle 0º)

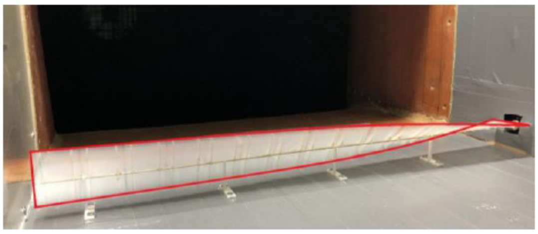

Fig. 14 Shaft's twist of the aeroelastic scale model during torsional galloping

Up to a speed of about 14 m/s, there is no oscillation, and the angle at the free end increases with speed as the wind load distributed along the tracker increases. The torsional deformation of the torque tube allows a relatively little rotation of the entire panel (the PV panels) from the drive end to the free end.

When the instability identified as torsional galloping begins, an oscillation is produced, with an amplitude that grows very fast with the wind speed. The amplitude of the oscillation varies along the axis of the solar tracker from zero at the driver section to its maximum value at the free end, producing a longitudinal sinusoidal twist of the panel (in contrast with a linear distribution when the momentum is concentrated at the free end), see Fig. 14.

In the beginning of the oscillation, the amplitude may be small but, when the velocity increases, the amplitude intensifies exponentially. If the solar tracker is maintained in the range of oscillations of small amplitude, fatigue effects may appear in the structure. However, with a small increase in the wind velocity, larger amplitudes will appear, generating loads on the structure (much higher than the static and dynamic loads usually considered), and the solar tracker easily reaches structural collapse.

For this research, the most important part of the wind tunnel tests is to find the critical velocity at which the torsional galloping phenomenon appears.

The critical galloping velocity (U_{cr}) is taken from the speed at which the galloping can be triggered, whatever the cause or source of the initial instability that generates the aeroelastic event. Fig. 13 illustrates the sudden increase of the amplitude of the oscillation from 13.9 m/s upward. Due to the slope at this point (about 21° per m/s), the precision with which this speed can be determined is greater than 1%.

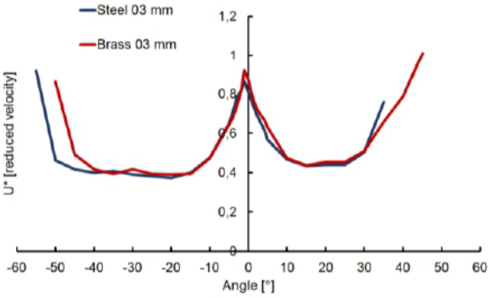

Fig. 15 Stability Diagram. Critical reduced velocity as a function of the tilt angles

It has been found that, sometimes, the onset of galloping can be delayed to velocities somewhat above critical, although when it falls into galloping, it goes directly into the oscillations of that higher speed. This effect is believed to be related to friction in the supports and increases if there are bending loads due to misalignments of the torque tube. However, that this delay is seen to be reduced if there is greater turbulence in the flow or if the tracker experiences a forced oscillation.

To avoid these effects and to find the minimum possible speed for the start of the galloping, the following experimental procedure has been followed: for each test, the speed is increased until the tracker goes into advanced galloping; from then on, the speed is reduced until the oscillation disappears. It has been found that, when approaching this point with the tracker oscillating, when it stops vibrating, it does not fall back into galloping, neither by increasing the turbulence, nor in the presence of gusts, nor even with externally forced oscillations.

The critical velocity depends on the tilt angle of the solar tracker. The entire speed range has been examined until instability is found, and measurements have been made for all angular tilts (from +75° to -75°) every 5°, and every 1º in the area near the horizontal. This has also allowed a detailed study around the classic stow positions, close to 0º tilt. Fig. 15 shows the found values, expressed as non-dimensional reduced velocity, in the so-called Stability Diagram:

The reduced velocity corresponds to the dimensionless wind speed taking into account the chord and the natural frequency (radians/s), Eq. (14)

$$U^* = \frac{U}{b}\frac{2}{\pi}\sqrt{\frac{I}{K}} \tag{14}$$

The oscillation phenomenon does not appear on every tilt angle, it is restricted between approximately +50° and -55° degrees. The minimum critical velocities show up in the range of -45° to -15° and from 20° to 40°, this velocity is more or less uniform in these ranges, with a value of 0.37 on the negative side and 0.43 for the positive one. For tilt angles close to zero, the critical velocities are higher, up to 0.86 for an angle of -1°. The maximum value is not centered at zero due to the asymmetry induced by the ground. The critical velocities also increase at the extreme angles (± 50°), where the forced oscillation disappears.

The plot behavior shows several aspects of the phenomenon:

- Considering the stable velocity for the angles ranging from -45° to -15° and from 20° to 40°, it seems to indicate that a certain kinetic energy is necessary for the oscillatory phenomenon to develop.
- For small tilt angles, between approximately -10° and +5°, the critical velocity is considerably higher. It is known that a flat plate with small angles of inclination does not shows the vortex shedding phenomenon (Blevins 1990). However, due to the flexibility of structure, as the velocity increases, the angle of the free end deviates with respect to the end of the driver; the higher the velocity, the bigger the difference. For example, if the tilt position of the model solar tracker is 5°, when the wind velocity is 10 m/s, the free end angle is about 8°or 9°. What it means is that vortex shedding can be triggered on the free end with a velocity high enough, even at small tilt angles. It may be assumed that, if this velocity is sufficient for the necessary kinetic energy, the tracker will then go into the torsional galloping phenomenon.
- When the absolute value of the azimuthal angles is high enough, the torsional galloping phenomenon does not activate. It is possible that the flow detachment at the leading or trailing edge close to the ground may be much less energetic and is not sufficient to develop the instability. Or perhaps, the lack of symmetry makes more difficult the beginning of the instability.

Another aspect of the experimental results is that the values for the critical reduced velocity are basically the same on the two tested models in spite of the difference of the shaft's torsional stiffness (*K*). This is believed to be a consequence of the reduced velocity maintaining the dimensionless torsional stiffness coefficient (C_k). In other words, both tests keep the similarity with respect to the stiffness.

Only models with the same value of moment of inertia (*I*) have been tested, so it is still unknown its possible effect on the galloping critical velocity.

The damping ratio (ζ) values in both models are quite different but both are also quite small. Although not included in this work, other tests with different materials have been carried out, and the preliminary results corroborate the idea that, when the damping ratio is small, it has little influence on the onset of torsional galloping.

4. Discussion

4.1 Design values for wind speed and stiffness of the torque tube

The previous analysis and experimental results allow to calculate the maximum wind velocity that a specific prototype of solar tracker will stand before the onset of the torsional galloping.

For instance, for the prototype of solar tracker in this study, if the threshold value of the critical reduced velocity is set to 0.37, the galloping critical velocity is, Eq. (15)

$$U_{cr} = U_{cr}^{*} \cdot \frac{b \cdot \pi}{2} \cdot \sqrt{\frac{K}{I}} \approx 14.4\ m/s \tag{15}$$

Alternatively, it is also possible to calculate the shaft stiffness for a specified critical galloping velocity or maximum project wind speed, for example, for 100 km/h, as shown in the Eq. (16)

$$K_{cr} = \frac{U_{cr}^{2}}{U_{cr}^{*2}} \frac{4I}{b^{2}\pi^{2}} = \approx\ 423356\ Nm \tag{16}$$

Which corresponds to a shaft thickness of 33 mm, instead of the 6 mm of the original prototype.

Normally, operation procedure in a photovoltaic facility calls for the solar tracker to assume a stow position when the wind is above a certain value; usually zero or a slightly negative tilt angle. In that case, the critical reduced velocity can reach a value around 0.8. This corresponds to a galloping critical velocity of 31 m/s, for the original prototype, or for a shaft thickness of 5 mm to withstand up to 100 km/h.

4.2 Critical velocity of the torsional galloping

The data in Fig. 15 are considered conservative, and suitable for this tracker (and any other fitting the similarity laws) with a uniform, steady and frontal wind. Based on this, some considerations can be made about other aspects that have influence on this problem.

The real wind is not uniform and continuous. Depending on the weather or the terrain conditions, there may be a strong influence of turbulence and gusts (buffeting). As mentioned above, the experimental procedure followed in this research ensures that no continuous galloping occurs if the wind speed is below the critical velocity. However, the absence of transient vibrations is not guaranteed. Due to this, the presence of strong turbulence or gusts may make it necessary to increase the design speed (Jia 2011).

An analogous reasoning can be made for the atmospheric boundary layer. Its presence decreases the average speed at the height of the tracker, so - in theory - the design speed of torsional galloping could be decreased (Fan 2020). However, in the boundary layer there may be more turbulence, and it may also be highly variable with weather conditions. This may make it convenient to take the design speed at a certain height above the trackers.

Regarding the position of the tracker in the row, the scale model is placed in the tunnel between two walls, which makes it is equivalent to an interior tracker. Some tests have been done with a tracker where the free end does not have an adjacent wall, which would be equivalent to a position at the end of the row. It has been found that, under these conditions, the edge effects cause the oscillation to be slightly reduced and the critical velocity to increase. The critical velocity data obtained would be on the safety side for these trackers.

No wind direction tests have been performed. It has been assumed that the most severe effects occur when considering the wind speed normal to the tracker, but this factor deserves further investigation.

As mentioned above, the studied tracker would correspond to a tracker in the front row. On the one hand these are the most exposed trackers, but, on the other hand, the behavior of one row can affect the following ones.

The performance of a multi-row system, as designed for solar plants, is currently being tested. It has been found that if there are two rows of trackers, under some singular conditions, the second one may fall into galloping before the first one starts to oscillate. It needs further study, but this is believed to occur when the trackers are in a position close to horizontal, where the critical velocity is higher. Under these circumstances, the first tracker can change the angle of the flow over the second tracker to an area with a lower critical velocity in the Stability Diagram.

In any case, if the critical velocity is less than the minimum possible (according to Fig. 15), they should not reach the galloping, at least not continuously.

However, this may indicate that a stow position close to the horizontal may not be a good method to consider higher critical velocities than the minimum.

Apart from the above, the wake of the trackers may generate buffeting or wake induced vibrations in the rear rows, but that is outside the scope of this study.

5. Conclusions

An analytical and experimental analysis of the aeroelastic instabilities of a single-axis solar tracker has been carried out. The analytical procedure has led to identify and evaluate the dimensionless variables most relevant for the phenomenon. Based on this study, several aeroelastic scale models have been designed, built and tested in a wind tunnel. The models have been able to reproduce the phenomenon of torsional galloping that appears when wind velocities reach relatively high values.

- The results suggest that in order for torsional galloping to occur, two conditions must be met: the angle of the solar tracker has to be adequate for vortex shedding; and the flow must have a certain minimum kinetic energy.
- The measurements have allow to determine the galloping critical velocities for the whole practical range of tilt (azimuthal) positions.
- It has been found that the critical reduced velocity for instability exhibits a minimum that changes little on a wide range of the tilt angle. That minimum can be set as a limit for stable operation.
- The stability range is higher when the tilt is close to horizontal since the critical velocity increases significantly. In addition, there are certain positive and negative tilt angles from which the instability no longer develops.
- The threshold value of the critical reduced velocity has been used to determine the wind speed at which aeroelastic instabilities start to develop, as well as the necessary shaft thickness for a given project wind speed.
- The results of the critical velocity have been obtained for a continuous, uniform and frontal wind speed. The experimental procedure allows to assume that those values are on the safety side to prevent torsional galloping with respect to the effects of other factors such as the atmospheric boundary layer, turbulence and gusts. However, configurations of multi-row trackers need to be further investigated. Also, the data found is only valid for the tracker studied, and those that meet the conditions of similarity.

Acknowledgments

This research has been developed in the framework of the FC-GRUPIN- IDI/2018/000205 project, supported by the "Principado de Asturias - Plan de Ciencia, Tecnología e Innovación", co-financed by FEDER funds.

References

Aydogdu, M., Arda, M. and Filiz, S. (2018), "Vibration of axially functionally graded nano rods and beams with a variable nonlocal parameter", *Adv. Nano Res.*, **6**(3), 257-278. https://doi.org/10.12989/anr.2018.6.3.257.

Blevins, R.D. (1990), *Flow-Induced Vibration*, 2nd Edition, Van Nostrand Reinhold Co., New York, NY, USA.

Dyrbye, C. and Hansen, S.O. (1997), *Wind Loads on Structures*, John Wiley & Sons, Ltd., Baffins Lane Chichester, Sussex, UK.

Ebrahimi, F., Barati, M.R. and Civalek, O. (2020), "Application of Chebyshev-Ritz method for static stability and vibration analysis of nonlocal microstructure-dependent nanostructures", *Eng. Comput.*, **36**, 953-964. https://doi.org/10.1007/s00366-019-00742-z.

Fan, X., Wang, Z., Chen, X., Wang, Y. and Tan, W. (2020), "Experimental investigation on flow-induced vibration of flexible multi cylinders in atmospheric boundary layer", *Int. J. Mech. Sci.*, **183**, 105815. https://doi.org/10.1016/j.ijmecsci.2020.105815.

Jia, J. (2011), "Wind and structural modelling for an accurate fatigue life assessment of tubular structures", *Eng. Struct.*, **33**, 477-491. https://doi.org/10.1016/j.engstruct.2010.11.004.

Jubayer, C.M. and Hangan, H. (2015), "Numerical simulation of wind effects on a stand-alone ground mounted Photovoltaic (PV) system", *J. Wind. Eng. Ind. Aerodyn.*, **134**, 1-37. https://doi.org/10.1016/j.jweia.2014.08.008.

Katariya, P.V. and Panda, S.K. (2019), "Numerical frequency analysis of skew sandwich layered composite shell structures under thermal environment including shear deformation effects", *Struct. Eng. Mech.*, **71**(6), 657-668. https://doi.org/10.12989/sem.2019.71.6.657.

Lave, M. and Kleissl, J. (2011), "Optimum fixed orientations and benefits of tracking for capturing solar radiation in the continental", *Renew. Energy*, **36**, 1145-52. https://doi.org/10.1016/j.renene.2010.07.032.

Mohammadnejad, M. (2015), "A new analytical approach for determination of flexural, axial and torsional natural frequencies of beams", *Struct. Eng. Mech.*, **55**(3), 655-674. https://doi.org/10.12989/SEM.2015.55.3.655.

Païdoussis, M.P., Price, S.J. and De Langre, E. (2011), *Fluid Structure Interaction: Cross Flow Induced Instabilities*, Cambridge University Press, Cambridge, UK.

Rao, S.S. (2007), *Vibration of Continuous Systems*, Wiley, New York.

Rodríguez Lastra, M., Fernández Oro, J.M., Galdo Vega, M., Blanco Marigorta, E. and Santolaria Morros, C. (2013), "Novel design and experimental validation of a contraction nozzle for aerodynamic measurements in a subsonic wind tunnel", *J.*

Wind. Eng. Ind. Aerodyn., **118**(3), 5-43. https://doi.org/10.1016/j.jweia.2013.04.008.

Roedel, A. and Upfill-Brown, S. (2018), “Designing for the Wind, using dynamic wind analysis and protective stow strategies to lower solar tracker lifetime costs”, White Paper, NEXTracker.

Rohr, C., Bourke, P.A. and Banks, D. (2015), “Torsional instability of single-axis solar tracking systems”, *Proc. 14th Int. Conf. Wind. Eng.*, Porto Alegre Brazil, June.

Simiu, E. and Scanlan, R.H. (1996), *Wind Effects on Structures: Fundamentals and Applications to Design*, 3th Edition, John Wiley & Sons, Ltd., New York, NY, USA.

Strobel, K. and Banks, D. (2014), “Effects of vortex shedding in arrays of long inclined flat plates and ramifications for ground-mounted photovoltaic arrays”, *J. Wind. Eng. Ind. Aerodyn.*, **133**, 146-149. https://doi.org/10.1016/j.jweia.2014.06.013.

Talavera, D.L., Muñoz-Cerón, E., Ferrer-Rodríguez, J.P. and Pérez-Higueras, P.J. (2019), “Assessment of cost-competitiveness and profitability of fixed and tracking photovoltaic systems: the case of five specific sites”, *Renew. Energy*, **134**, 902-913. https://doi.org/10.1016/j.renene.2018.11.091.

Taylor, Z.J. and Browne, M.T.L. (2020), “Hybrid pressure integration and buffeting analysis for multi-row wind loading in an array of single-axis trackers”, *J. Wind. Eng. Ind. Aerodyn.*, **197**, 104056. https://doi.org/10.1016/j.jweia.2019.104056.

Yang, Y. (2010), “Experimental investigations of vortex induced vibration of a flat plate in pitch oscillation”, M.Eng. Dissertation, A&M University, Texas.

PL

Notations

b	Panel chord
c	Structural damping
C_k	Torsional stiffness coefficient
C_T	Torque coefficient
f,g	Function of
h	Height of the torque tube over the ground
I	Moment of inertia respect to the axis
K	Tracker torsional stiffness
L	Structure characteristic length
Re	Reynolds number
St	Strouhal number
T	Torque magnitude
TI	Turbulence intensity
U	Wind speed
y	Height along the test section over the ground
z	Total height -equal to width- of the test section
θ	Angle
μ	Air dynamic viscosity
ρ	Air density
ω	Frequency
ξ	Damping ratio
Subscripts	
cr	critical
m	model
max	maximum
n	cycles number
p	prototype
0	natural frequency (first mode of vibration)
Superscripts	
*	reduced

2.3. Métricas del artículo

ARTÍCULO. 1

Revista	Structural Engineering and Mechanics
Título	Experimental determination of the resistance of a single-axis solar tracker to torsional galloping
Cuartil	Q2
Factor de impacto (JCR)	2.998
Citescore (Scopus)	5
N° citas [junio 2021-octubre 2024] (Web of Science)	16

Capítulo 3: Influencia de la inercia y la relación de aspecto en el galope torsional de seguidores solares monoeje

3.1. Descripción del artículo

El artículo investiga la influencia de la inercia y la relación de aspecto en el galope torsional de seguidores solares de un solo eje, un fenómeno en el que las oscilaciones inducidas por el viento pueden llevar al colapso estructural. Mediante pruebas en túneles de viento con modelos a escala, se determina la velocidad crítica a la que se produce esta inestabilidad, y que esta varía con el ángulo de inclinación, pero no está significativamente afectada por la inercia o la relación de aspecto del panel. Un hallazgo clave es que la velocidad crítica reducida permanece constante, lo que sugiere que la estabilidad depende más de la rigidez torsional y la interacción aerodinámica que de las propiedades geométricas. En este contexto, la creación de un diagrama de estabilidad es fundamental, ya que este permite visualizar y prever las velocidades críticas para distintos ángulos de inclinación, proporcionando una herramienta crucial para el diseño de seguidores solares. Este diagrama facilita la identificación de los ángulos más vulnerables y permite optimizar las dimensiones y la rigidez de los seguidores. El estudio sugiere que los seguidores más cortos son más estables ante el galope torsional, aunque presentan mayores cargas por unidad de longitud. La investigación concluye que la velocidad crítica reducida es el parámetro esencial para evitar inestabilidades, estableciendo directrices claras para el diseño seguro y eficiente de seguidores solares que puedan resistir condiciones de viento adversas. Estos hallazgos ofrecen una base sólida para mejorar la seguridad y durabilidad de los sistemas de energía solar.

3.2. Publicación en revista revisada por pares

Influencia de la inercia y la relación de aspecto en el galope torsional de seguidores solares monoeje

Engineering Structures 243 (2021) 112682

Contents lists available at ScienceDirect

Engineering Structures

journal homepage: www.elsevier.com/locate/engstruct

Influence of inertia and aspect ratio on the torsional galloping of single-axis solar trackers

Eva Martínez-García, Eduardo Blanco-Marigorta, Jorge Parrondo Gayo, Antonio Navarro-Manso *

Energy Department, University of Oviedo, Gijón, Spain

A R T I C L E I N F O

Keywords:
Single-axis tracker
Wind load
Aeroelastic model
Torsional galloping
Stability diagram
Wind tunnel

A B S T R A C T

Single-axis solar trackers are currently one of the cheapest systems for electricity generation. However, they may have to face significant maintenance costs depending on environmental and climatic factors. Weather is believed to provoke approximately half of the damages registered in solar tracker systems, and a large part of them are due to dynamic wind load. Torsional galloping – or, more precisely, flutter with one degree of freedom – is a phenomenon that arises when the wind speed exceeds a certain critical value. It causes the tracker to undergo angular oscillations with increasing amplitude until the structure collapses. The phenomenon is intrinsically linked to geometric and structural parameters, some of which exhibit a wide range of variation in the current market, depending on the configuration and design of the trackers. This article presents an analytical and experimental study on how the onset of torsional galloping is influenced by the inertia of the modules and the aspect ratio of the panel; it also includes the effect of the torque tube stiffness. The analytical study starts from the equation of motion involving the aeroelastic derivatives and the torque equation in differential form. Tests have been conducted on aeroelastic models of the structures of interest. It has been found that the critical reduced velocity of galloping changes with tilt angle, but it is essentially independent of the main structural parameters: torsional stiffness, inertia and aspect ratio. The results are finally presented in a Stability Diagram for the correct and optimal dimensioning of these structures against torsional galloping.

1. Introduction

In 2019, the solar tracker market grew by 62% reaching an installed capacity of 23 GWh. Based on those data, technological improvements and energy demand forecasts, that renewable source is expected to grow by 11% per year until 2024 [1].

At present, solar utility-scale installations (see Fig. 1) have one of the lowest levelized costs of electricity production (LCOE) in the renewable energy sector [2]. It is expected that it will soon become the energy source with lowest LCOE of all systems used in the market [3].

This is due to the improvement of the photovoltaic panels and trackers. In the first case, as a result of increased performance and cost reduction due to optimization of the production systems; in the second case, through cost reduction achieved by adjustment of the structural design [4,5].

In this particular, the single-axis photovoltaic solar trackers stand out with an increase in efficiency between 10% and 30% with respect to the fixed panels, depending on the geographical and climatic conditions [6–8].

These structures are composed of a torque-tube oriented north to south, on which the solar panels are mounted. Progressive rotation of that tube (tilt angle) allows the panels to always face the sun direction. The structure is symmetrical with respect to the central driver, which constitutes a fixed point for torsion. The tube is supported by several intermediate pillars that preclude horizontal and vertical motion but allow for free rotation. Fig. 2 shows a structural scheme and details of a common solar tracker.

This structure behaves like a torsion embedded beam, whose torsion constant is defined by the torque-tube; this shaft normally has circular, rectangular or hexagonal cross-sections, with relatively large diameters and small thicknesses to increase rigidity. The inertia, however, is defined by the panels themselves plus the frame that joins them (beams and struts) [9]. The height of the tube above the ground is approximately half the total width of the tracker panel. Fig. 3 shows a simulation image of a tracker by means of Finite Element Method (FEM), which

---

* Corresponding author.
E-mail address: navarroantonio@uniovi.es (A. Navarro-Manso).

https://doi.org/10.1016/j.engstruct.2021.112682
Received 13 November 2020; Received in revised form 25 March 2021; Accepted 3 June 2021
Available online 20 June 2021

Nomenclature

List of symbols

$A^*_{i,2,3}$	Aeroelastic derivatives
a	Ratio of lengths
b	Panel chord
C	Limit relationship of e/D for the buckling limit
C_{I0}	Inertia coefficient per unit length
Ck	Torsional stiffness coefficient
D	Diameter of the torque-tube (middle)
D_e	External diameter of the torque-tube
D_i	Internal diameter of the torque-tube
E	Elasticity module
e	Thickness of the torque-tube
G	Shear module
I	Moment of inertia respect to the axis
I_0	Moment of inertia respect to the axis per unit length
J	Polar moment of inertia
K	Reduced frequency
k	Tracker torsional stiffness
L	Structure characteristic length
M	Aerodynamic torque per unit length
m	Total mass of the modules
R	Radius of the torque tube
T	Torque magnitude
t	time variable
TI	Turbulence intensity
U	Wind speed
U^*	Reduced velocity
U_{cr}	Critical velocity
x	Length variable
θ	Angle displacement variable
ρ	Air density
τ_{xy}	Cross section shear tension
υ	Poisson ratio
ω_0	Natural circular frequency
ξ	Damping ratio

Fig. 1. Solar tracker plant.

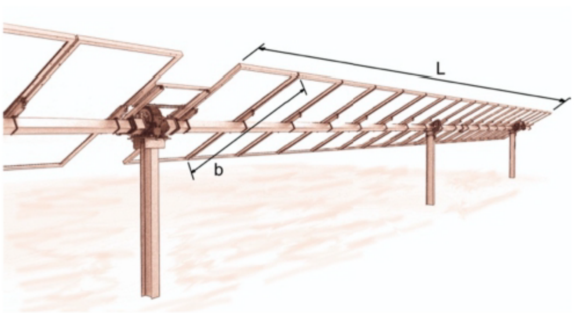

Fig. 2. Structural scheme of the solar tracker.

can be used to analyze the influence of the most important structural parameters on the deformation, the natural modes of vibration, etc.

Weather action and climatic events accounts for 49.8% of the causes of structural breakage or collapse of these structures [10]. Among them, one of the main problems they stand is the wind loads. Due to the fact that trackers have evolved to become rather slender structures (for economic reasons), they are now prone to suffer aeroelastic effects. This implies that the usual static design criteria are not valid when the structure begins to exhibit oscillations, not even if considering a dynamic amplification factor (DAF) [11–14]. Furthermore, international standards do not yet specifically include this type of structure nor the aeroelastic phenomena that may affect them.

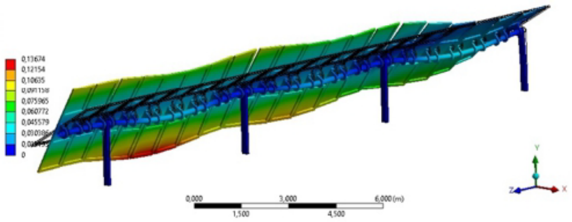

Fig. 3. Example of FEM analysis of the first natural mode of vibration.

There have been numerous studies on the aerodynamic forces in structures such as heliostats and solar panels with a limited aspect ratio, such as [15,16], and also, on the aerodynamic forces in solar arrays, including DAFs, as for example in [17–19].

In particular, one of the most destructive phenomena, which affects many single-axis solar tracker structures, has been identified to be the one degree of freedom flutter (1DOF), commonly called torsional galloping in this industry sector [20–22]. This phenomenon manifests in that, when wind speed exceeds a certain critical value, the tracker begins to vibrate in the first torsional mode of the structure. The amplitude grows rapidly with the wind speed, until the structure collapses due to the breakage of one of its elements.

To date, however, publications on the phenomenon of torsional galloping in single-axis solar trackers are very scarce. Some authors [11] described the phenomenon and explained with some detail the case of initial tilt angle close to 0°. They also shown some preliminary results of a numerical model validated with an experimental sectional model.

More recently [23], a study on the dynamic forces on these structures has been conducted, by means of a new method that combines aeroelastic measurements in a sectional model with numerical calculations. Although this study was not really focused on instability but on the analysis of buffeting for multi-row trackers, they determined the aeroelastic derivatives to be integrated in their calculation method.

Finally, it has been found that the critical wind speed at which the instability begins is a function of the tilt angle of the solar tracker [24]. In the stability diagram of Fig. 4 which represents the wind speeds that cause aeroelastic instability for each initial position, the lowest values are found for positive angles close to 20° and a broader range of negative angles, from −15° to −40°. For angles near 0° the critical velocity reaches a somewhat higher value, and for angles higher than 40° or lower than −50° the critical velocity increases rapidly, and the phenomenon even disappears.

However, that set of results has not yet become part of the standards, and there is insufficient data for a reliable design of these structures against aeroelastic effects. As a contribution to fill that gap, an in-depth study is now presented on the critical velocity at which the instability begins over the operating range of angular positions.

This paper first examines the structural characteristics of the single axis solar trackers on the market and describes the dimensionless parameters and aeroelastic variables involved in the phenomenon. This is followed by a description of the experimental procedure used to study the galloping on a series of scale models of trackers with different inertias and aspect ratios. In the next section, the results for each of these two variables are analyzed and the hypotheses used are discussed, as well as the transformation relationships between trackers. Finally, the stability diagram consisting of the determination of the reduced critical speed for each tilt is shown and a study of the optimization of the dimensions to minimize the risk of galloping is made.

2. Structural characteristics

Table 1 lists a wide range of standard configurations of solar trackers on the market. It shows the following parameters: the total length *2·L* and width *b* of the tracker-panel, its inertia, the type of photovoltaic modules and the total number *N* of modules mounted on the tracker-panel. The most common modules have dimensions of about 1 × 2 m. Typical module layouts are: 1MIP (1 module in portrait), with a width of approximately 2 m, and 2MIP with a width of approximately 4 m. It is also possible to find 3MIL layouts (3 modules in landscape) and even install 0.5 × 1 m modules in 6MIL layout.

As for the type, the main division between the solar modules that are installed is made in relation to their economic efficiency and their weight: crystalline panels and thin film (Tf). In turn, for the crystalline ones, although they can be divided into monocrystalline and polycrystalline, the parameter that most affects their mass is the mono (1F) or bifacial (2F) configuration. The usual weight of these panels is between 10 and 15 kg/m^2.

The main structural properties that influence the galloping critical velocity are the stiffness *k*, the inertia *I*, the damping ratio ξ and the geometry configuration. The main geometrical parameter is the aspect ratio, *AR*, although other factors that can affect the phenomenon include the height of the axis above the floor, the separation between panels and the torque tube, the dimensions of the struts (depth and width) and the separation between the panels.

Table 1
Characteristics of commercial trackers.

Id	Type	Num. modules	b (m)	2L (m)	I (kg·m^2)
1	1F	60	3.0	40	704
2	2F	90	4.0	45	2127
3	Tf	90	4.0	45	1495
4	1F	90	4.3	47	2274
5	1F	270	3.6	54	2072
6	1F	90	4.0	55	2458
7	2F	120	4.0	60	2836
8	Tf	120	4.0	60	1994
9	1F	120	4.3	63	3033
10	2F	90	2.0	90	570
11	Tf	90	2.0	90	401
12	1F	90	2.1	94	604
13	1F	240	1.8	96	501
14	1F	78	2.0	96	570
15	2F	100	2.0	100	633
16	Tf	100	2.0	100	446
17	1F	100	2.1	107	651
18	2F	180	2.0	180	1140
19	Tf	180	2.0	180	802
20	1F	180	2.1	189	1209

The influence of the properties can be analyzed from the following equation describing the torsional movement of the structure per unit length [11]:

$$I_0\ddot{\theta} + 2I_0\xi\omega_0\dot{\theta} + \frac{k}{L}\theta = M \tag{1}$$

where I_0 is the torsional inertia per unit length, ω_0 is the natural circular frequency, and θ the angular displacement variable. The first term on the left of the equation corresponds to the inertial forces, the second term includes the effects of damping and the third term is the elastic forces, in this case torsional ones.

The right-hand term *M* is the aerodynamic torque per unit length. To study the beginning of the aeroelastic instability, these moments can be written as a function of the flutter derivatives according to [25]:

$$M = \frac{1}{2}\rho U^2 b^2 \left(K\frac{b}{U}A_2^*\dot{\theta} + K^2 A_3^*\theta \right)\# \tag{2}$$

where *K* is the reduced frequency (inverse of the reduced velocity), *b* a characteristic length (chord), *U* is the wind speed and A^*_i are the flutter derivatives or Scanlan coefficients involved in the decoupled two-dimensional torsion. The term with the first derivative of the angle is the aerodynamic damping, and the term that multiplies the angle is the aerodynamic stiffness. The A^*_i coefficients are purely aerodynamic and a function only of reduced velocity, i.e., for a given geometric shape of

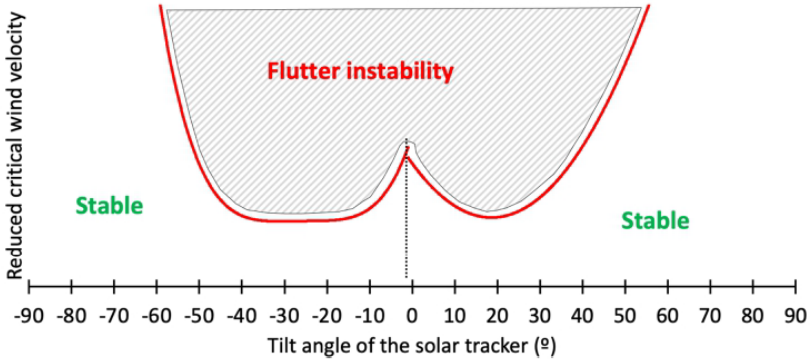

Fig. 4. Conceptual Stability Diagram of single-axis solar tracker.

the section, they are independent of the mass, stiffness, and structural damping of the design [26].

Putting together the structural and aerodynamic terms, the resulting differential equation will be unstable if the damping term is negative:

$$\xi - \frac{\rho U b^3 K A_2^*}{2 I_0 \omega_\theta} < 0\# \tag{3}$$

The critical velocity for torsional galloping could be obtained from this equation. In the case of solar trackers each initial angular position implies a different geometrical shape (different A^*_i), which means that the critical reduced velocity of galloping varies with the tilt.

As can be seen from Eq. (3), for an instability 1DOF to exist, A^*_2 must be positive. It is also observed (and has been proven in the experiments carried out in this research) that when the structural damping is small (<5%), it does not have a significant influence [11]. This is usually the case in steel structures such as solar trackers without external dampers.

Thus, it can be said that instability occurs when A^*_2 goes from negative to positive, which occurs at a fixed value of the reduced velocity. Therefore, this implies that the influence of the stiffness, inertia and the aspect ratio in the beginning of the instability occurs only through the reduced velocity.

To study the influence of the structural properties on the critical velocity of galloping, the dimensionless coefficients obtained from the inspectional analysis of Eq. (1) can be used: the damping coefficient ξ itself, and the torsional stiffness $C_k$and inertia C_{I0} coefficients.

$$C_k = \frac{k}{\frac{1}{2}\rho U^2 L^3}\# \tag{4}$$

$$C_{I0} = \frac{I_0}{\frac{1}{2}\rho L^4}\# \tag{5}$$

where U is the wind speed and L a characteristic length of the structure.

From Eq. (4), the relationship between the velocities between two similar trackers with different stiffness is:

$$U_2 = U_1\sqrt{\frac{k_2 L_1^3}{k_1 L_2^3}}\# \tag{6}$$

which gives the influence of the stiffness on the critical velocity.

However, the influence of the inertia and the damping ratio cannot be obtained directly from the laws of similarity, since they do not depend on U. The same happens regarding the aspect ratio because the geometric similarity is not maintained between models with different *AR*.

3. Experimental results

In order to study the influence of the structural characteristics on the galloping critical velocity, aeroelastic tests have been carried out on reduced models of the trackers, with different inertias and aspect ratios. The tests have been performed in the EB40-oWT open wind tunnel, at the Energy Department building of the University of Oviedo. The test section is 0.7 × 0.7 m^2, the maximum speed is about 35 m/s and the nominal power is 30 kW. Other details as well as the nozzle design can be found in [27].

Experiments were conducted under smooth flow conditions. Fig. 5 shows the velocity profile (vertical mid-plane, near the bottom wall), where it can be seen that the boundary layer is about 1 cm. The maximum turbulence intensity is 1.1% in the test section (outside de boundary layer).

Seven scale models were used for this study. The models are composed of up to 3 different materials to correctly reproduce their mechanical and structural characteristics. The shaft is a steel cylinder from 2 to 3 mm of diameter, and it is the responsible of the torsional stiffness of the model; the solar panel frame has been manufactured in PLA by 3D printing and several types of plastic films have been used for the solar panel in order to adjust the weight and corresponding inertia of these elements. The struts and pillars have also been manufactured in PLA.

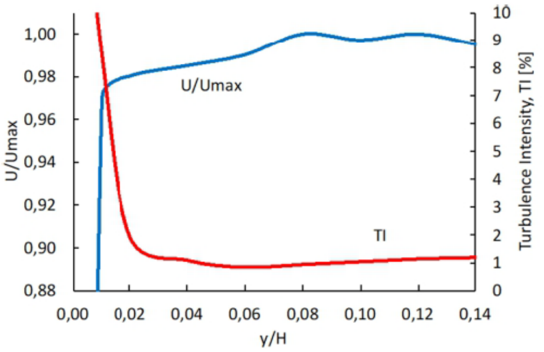

Fig. 5. Velocity ratio and turbulence intensity profiles at the outlet of the nozzle of the wind tunnel, near the wall.

The height of the torque-tube above the floor for all models is 1.15 times the semi-chord of the panel. The separation between solar panel and torque-tube is 0.15 times the semi-chord. These dimensions are an average of the values found in the prototypes studied. Table 2 shows the dimensions and structural characteristics of the scale models tested:

The structural damping of all models is less than 1%. Fig. 6 shows all the scale models built on the left, and the detail of assembly of the torque-tube, panels and pillars on the right.

The symmetry of the structure of the solar tracker has allowed to make models of half the length *L*, testing only one of the wings of the prototype, from free end to the driver section. This section corresponds to an embedded support (Fig. 7 a), where a force balance has been used to measure the torque. This instrument has 3 load cells (Fig. 7 b) with a range of 2.5 N·m. and accuracy of 0.73%.

The model's tilt positioning system uses a worm gear that allows an angular accuracy of 0.1 degrees (also Fig. 7 b). Tests have been made by changing the tilt angle every 5 degrees, except for positions close to zero, where the increment has been 1 degree. The measurement of the twisted angle (amplitude) at the free end of the tracker is done with a combination of high speed (1000 fps) video and digital photography together with technical drawing software; an accuracy of 0.25 degrees has been achieved.

The air speed in the test section is adjusted with a frequency converter in 0.1 Hz increments which translates into 0.07 m/s. Typical test speeds range from 6 to 15 m/s, with a Reynolds number around 10^5.

To determine the critical velocity of the instability, the velocity is increased until the model is clearly under galloping (see Fig. 8). Then the velocity is gradually lowered until the oscillation disappears (amplitude less than 0.25 degrees). In this way the critical velocity limit is approached with the tracker in motion, which minimizes the effects of static friction. For the experiments performed with this methodology, it

Table 2
Characteristics of the scale models.

Id	L (m)	b (m)	k (N·m)	I (kg·m^2)	ω_0 (Hz)
1	0.677	0.067	0.200	5.43E^{-6}	48.0
2	0.677	0.100	0.200	3.65E^{-5}	18.5
3	0.677	0.067	0.200	7.82E^{-6}	40.0
4	0.677	0.067	0.200	9.24E^{-6}	36.8
5	0.677	0.067	0.202	1.14E^{-5}	33.2
6	0.677	0.091	0.200	2.84E^{-5}	21.0
7	0.677	0.134	0.900	1.34E^{-4}	20.0

Fig. 6. Scale models tested and detail of the assembly.

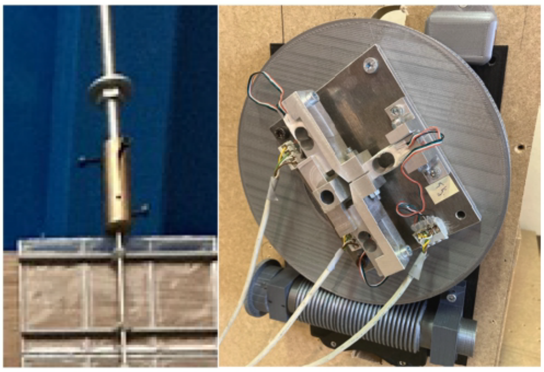

Fig. 7. Detail of the anchoring for the driver section (a) and initial tilt positioning system and balance (b).

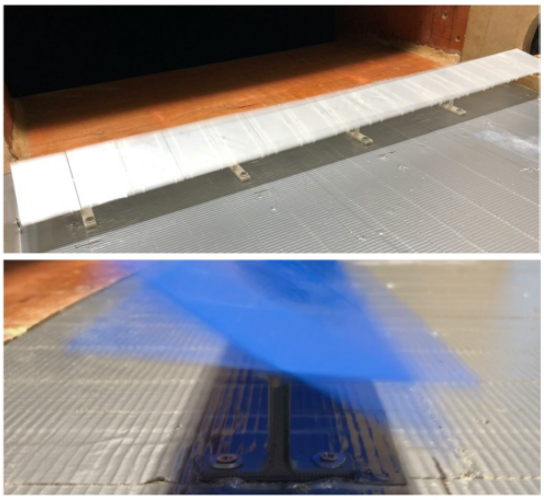

Fig. 8. Galloping of the scale model.

has also been found that this velocity is the minimum possible. That is to say, the structure does not fall into galloping for velocities lower than that, even in the face of increased turbulence or other aerodynamic instabilities. This procedure is repeated for each tilt (initial angular position) and the critical velocity values found allow the drawing stability diagram to be drawn. Fig. 9 shows the corresponding curve for the tracker that has been used as a basis for this study (Id 4 of Table 2):

Fig. 10 shows a power spectra cascade corresponding also to the base case, for −25° tilt, which clearly shows the onset of instability at a reduced velocity of 0.382.

The peak of the beginning of the oscillation occurs at about 33 Hz, while the structure's natural frequency in this case is higher, 36.8 Hz. This is because, unlike Vortex Induced Vibration (VIV), the frequency of the oscillation in flutter is influenced by the aerodynamic damping and stiffness.

Fig. 11 shows one of the models during galloping. The angular deformation can be seen, increasing from the driver to the maximum value of the amplitude at the free end.

In the tests, only one isolated structure was considered, which makes them equivalent to the first-row trackers of the solar plant. The trackers of the second and successive rows would be somewhat protected from the flutter by those of the first row, but being under the influence of the wake, makes them also susceptible to aeroelastic phenomena, and their study requires a specific analysis.

The models have been designed in such a way that they extend across the whole width of the test section and therefore reflect the behavior of a tracker in the middle of the row (the wall in the free end acting as a flow symmetry plane). Several tests have been carried out with the free end in the middle of the flow (simulating an end tracker) and it has been found that the critical velocity is slightly higher, especially for positive tilt angles. As with other structures, the tip effect reduces the aerodynamic forces in that area.

Some checks have also been made by increasing the turbulence in the test section up to 5% using intermediate grids; and it has been found that their effect does not substantially change the critical velocity, only raising it slightly for some tilts.

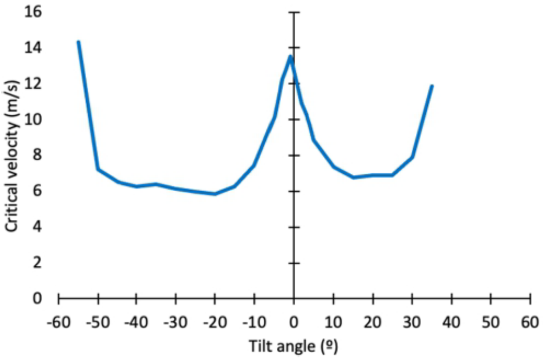

Fig. 9. Stability Diagram for a specific tracker.

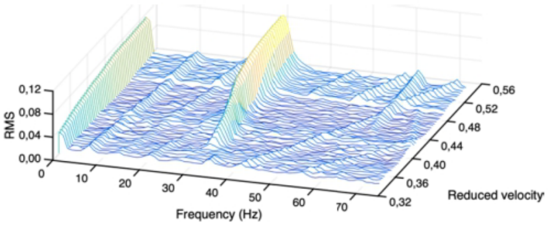

Fig. 10. Power spectra Id 4, tilt −25°, RMS torque vs. frequency and reduced velocity.

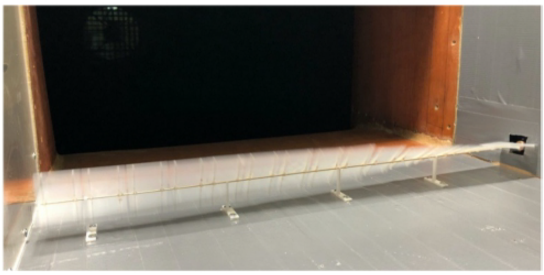

Fig. 11. Torsional deflection of the scale model.

Although it has not been specifically studied, the effect of the atmospheric boundary layer on this type of aeroelastic phenomena comes mainly from the reduction of the wind speed at the height of the structure, which implies an increase in the critical velocity [28].

4. Analysis of the influence of the inertia and the aspect ratio

For the tracker models and their associated fluid-dynamic phenomena to be fully similar, in addition to the geometric similarity and the non-dimensional stiffness coefficient, the non-dimensional inertia coefficient C_{I0}, Eq. (5) must also be maintained. According to this coefficient, the relationship between their inertias must satisfy:

$$I_{02} = I_{01}\frac{L_2^4}{L_1^4}\# \tag{7}$$

Unlike the ratio obtained for torsional stiffness, Eq. (6), only the dimensions ratio appears in this expression, so it does not allow to calculate the influence of the inertia on the critical velocity. For instance, if two trackers have the same geometrical dimensions then, for them to be similar, they should have the same inertia. If the inertia is different, they are not strictly similar, although the fluid-dynamic phenomenon may be of the same nature.

The typical inertias of the real trackers are shown in Table 1. However, to properly reflect the differences in length, it is more correct to utilize the coefficient of inertia per unit length C_{I0}. In the actual trackers studied, this coefficient varies between 0.44 and 1.63 (see Fig. 12). Lower values generally correspond to shorter tracker lengths, and vice-versa.

The models that have been tested to determine the influence of the inertia correspond to the Id 1 to 5 of Table 2, which have values of the inertia coefficient between 0.66 and 1.38. Regarding the torsional galloping critical velocity of these models, it has been found that the lower the inertia, the higher the critical velocity.

To be able to compare the different models with each other, the reduced velocity is used. This velocity has been calculated dividing by the width of the panel and the frequency of these structures:

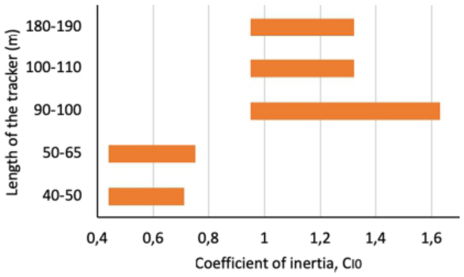

Fig. 12. Histogram of the coefficient of inertia C_{I0} as a function of the length of the tracker.

$$U^* = \frac{U}{b\omega_0} = \frac{U}{b}\frac{2}{\pi}\sqrt{\frac{I}{k}}\# \tag{8}$$

The results nondimensionalized in this way are shown in Fig. 13:

The average value of the differences between the curves (RMS) is less than 5% and is as low as 1% to 2% at the tilt angles where the minimum critical velocities are found. Obviously, the models are not similar because the inertia is different even though they have the same geometry. However, the results indicate that the reduced velocity of galloping is the same for all of them. And not only the starting point but, once the instability starts, the behavior also seems to be closely linked to the reduced velocity, with no direct dependence on inertia.

Fig. 14 shows the amplitude of the torque oscillation at the fixed end (driver) as a function of reduced wind velocity. Several models with different inertia are shown, all for a tilt angle of −25°. In the same Fig. 14 there are also the frequencies (dashed lines) at which the oscillation is produced. They are about 10 to 15% lower than the natural frequency of each tracker. This difference is mainly due to the aerodynamic rigidity. The frequencies remain fairly constant, at least in the galloping range studied, which covers about ±20° of amplitude at the free end of the tracker.

With the aspect ratio something similar to inertia happens: two trackers with different aspect ratios cannot be similar because they do not fulfill the geometrical relations.

To study its influence, the torsion equation for continuous media in partial derivatives with variation over length and time (without the damping term) is used [29]:

$$GJ\frac{\partial^2\theta(x,t)}{\partial x^2} + M(x,t) = I_0\frac{\partial^2\theta(x,t)}{\partial t^2}\# \tag{9}$$

where *θ(x,t)* is the angular displacement of the cross section, *M(x,t)* is the external torque on the axis per unit length due to the action of the wind, I_0 is the moment of inertia per unit length, *G* is the shear module and *J* is the polar moment of inertia of the cross section of the axis.

The aspect ratio of single-axis solar trackers is large (>5). In

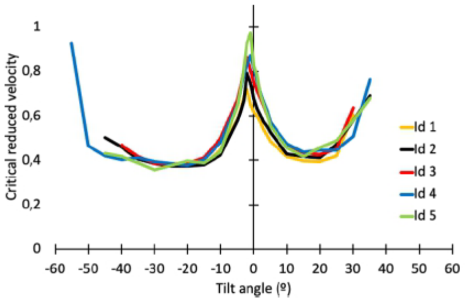

Fig. 13. Critical reduced velocities for scale models with different inertia.

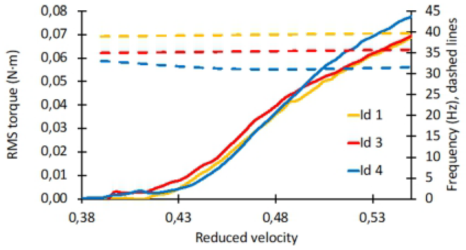

Fig. 14. RMS of torque and frequency (dashed lines) vs. reduced critical velocity.

addition, for structures in the middle of the row there is no tip effect. This gives the phenomenon a quasi-bidimensional aspect, despite the twisting along the axis. Then, if a tracker is considered, with the same cross section as another but with a shorter length, and if the angle rotated at the end of both structures is identical, it could be assumed that the phenomenon is the same but compressed. That is, the aerodynamic forces per unit length of tracker are the same in both structures, but in different longitudinal coordinates.

In other words, the hypothesis is based on the assumption that the three-dimensional structure of the fluid-structure interaction can be decomposed into a continuous differential phenomenon and that an integration of the aeroelastic forces over trackers of different lengths can be made basically changing the length variable. This does not mean that three-dimensional phenomena, such as vortex shedding and others, do not exist, but that the integral results of the forces on the driver are equivalent.

Applying the above to Eq. (9), consider two trackers, one of length L and one with a smaller length L'; if the variation in length is treated as a change in variable: ($x' = x/a$), the hypothesis implies that *if* $\theta(x) = \theta'(x')$ then $M(x) = M'(x')$. Performing the change of variable:

$$GJ\frac{1}{a^2}\frac{\partial^2\theta'(x',t)}{\partial x'^2}+M'(x',t)=I_0\frac{\partial^2\theta'(x',t)}{\partial t^2}\# \tag{10}$$

which would be the same as the equation of the tracker of length L' if its inertia per unit length I'_0 was equal to that of the tracker of length L (I_0) and its polar module J' was equal to J/a^2. In that case, the relation between total inertias would be:

$$I' = \frac{I}{a}\# \tag{11}$$

And, as the stiffness can be written as a function of the shear module and the polar module:

$$Gk = \frac{GJ}{L}\# \tag{12}$$

the relationship of stiffness would be:

$$k' = \frac{GJ'}{L'} = \frac{GJ}{La} = \frac{k}{a}\# \tag{13}$$

Then, if the equations of motion are the same for those two structures, the same air speed will produce the same aerodynamic forces for each differential length, and the same angles at each equivalent position. That is, a total force proportional to the length with the same angle at the end.

In addition, these relationships result in the reduced velocities of these two trackers being the same:

$$U^* = \frac{U}{b}\frac{2}{\pi}\sqrt{\frac{I}{k}} = \frac{U}{b}\frac{2}{\pi}\sqrt{\frac{I'}{k'}} = U'^*\# \tag{14}$$

To check the validity of this hypothesis, a number of tests have been carried out with experimental models of different aspect ratios. The aspect ratios of the commercial trackers analyzed vary between 5.5 and 45.6, basically increasing with length (see Fig. 15):

The aspect ratios that have been studied are 5, 7.5 and 10 (Id 4, 6 and 7 in Table 2), which are in the range of the minimum ratios found in the market. No larger ratios have been studied so as not to reduce the scale excessively. However, if the hypothesis made is valid, it is obvious that it will also be valid for higher aspect ratios.

Fig. 16 shows the critical reduced velocities of torsional galloping for the three models as a function of the tilt angle. As was the case for the inertia, the variations between them are very small, on average less than 2.3% and between 0.5% and 1% for the angles of the minimum critical velocities.

Using the similarity relations in the stiffness and those of the aspect ratio, it is possible to deduce the transformation relationships between two trackers.

Consider a tracker with dimensions length L_1 and chord b_1, with a torsional stiffness k_1 and an inertia I_1, withstanding a torque T_1 at a wind speed U_1. Then, a tracker of dimensions length L_2 and b_2, with a torsional stiffness k_2, would have the same behavior as the first one if its inertia I_2 is:

$$I_2 = I_1\frac{L_2}{L_1}\left(\frac{b_2}{b_1}\right)^4\# \tag{15}$$

and if the wind speed U_2 is:

$$U_2 = U_1\frac{b_1}{b_2}\sqrt{\frac{k_2}{k_1}\frac{L_1}{L_2}}\# \tag{16}$$

And it would withstand a torsional force T_2:

$$T_2 = T_1\frac{k_2}{k_1}\# \tag{17}$$

If the inertias do not meet the ratio of Eq. (15), it can be said, at least, that they have in common the critical reduced velocity, as shown previously.

5. Stability diagram and optimal design

According to what has been discussed in the previous sections, it can be concluded that the critical reduced velocity of this type of structures depends on the tilt angle but not on the inertia or aspect ratio. And therefore, the values of this reduced velocity can be represented in the following diagram of stability against galloping. Considering the values of the critical reduced velocity of all models tested, their mean value and standard deviation can be seen in Fig. 17, as a function of tilt:

The minimum average critical velocity value is found for negative tilt angles between −20 degrees and −30 degrees and is approximately 0.37. For these angles the variation is very small (around 1%). The other minimum is found for positive values between 15° and 20°, with a value of 0.4 and a variation of 2%. In the zone of horizontal tilts, the average value of the critical reduced velocity increases up to the range of 0.7 to 1,

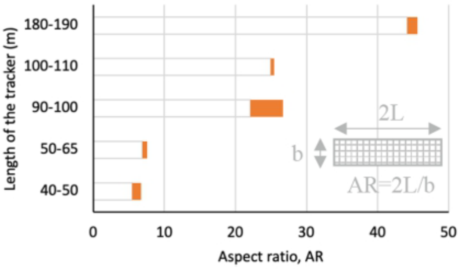

Fig. 15. Histogram of the aspect ratio AR as a function of the length of the tracker.

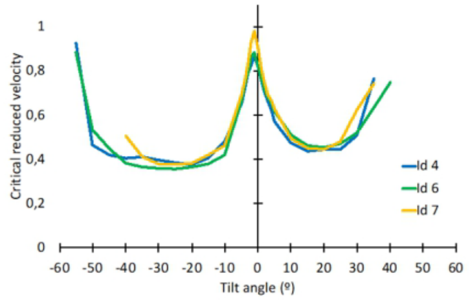

Fig. 16. Critical reduced velocities for models with different aspect ratio.

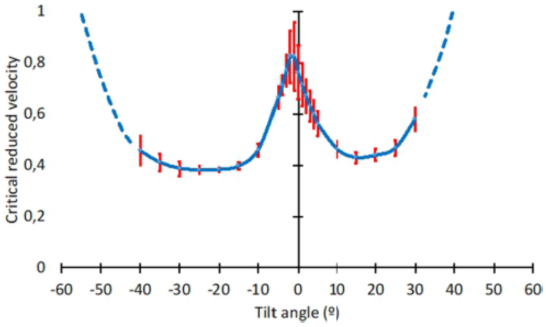

Fig. 17. Stability Diagram against torsional galloping: average value and standard deviation of the critical reduced velocity of the trackers tested.

between −1° and −2°. For large tilts, both positive and negative, the phenomenon disappears. No galloping has been found above 45° or below −55° in any of the models tested. At these extremes the standard deviation also increases, although not as much as in the horizontal angles.

It is believed that the factors that most influence the deviations are the friction of the model shaft with the supports and the gaps in the housings. In the case of angles close to the horizontal, geometric imperfections in the alignment of the leading edge may also be important.

The consistency between the results confirms that the key parameter to avoid torsional galloping is the critical reduced velocity. The relationship with the inertia and the torsional stiffness comes through the natural frequency of the structure.

For the design of a tracker against galloping, the critical velocity can be found with the following equation, taking the minimum values of the critical reduced velocity U^*_{cr} given by Fig. 17:

$$U_{cr} = U^*_{cr}\cdot\frac{b\cdot\pi}{2}\cdot\sqrt{\frac{k}{I}}\# \tag{18}$$

This formulation is specific to the torsional galloping or 1 DOF flutter. Other phenomena, such as VIV, have been found in some tests, although only for specific values of speeds and tilts. The amplitude measured has been an order of magnitude lower and disappears as the velocity increases. Another phenomenon that could appear is the flutter of two degrees of freedom (2DOF), if the solar panels were very flexible in their own plane.

The expression of Eq. (18) can be used to optimize the relationship between the length and chord dimensions of the panel. For instance, when designing a tracker with a certain number of modules ($L\cdot b$ = *constant*), for a fixed weight per square meter, the total inertia of the tracker depends on the width:

$$I = \frac{1}{12}mb^2\# \tag{19}$$

where m is the total mass of the modules.

However, when substituting in the Eq. (18) of the critical velocity, the result is independent of b (and of L):

$$U_{cr} = U^*_{cr}\cdot\frac{\pi}{2}\cdot\sqrt{\frac{12k}{m}}\# \tag{20}$$

Therefore, the only dependence on the inertia is not imposed by the shape but by the mass of the modules: the lower their weight, the higher the galloping critical velocity.

Regarding the torsional stiffness, assuming a thin-walled torque tube, it can be written as:

$$k = \frac{GJ}{L} = \frac{G}{L}\frac{\pi}{32}\left(D_e^4 - D_i^4\right) \approx \frac{G\pi}{8L}D^3e\# \tag{21}$$

where D_e, D_i, D are respectively the outer, inner and middle diameters, and e the thickness of the tube.

The ratio of diameter to thickness is ultimately defined by the buckling limit. According to [30] for long thin-walled cylinders, the criterion is:

$$\tau_{xy} = \frac{E}{3\sqrt{2}\left(1-\upsilon^2\right)^{\frac{3}{4}}}\left(\frac{e}{R}\right)^{\frac{3}{2}}\# \tag{22}$$

From where a limit value for the relationship between thickness and diameter $e/D = C$ can be obtained.

The volume of the torque tube will determine its cost (it will be proportional to the weight). The stiffness can be written as a function of that volume and the value imposed by the critical buckling stress:

$$k \approx \frac{G\cdot Vol^2}{\pi 8C^2L^3}\# \tag{23}$$

Substituting in Eq. (20):

$$U_{cr} = U^*_{cr}\cdot\frac{1}{L^{\frac{3}{2}}}\cdot\frac{Vol}{C}\cdot\sqrt{\frac{3\pi G}{8m}}\# \tag{24}$$

As it can be seen, the velocity of galloping is finally a function of the length, and the chord does not appear directly. According to this relationship, for a given value of the panel surface ($b\cdot L$), the shorter the length of the structure or the larger the width, the greater the wind speed it can withstand without falling into instability.

Despite the previous analysis, it would be necessary to consider that by increasing the tracker's chord, the wind forces per unit length would increase. This would force an increase in the stiffness of the struts in the plane of the panel, as well as the section and foundation of the pillars. Therefore, the optimal length of the tracker would result from a compromise between these factors.

6. Conclusions

In this paper it has been obtained for the first time the Stability Diagram that determines the behavior of a single-axis solar tracker against the phenomenon of torsional galloping. The main contribution of the research is that the galloping critical velocity varies for each tilt, and that the influence of the main structural factors, within the range currently on the market, comes only through the reduced speed.

To this end, the effect of the stiffness in similar models has been examined, and an analytical and experimental study of the influence of the inertia of the modules and the aspect ratio of the panel has been carried out.

To determine the appropriate ranges of these variables, the typical values on existing trackers have been compiled. Currently, these properties are mostly grouped according to the total length of the tracker:

shorter trackers are usually those with lower inertia coefficients and lower aspect ratios, and vice-versa.

Regarding the effect of the inertia, the beginning of the instability has been analyzed from the motion equation and the aeroelastic forces. It has been found that it depends mainly on the sign of the aeroelastic derivative corresponding to the torsional aerodynamic damping. This analysis and the test performed on scale models with different inertia have probed that the critical reduced velocity of torsional galloping does not change with respect to inertia. Likewise, the non-stationary behavior during galloping also seems to be directly related to the reduced velocity.

As for the aspect ratio, it has been assumed that the aerodynamic forces per unit of tracker length are maintained for structures with different aspect ratios, but in different longitudinal coordinates. From this hypothesis, the equations that relate the structural properties between different aspect ratios have been derived analytically. The tests carried out have been focused on the lowest aspect ratio range (the most problematic) and it has been verified that, as with the inertia, the critical reduced velocity of galloping remains constant.

The equations of transformation of structural properties as a function of dimensions and torsional stiffness have also been deduced.

The bulk of the experimental data has been used to plot a Stability Diagram with an average critical velocity line and independent confidence bounds for each tilt angle, as obtained from a standard deviation analysis. This diagram establishes the general criterion of tracker stability against torsional galloping.

Finally, an analysis has been carried out on the optimal design of the tracker. The results show that, for a certain solar capture surface and given dimensions of the torque tube, shorter trackers are more stable with respect to torsional galloping instability, though the wind forces per unit length increase.

CRediT authorship contribution statement

Eva Martínez-García: Software, Methodology, Resources, Data curation, Visualization, Project administration. **Eduardo Blanco-Marigorta:** Conceptualization, Formal analysis. **Jorge Parrondo Gayo:** Validation, Writing - review & editing, Supervision. **Antonio Navarro-Manso:** Investigation, Writing - original draft, Funding acquisition.

Declaration of Competing Interest

The authors declare that they have no known competing financial interests or personal relationships that could have appeared to influence the work reported in this paper.

Acknowledgments

The authors would like to thank Professors and students at Department of Energy for the support provided during the study, as well as TSK for the pictures of the solar plants.

Funding sources

This research has been developed in the framework of the FC-GRUPIN- IDI/2018/000205 project, supported by the Principado de Asturias – Plan de Ciencia, Tecnología e Innovación-, co-financed by FEDER funds.

References

[1] Wesoff E. Solar Trackers in Wind and the Terror of Torsional Gallopoing. PV Magazine USA; 2020. January 17th. https://pv-magazine-usa.com/2020/01/17/dan-shugar-nextracker-ceo-on-solar-trackers-in-wind-and-the-terror-of-torsional-galloping/.

[2] Lazard. Lazard's Levelized Cost of Energy Analysis – Version 12.0. Lazard, New York, USA; 2018. https://www.lazard.com/media/450784/lazards-levelized-cost-of-energy-version-120-vfinal.pdf.

[3] Energy Information Administration. Levelized Costs and Levelized Avoided Cost of New generation Resources in the Annual Energy Outlook. U.S. Energy International Agency; 2021. https://www.eia.gov/outlooks/aeo/pdf/electricity_generation.pdf.

[4] Talavera DL, Muñoz-Cerón E, Ferrer-Rodríguez JP, Pérez-Higueras PJ. Assessment of cost-competitiveness and profitability of fixed and tracking photovoltaic systems: the case of five specific sites. Renew Energy 2019;134:902–13. https://doi.org/10.1016/j.renene.2018.11.091.

[5] Masson G, Kaizuka I. Trends 2019 in Photovoltaic Applications. (IEA) International Energy Agency; 2019. https://iea-pvps.org/wp-content/uploads/2020/02/5319-iea-pvps-report-2019-08-lr.pdf.

[6] Bahrami A, Onyeka Okoye C, Atikol U. Technical and economic assessment of fixed, single and dual-axis tracking PV panels in low latitude countries. Renew Energy 2017;113:563–79. https://doi.org/10.1016/j.renene.2017.05.095.

[7] Koussa M, Cheknane A, Hadji S, Haddadi M, Noureddine S. Measured and modelled improvement in solar energy yield from flat plate photovoltaic systems utilizing different tracking systems and under a range of environmental conditions. Appl Energy 2011;88:1756–71. https://doi.org/10.1016/j.apenergy.2010.12.002.

[8] Lave M, Kleissl J. Optimum fixed orientations and benefits of tracking for capturing solar radiation in the continental. Renew Energy 2011;36:1145–52. https://doi.org/10.1016/j.renene.2010.07.032.

[9] Galuppi L, Royer-Carfagni G. Enhanced Effective Thickness for laminated glass beams and plates under torsion. Eng Struct 2020;206:110077. https://doi.org/10.1016/j.engstruct.2019.110077.

[10] Pickerel K. How the Solar Industry is Responding to the Increasing Intensity of Natural Disasters. Solar Power World (SPW) 2018, January 29th. https://www.solarpowerworldonline.com/2018/01/solar-industry-responding-increasing-intensity-natural-disasters/.

[11] Rohr C, Bourke PA, Banks D. Torsional instability of single-axis solar tracking systems. In: Proc. 14th Int. Conf. Wind. Eng. 2015, Porto Alegre Brazil, June.

[12] Willuhn M. Tracking in the wind. PV Magazine Australia 2019, September 7th. https://www.pv-magazine-australia.com/2019/09/07/long-read-pt-1-tracking-in-the-wind/.

[13] Davenport AG. The buffeting of large superficial structures by atmospheric Turbulence. Ann N Y Acad Sci 1964;116:135–59. https://doi.org/10.1111/j.1749-6632.1964.tb33943.x.

[14] Jia J. Wind and structural modelling for an accurate fatigue life assessment of tubular structures. Eng Struct 2011;33(2):477–91. https://doi.org/10.1016/j.engstruct.2010.11.004.

[15] Pfahl A, Buselmeier M, Zaschke M. Wind loads on heliostats and photovoltaic trackers of various aspect ratios. Sol Energy 2011;85(9):2185–201. https://doi.org/10.1016/j.solener.2011.06.006.

[16] Stathopoulos T, Zisis I, Xypnitou E. Local and overall wind pressure and force coefficients for solar panels. J Wind Eng Ind Aerodyn 2014;125:195–206. https://doi.org/10.1016/j.jweia.2013.12.007.

[17] Miller RD, Zimmerman DK. Wind Loads on Flat Plate Photovoltaic Array Fields. Seattle, Washington: Boeing Engineering and Construction Company; 1981.

[18] Kopp GA, Farquhar S, Morrison MJ. Aerodynamic mechanisms for wind loads on tilted, roof-mounted solar arrays. J Wind Eng Ind Aerodyn 2012;111:40–52. https://doi.org/10.1016/j.jweia.2012.08.004.

[19] Strobel K, Banks D. Effects of vortex shedding in arrays of long inclined flat plates and ramifications for ground-mounted photovoltaic arrays. J Wind Eng Ind Aerodyn 2014;133:146–9. https://doi.org/10.1016/j.jweia.2014.06.013.

[20] Simiu E. Scanlan RH Wind Effects on Structures: Fundamentals and applications to design. 3th ed. New York: John Wiley & Sons, Ltd.; 1996.

[21] Blevins RD. Flow-Induced Vibration. 2nd ed. New York: Van Nostrand Reinhold Co.; 1990.

[22] Seo D, Caracoglia L. Estimation of torsional-flutter probability in flexible bridges considering randomness in flutter derivatives. Eng Struct 2011;33(8):2284–96. https://doi.org/10.1016/j.engstruct.2011.03.016.

[23] Taylor ZJ, Browne MTL. Hybrid pressure integration and buffeting analysis for multi-row wind loading in an array of single-axis trackers. J Wind Eng Ind Aerodyn 2020;197:104056. https://doi.org/10.1016/j.jweia.2019.104056.

[24] Martínez-García E, Blanco-Marigorta E, Parrondo J, Navarro-Manso A. Experimental determination of the resistance of a single-axis solar tracker to torsional galloping. Struct Eng Mech 2021;78:519–28. https://doi.org/10.12989/sem.2021.78.5.519.

[25] Scanlan RH, Tomko JJ. Airfoil and bridge deck flutter derivatives. J Eng Mech Div 1971;ASCE 97:1717–37.

[26] Wardlaw RL. Flutter and Torsional Instability. In: Sockel H, editor. Wind-Excited Vibrations of Structures. Vienna: Springer; 1994. p. 335. https://doi.org/10.1007/978-3-7091-2708-7_6.

[27] Rodríguez M, Fernández JM, Galdo M, Blanco-Marigorta E, Santolaria C. Novel design and experimental validation of a contraction nozzle for aerodynamic measurements in a subsonic wind tunnel. J Wind Eng Ind Aerodyn 2013;118(3):5–43. https://doi.org/10.1016/j.jweia.2013.04.008.

[28] Fan X, Wang Z, Chen X, Wang Y, Tan W. Experimental investigation on flow-induced vibration of flexible multi cylinders in atmospheric boundary layer. Int J Mech Sci 2020;183:105815. https://doi.org/10.1016/j.ijmecsci.2020.105815.

[29] Rao SS. Vibration of Continuous Systems. New York: Wiley; 2007.

[30] Timoshenko S, Gere JM. Theory of elastic stability. New York: Mc-Graw Hill; 1963.

3.3 Métricas del artículo

ARTÍCULO. 2	
Revista	Engineering Structures
Título	Influence of inertia and aspect ratio on the torsional galloping of single-axis solar trackers
Cuartil	Q1
Factor de impacto (JCR)	5.58
Citescore (Scopus)	7.6
N° citas [junio 2021-octubre 2024]] (Web of Science)	25

Capítulo 4. Referencia experimental para la construcción de un modelo canónico 3D, para ensayar las inestabilidades aeroelásticas torsionales de un seguidor solar monoeje en túnel de viento.

4.1. Descripción del artículo

Este trabajo propone una metodología innovadora y referente para estudiar las inestabilidades aeroelásticas torsionales en seguidores solares de un solo eje, utilizando pruebas en túneles de viento que permiten evaluar con precisión las condiciones críticas bajo las cuales se desarrollan estas inestabilidades. A través de la construcción de un modelo 3D completamente aeroelástico, que replica con exactitud las propiedades torsionales y de flexión de los seguidores solares, el estudio ofrece una solución práctica para analizar cómo responden estas estructuras a diversas condiciones de viento. El modelo fue probado en dos túneles de viento distintos (Universidad Politécnica de Madrid y Universidad de Oviedo), lo que permitió validar los resultados y asegurar su reproducibilidad. Los principales hallazgos incluyen la identificación de la velocidad crítica necesaria para que se desarrolle la inestabilidad torsional, la cual está altamente influenciada por el ángulo de inclinación de los paneles. Se encontró que este fenómeno es asimétrico, con una mayor vulnerabilidad en inclinaciones entre +35° y -45°. A partir de estos datos, se construyó un diagrama de estabilidad que visualiza las zonas de riesgo de inestabilidad según la velocidad y el ángulo de inclinación, proporcionando una herramienta esencial para diseñadores e ingenieros que buscan optimizar la seguridad y eficiencia de los seguidores solares. Además, se demostró que los modelos a escala, si cumplen con las condiciones de similitud aerodinámica y estructural, pueden reproducir con fidelidad los fenómenos aeroelásticos observados en la realidad. Este enfoque metodológico llena un vacío en los estándares actuales, que carecen de criterios específicos para evaluar inestabilidades aeroelásticas en seguidores solares, y establece una referencia valiosa para futuras investigaciones, optimización de diseños y simulaciones CFD en el campo de la energía solar.

4.2. Publicación en revista revisada por pares

Referencia experimental para la construcción de un modelo canónico 3D, para ensayar las inestabilidades aeroelásticas torsionales de un seguidor solar monoeje en túnel de viento.

Journal of Wind Engineering & Industrial Aerodynamics 253 (2024) 105838

Contents lists available at ScienceDirect

Journal of Wind Engineering & Industrial Aerodynamics

journal homepage: www.elsevier.com/locate/jweia

Experimental Benchmark for the 3D wind tunnel testing of torsional aeroelastic instabilities in single-axis solar trackers

Carlos Rodríguez-Casado [a], Eva Martínez-García [a], Raúl Manzanares-Bercial [b], José Luis Ruiz-Moral [b], Eduardo Blanco-Marigorta [a], Antonio Navarro-Manso [a,*]

[a] Energy Department, University of Oviedo, Gijón, Spain
[b] Microgravity University Institute "Ignacio Da Riva" (IDR/UPM), Polytechnic University of Madrid, Madrid, Spain

ARTICLE INFO

Keywords:
Torsional instability
Single-axis solar tracker
Wind tunnel test
Aeroelastic model
Tilt angle
Stability diagram

ABSTRACT

Wind-excited torsional oscillation of photovoltaic single-axis solar trackers constitutes a class of complex fluid-structure interaction phenomena, involving torsional galloping, torsional divergence, 1DOF flutter, VIV and buffeting. The highest potential for structural damage corresponds to torsional aero-elastic instability, which develops when wind speed exceeds a critical value that, for a given tracker, depends on tilt. Current engineering standards do not offer reliable criteria to yield safe operation conditions, therefore each case requires specific wind tunnel testing. Since data reported in the literature are scarce and scattered, from both industry and academia there is a growing need to define a Benchmark as a reference to compare results and validate methodologies of different studies. This paper proposes a tracker model with 3D aeroelastic characteristics, both torsion and bending, appropriate for wind tunnel testing, including geometry, mounting details, experimental methodology and critical velocity criterion. Tracker units built according to this model were tested in two different wind tunnels (at Polytechnic University of Madrid and University of Oviedo), and the respective measurements show good agreement. The reported results include stability maps with comparison to literature data, an evaluation of the phenomena identified, and the effects of the tracker relative position in a row.

Nomenclature		m	Mass variable
List of symbols		Re	Reynolds number
AR	Aspect ratio, L/b	RMS	Root mean square, typical value of the amplitude
b	Panel chord	St	Strouhal number
C_{IR}	Rotational inertia coefficient	T	Torque magnitude
C_{KF}	Flexural stiffness coefficient	C_T	Torque coefficient
C_{KT}	Torsional stiffness coefficient	t	Time variable
C_M	Mass coefficient	U	Wind speed
C_T	Torque coefficient	U_{cr}	Critical velocity for torsional instability
D	Diameter of the torque-tube (outer)	U_{crmin}	Minimum critical velocity
E	Elasticity or Young's module	U^*	Reduced velocity
e	Thickness of the torque-tube	U^*_{cr}	Reduced critical velocity
f	Frequency variable	a_0	Initial tilt angle
f_T	Torsion natural frequency of the solar tracker, typically first mode	a	Angle displacement variable
G	Shear module	Δa	Angle increment
H	Height of the solar tracker, from the center of the torque tube	δ	Logarithmic decrement
h	Clearance, distance between the panel (mid plane) and the center of the torque tube	λ	Geometrical scale
I	Area moment of inertia of the panels	ρ	Air density
I_R	Rotational inertia: mass moment of inertia respect to the axis	μ	Air viscosity
J	Polar moment of inertia	ζ	Damping ratio
K_T	Torsional stiffness of the torque tube	**Subscripts**	
L	Structure characteristic length, one wing, half the whole solar tracker	m	Scale model
M	Mass of the solar tracker	p	Prototype
m	Mass variable		

(*continued on next column*)

(*continued*)

1. Introduction

A single-axis solar tracker is a structure made up of several photovoltaic panels mounted in-line on a horizontal shaft (torque tube) that is driven by a motor. The motor rotates the tracker so that the tilt angle of

---

* Corresponding author.
E-mail address: navarroantonio@uniovi.es (A. Navarro-Manso).

https://doi.org/10.1016/j.jweia.2024.105838
Received 5 February 2024; Received in revised form 18 July 2024; Accepted 21 July 2024

the panels can be progressively varied from east to west orientation every day, in order to maximize the amount of solar energy captured by the photovoltaic cells. Structurally, this system has one degree of freedom (1DOF) that corresponds to torsional rotation, because the supports distributed along the torque tube preclude any significant movement in the radial direction. In these systems, the first mode of vibration is often a low frequency helical torsion (of the order of 1 Hz), which does not generate any deflection in the motor shaft but causes opposite rotation at both ends (Rohr et al., 2015). The need to reduce costs in such a competitive industry sector has led to narrower torque tube designs. The latter, combined with large flat plates that can be exposed to wind loading, often results in solar trackers that exhibit aerodynamic instability (Martínez-García et al., 2021b; Taylor et al., 2024). In fact, this type of structures can be subject to different types of aeroelastic phenomena, including torsional galloping or single degree of freedom flutter, vortex induced vibration, and buffeting. Indeed, aeroelastic phenomena have been studied for decades on various types of flexible structures (Scanlan and Sabzevarit, 1969), but, in the case of single axis solar trackers (SAT), their damage potential has only been reported recently (Valentín et al., 2022). Not all the causes and effects of these phenomena are fully understood, and it is also necessary to study how they can interact (Enshaei et al., 2023). Understanding the phenomena involved is crucial to improve the aeroelastic performance of the SATs through more efficient designs (Gross et al., 2020), as well as to avoid possible failures by addressing non-specific standards in the planning stage (Cheruku et al., 2020). Therefore, many related projects are currently underway worldwide (Bruner et al., 2022).

Throughout the last decades, solar energy harvesting has been based on different types of structures with different geometries, including heliostats, solar trackers, collectors, cable suspended panels, etc. The importance of properly considering wind loads and aeroelastic effects was already pointed out by Roschke (1984), in an early report on solar concentrators. In the case of heliostats, recent research focused on the peak wind loads and the use of passive elements, such as fences and spoilers, to mitigate that loading (Pfahl, 2018; Pfahl et al., 2011). Photovoltaic modules supported by suspension cables can be especially prone to vibrate under wind load and stability conditions were studied by He et al. (2020) and under different turbulence of the approaching flow (Kim et al., 2018). Besides, Chen et al. (2023) presented a comprehensive review focused on the wind induced response of flexible photovoltaic systems. However, the results and conclusions drawn from these studies cannot be directly applied to SATs because of the peculiarity of their geometry and structural design, and so specific research needs to be carried out on SATs.

Over the last decade, several techniques have been developed to study these flexible structures, both in single-row and multi-row configurations. As the simplest procedure, static wind tunnel testing has been traditionally used in the industry to help design the SAT structures to withstand wind static loading, but this is not useful to assess on aeroelastic loading and response. Instead of wind tunnel data, McBean (1985) used a simplified wind pressure distribution to yield a conservative design for the structures, except in the case of collectors subject to severe turbulence effects near the edge of the field. They also stated that aeroelastic behavior should be assessed in wind tunnels to evaluate the potential for unacceptable vibrations due to vortex shedding or flutter. More recently, Strobel and Banks (2014) shown that the conventional '1 Hz threshold' standard is not appropriate for ground-mounted photovoltaic panel arrays in multi-row configuration, because such small structures can exhibit both self-excitation and buffeting from upwind panels at frequencies well above that value during both serviceability and design wind events. Later, Cain et al. (2015) demonstrated that the usual codes did not account properly for buffeting and vortex shedding excitation, and so they attempted to determine limiting wind velocities for safe operation by combining several dynamic variables of both wind and structure, including the gust factor, the dynamic amplification factor (DAF), the reduced velocity and the structural damping. Since then, several studies on rigid scale models have considered tests of multi-row configurations in Atmospheric Boundary Layer (ABL) wind tunnels, in order to include unsteady wind excitation; in general, the results show that the aerodynamic forces and torque depend on row spacing and are higher at the perimeter region, so that the effect of shielding needs to be considered. However, rather than tackling the actual aeroelastic phenomena, these studies were still primarily based on the DAF concept (Kray and Markus, 2019) and the cover ratios, the panel aspect ratio, and force and torque coefficients for static structures (Yağci et al., 2018). With this same type of assumptions, Wittwer et al. (2022) combined experimental studies on rigid models with FEM simulations in order to determine worst-case scenarios for both single and multi-row configurations, pointing out that the standards cannot be applied to all the individual situations. More recent studies focused on the purlins of the underlying structure, which were identified to play a role in the dynamic response especially when the tilt angles are small (Chowdhury et al., 2022), or in the interference effects between SAT rows (Ma et al., 2023).

Dynamic tests have also been performed to characterize the aeroelastic behavior of SATs and the conditions leading to fluid-structure instability. For this kind of tests, the extrapolation of results is subject to verify the usual similarity conditions for unsteady viscous flow, like Strouhal and Reynolds numbers, but also for the dynamic parameters of the structure like the frequency and damping ratios (American Society of Civil Engineers (American Society of Civil Engineers, 2021). A basic goal of these studies is to determine the threshold or critical wind speed for instability onset, which is equivalent to the critical speed for flutter of a 1DOF system (also referred to as galloping in the literature).

A usual procedure is to implement dynamic sectional tests (2D) in wind tunnel to study the variation of the angle of attack of the tracker when subject to cross flow (Franchini et al., 2019). Initially, these studies were based on classical tests on rectangular cylinders undergoing vortex induced vibrations (VIV) or galloping (Mannini et al., 2014), thus considering St and Sc as non-dimensional parameters to model the phenomena. Pigolotti et al. (2017) shown their influence on the critical velocity for instability and also on the response in the post-critical regime, by determining the net damping ratio of the flow-structure coupled system. J. Quintela et al. (2020, 2020b), a conducted sectional experimental wind tunnel tests and computer-aided numerical integration in order to estimate the so-called flutter derivatives, which are related to the unsteady force and torque coefficients, to explain the development of vortex shedding, torsional divergence and flutter of the SATs. They also explored the use of mechanical dampers to control the development of flutter instability (Quintela et al., 2020, 2020b). More recently, Frontini et al. (2022) and Martínez-García et al. (2021b) presented stability diagrams for galloping or 1 DOF flutter, which show the dependence of the critical velocity on the tilt angle of the panels. The influence of the turbulence intensity has been also analyzed on a sectional model (Ma et al., 2023) showing two different behaviors for large torsional vibrations at various tilt angles: strong and weak coupling. The stability conditions for torsional instability depending on the height of the SAT above the ground has been recently stated by Cárdenas-Rondón et al. (2023).

The first stability diagram for a wide range of tracker characteristics was however published by Martínez-García et al. (2021b), using another approach, which is to consider a complete 3D model of a tracker under strict aeroelastic similarity conditions (Martínez-García et al., 2021a). Enshaei et al. (2023) published a recent survey on the methods used to study torsional instability and the results on the excitation mechanisms. Taylor et al. (2024) tested a 3D aeroelastic model replicating the dimensions and torsional stiffness of certain tracker; and discussed the results in comparison with other methodologies and studies. All these studies are focused on stand-alone or single row configuration.

This can also be extended to multi-row configurations to study the behavior of internal rows and possible row interactions and to analyze the effect of wind direction. The same model than Ma et al. (2023) was used for the study of multi-row configuration (Zhang et al., 2023) finding that the interference between the rows is weak when the trackers are nearly horizontal, and a flutter instability is developed for every row; however, for larger tilts the interference increases, and the vibration is closer to vortex induced vibration type. Interference effects among solar panel units can cause instability due to the gap between the rows: Kim et al. (2018) performed a wind tunnel test of 12 solar panels suspended by cables, oriented horizontally, and varying both the turbulence and wind direction. Using the same scale model, Kim et al. (2020) found that certain shapes of the panels may mitigate or even eliminate the vibration.

Given the complexity of performing accurate measurements on fully aeroelastic models, Taylor and Browne (2020) proposed a hybrid approach based on wind tunnel testing of sectional rigid models, to measure pressure distributions, combined with phase data relative to the tracker motion obtained from numerical calculation (FEM and CFD). With this procedure, it is possible to obtain the aerodynamic coefficients and the aeroelastic derivatives of the tracker, so that the complete aeroelastic behavior can be reproduced and considered for the structural design of the trackers.

Computational Fluid Dynamics (CFD) methodologies have been used in parallel with the experimental research, often in a complementary way as in some of the aforementioned references. In fact, despite the huge advances in the last decades in both computational capacity and numerical analysis tools, the experimental validation of predictions remains unquestionably necessary. Unsteady flow models ranging from the basic URANS to the more complete LES formulations can be used to describe the flows of interest in aeroelastic problems, like the highly unsteady flows involving with 3D wakes and vortical structures that fluctuate along with the tracker motion (Breuer and Jovicic, 2001). However, the associated computational costs of 3D models are still high, and 2D models of flat plates have been frequently considered (Barrero-Gil and Sanz-Andrés, 2009) to simulate both linear and non-linear aeroelastic instabilities. Young et al. (2020) analyzed the stowed position of a SAT and found that galloping instability is related to cyclic vortex shedding at the leeward edge and the elastic properties of the torque tube. Numerical simulations of hydraulic dampers have also been performed (Watwe and Kartik, 2021).

With a different perspective, some studies have used measurement data from full-scale plants under real wind conditions to check the predictions of theoretical or numerical models, and even to check the extrapolation of data from wind tunnels, since the latter were obtained in a controlled laboratory environment. That is the case of Dana and Young (2020), who carried out load and acceleration measurements on SAT prototypes located in a real photovoltaic plant, with the aim of contrasting the stability characteristics predicted from 3D simulations and obtain a stability map. After testing panels at different tilt angles and a variety of wind conditions, they concluded that the panels are more stable when oriented at a negative angle (i.e., with the leading edge closer to the ground), due to ground blocking effects. Besides, fiber optic sensors have been used to measure stress and temperature distribution throughout a SAT structure (Mariñelarena et al., 2019), and also to monitor the structural torsion under field conditions (Leandro et al., 2020). Tests have also been carried out in real installations with other types of solar collectors that, like SATs, also involve photovoltaic panels under wind loading. Bhaduri and Murphy (1985), published an extensive report on wind velocity profiles on photovoltaic arrays and the resulting force coefficients on the panels as a function of aspect ratio and tilt angle, including a comparison with the static approach of the ASCE code and validation aspects with large-scale experiments. They also studied the spectra of turbulent velocity fluctuations, addressing the importance of topographical aspects. More recently, Adeleke (2016) combined on-site strain gauge measurements with a FEM model of a two-axis solar tracker, to predict displacements at higher wind speeds. Kaabia et al. (2017) conducted full scale tests on concentration photovoltaic (CPV) panels under moderate wind speed conditions (accordingly, the forces obtained cannot be extrapolated to extreme wind events).

It is also feasible to pursue theoretical investigations or other types of tests that analyze the same phenomenon in a different way; and to explore other phenomena and their possible interactions. Among the former, the influence of the mechanical properties of a sign panel on the forces induced by the motion is developed (Barrero-Gil and Sanz-Andrés, 2009). And regarding the latter, Armandei and Fernandes (2014), observed that a rectangular flat plate with 1DOF (torsional) becomes unstable when the current speed exceeds a critical value; experiments were carried out in a water channel at approximately $\mathrm{Re} = 1{\cdot}10^5$, the moment on the plate was extracted from the flutter derivatives (free vibration experiments) and the Hopf bifurcation was analyzed. There are several studies of the oscillating fluid phenomenon through the St number, although most of them are made on static bodies. For example, explanations of shear layer separation and reattachment are well known on rectangular cylinders (Knisely, 1990) and flat plates (Chen and Fang, 1996), depending on the angle of attack. Rostami et al. (2019) performed a test in a water channel and offered an interesting contribution on how the vortex force could trigger galloping in a flat and flapped plate. Marra et a. (2015), mentioned the interest of studying the vortex induced vibration of rectangular cylinders and the need for verification for other structures where damping is uncertain, or dampers need to be designed. And the interaction between some aeroelastic phenomena has been reported: research on spring-mounted slender rectangular cylinders concluded that structures with ordinary mass damping properties can exhibit sustained vibrations in flow velocity ranges where no excitation is predicted by classical theories of vortex-induced vibration and galloping (Mannini et al., 2016).

For the correct execution of an aeroelastic wind tunnel test, it is necessary to establish geometric, kinematic and dynamic similarity (American Society of Civil Engineers, 2021) between the prototype of a flexible structure and its scale model, matching the significant dimensionless parameters.

Indeed, there has already been a significant research effort devoted to the aeroelastic behavior of SATs and other related structures under wind loading. However, the range of possible geometrical and physical configurations of engineering interest is large (Roedel and Upfill-Brown, 2018), and, besides, the associated flow-structure interaction phenomena are complex, up to the point of having different possible excitation mechanisms leading to instability that may coexist and affect each other. Taylor et al. (2024) defined the primary aeroelastic mechanisms involved in the torsional instability and compared the results by several of the methods previously mentioned. Furthermore, the variety of flow-structure phenomena can be expected to increase, because the current exponential deployment of PV plants worldwide, with progressively leaner structures to reduce manufacturing costs (Roedel, 2021; Roedel and Butcher, 2021), is likely to increase the rate of high vibration events and failure cases induced by wind dynamic load. In consequence, the data available from tests and simulations happen to be both sparse and scattered, and our current knowledge of the fundamental phenomena involving aeroelasticity of SATs can still be considered limited (Ricci, 2020). In particular, there is a growing need to establish a set of test criteria and conditions (Taylor et al., 2024) that are suitable for investigating the aeroelastic response of a reference SAT, so that measurement data and simulation predictions can be properly reproduced and contrasted elsewhere (Browne et al., 2020).

The aim of this article is to define a Benchmark that, in compliance with the similarity laws, may be used in the research and design of solar tracking systems. The Benchmark model, involving full 3D aeroelastic features, consists of one single row tracker and it has been defined in detail and tested in two different wind tunnels (Polytechnic University of Madrid and University of Oviedo) under controlled conditions, obtaining accurate information about its aerodynamic behavior. In particular, a procedure is proposed to determine the critical velocities of the torsional aeroelastic instability. This Benchmark is intended to become a reference for wind tunnel testing and CFD modelling, so that tests under controlled conditions can be reproduced in other laboratories and even subjected to peer review. It will also provide reliability to the results obtained at a given facility for other tracker designs or configurations. All this will ultimately contribute to optimizing the design of the trackers and improving their dynamic performance and durability, mending the current gap in the standards applicable to SAT structures.

2. Definition and design of the Benchmark model

2.1. Prototype

The prototype used as a reference for this article is a basic Single-Axis Solar Tracker (see Fig. 1). It features a central pillar with the motor, and two lateral wings composed of a long shaft (torque tube) onto which the panels are mounted. The tube is supported by several pillars along its length. The central motor regulates the orientation throughout the day and structurally acts as a fixed support. Any vertical or horizontal movement is prevented by the support pillars distributed along the span of the tube, allowing only rotational motion. Therefore, the tube behaves like a torsion beam, with a fixed end on one side and a free end on the other.

As mentioned, such Solar Trackers are prone to torsional aeroelastic instability. When the wind speed reaches a certain value it causes oscillations in the angular position, increasing in magnitude closer to the free end. These oscillations occur at frequencies near the natural frequencies of the structure and increase rapidly in amplitude with wind speed. Due to their magnitude, these oscillations may result in structural collapse.

The speed at which the instability starts depends on the geometric and structural characteristics, and especially the natural frequencies. In these trackers, the first vibration mode corresponds to the torsion of the torque tube. This mode has the lowest natural frequency, the largest deformations, and is why this instability is commonly referred to as torsional. If the transverse stiffness is sufficiently low, flexural vibrations

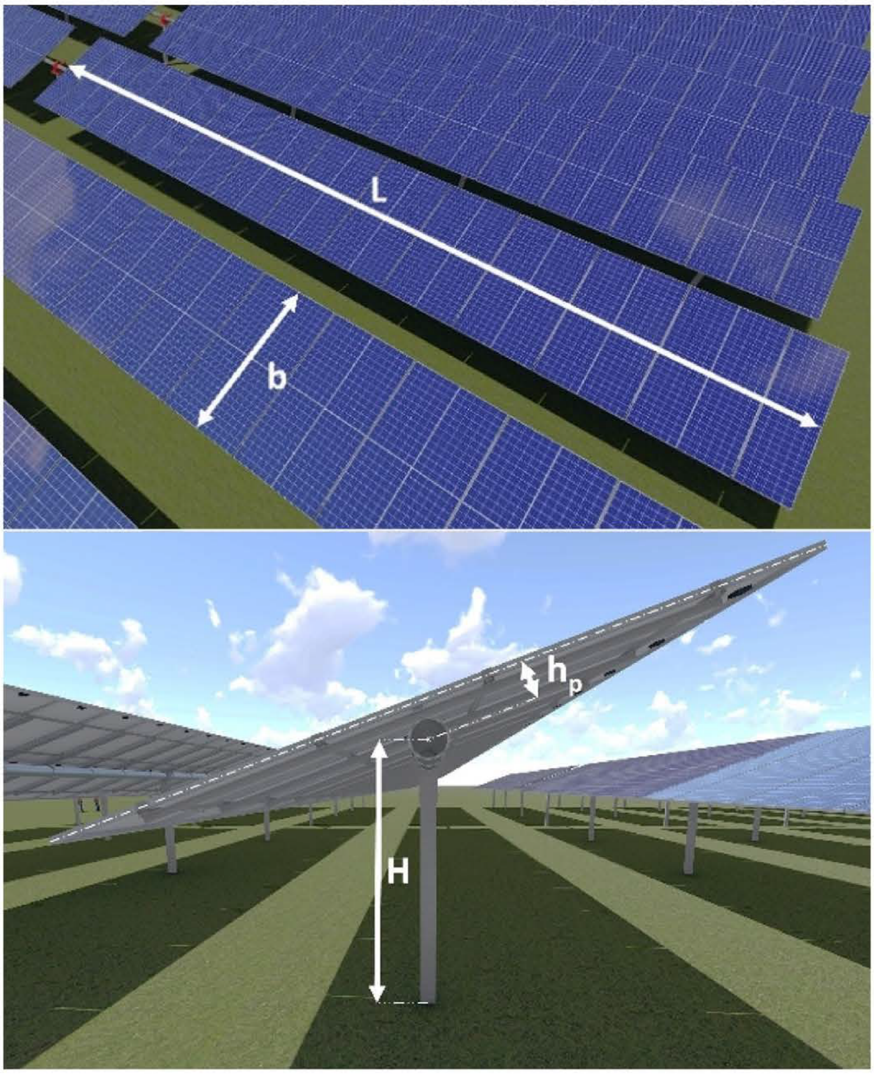

Fig. 1. Structural sketch of the tracker.

corresponding to the bending of the panels might also appear, although the higher vibration modes are generally not noticeable.

The prototype has been selected with two independent vertical rows of panels (2P), each tracker consisting of a total of 96 panels (48 per wing). The panels have been taken to be 2.4 m long and 1.2 m wide. The total length of the tracker is 2 L_p = 57.6 m (L_p = 28.8 m), and the tracker's chord is $b_p = 4.8$ m. The aspect ratio ($AR = 2L/b$) is 12, which is representative of the systems with 2 modules-in-portrait. The systems with one module-in-portrait usually have a larger aspect ratio. The torque tube is steel with a circular section of diameter $D_p = 200$ mm and thickness e_p = 4 mm. It is supported by 6 pillars (3 per wing). The distance from the tube axis to the ground is H_p = 3 m, and the distance to the panels is $h_p = 0.24$ m. In the variables, subscripts p and m are used to refer to the prototype and model respectively.

The panels are attached to the torque tube with rectangular steel purlins, measuring 80 × 40 mm and 2 mm thick. The purlins are as long as the tracker's width, with 49 purlins per wing. The mass of the panels is 15 kg/m^2, with an additional 25% weight considered for purlins and fastenings.

Regarding the natural frequencies of the prototype, the main one is that of the torsional mode, as mentioned above. This torsional movement, and the corresponding frequency, are controlled by the torsional stiffness and the rotational inertia. The torsional stiffness is essentially that of the torque tube, as the contribution of the panels is negligible. Conversely, the inertia of this movement is mainly due to the mass of the panels and purlins. The torsional stiffness, for a fixed-free tube with a moment at the free end, can be calculated as:

$$K_{Tp} = \frac{GJ}{L} \tag{1}$$

Where G is the Shear Modulus, which has been taken as 80.8 GPa for steel, and J is the Polar Moment of Inertia of the torque tube. The prototype's torsional stiffness value is $K_{Tp} = 6.64{\cdot}10^4$ N m.

The rotational inertia of the tracker (Mass Moment of Inertia with respect to the torsional axis) considering panels, purlins, and tube, is $I_{Rp} = 5.14{\cdot}10^3$ kg m^2.

The prototype's natural torsional frequency can be calculated using the following expression (Rao S.S., 2019):

$$f_{Tp} = \frac{1}{4}\sqrt{\frac{GJ}{I_{Rp}L}} = \frac{1}{4}\sqrt{\frac{K_{Tp}}{I_{Rp}}} \tag{2}$$

The value is $f_{Tp} = 0.90$ Hz.

Without conducting a finite element study, it is not easy to determine the sequence and frequencies of higher vibration modes. Nevertheless, since the bending movement of the panels overlaps with the torsional movement, the panels flexural vibration has also been considered, taking into account the corresponding mass and stiffness. The total mass of a wing is $M_p = 2592$ kg. The flexural stiffness is a function of EI, where E is the Young's modulus, and I is the second moment of area. It has been calculated that the composite value (steel and glass) is approximately $(EI)_p = 2.3{\cdot}10^5$ N m^2.

No other vibration modes have been considered for this prototype tracker, but the current trend of using shorter purlins with smaller sections and panels with more slender frames, might lead to the emergence of plate vibration frequencies. Similarly, depending on their height and section, the pillars could also generate modes interfering with the phenomenon.

2.2. Similarity

Regarding the torsional aeroelastic instability of single-axis solar trackers, the variables involved include the characteristic length (L), typically the span or chord, as well as those corresponding to the fluid: velocity (U), density (ρ), and viscosity (μ). Then there are structural effects to consider, such as torsional stiffness (K_T) and rotational inertia with respect to the tube axis (I_R) in the case of torsion, and mass (m) and flexural stiffness (EI) in the case of bending. Additionally, structural damping (ζ) should be taken into account. The corresponding variable for the results would be the Torque (T) or, if a vibration is involved, the amplitude of the moment and the frequency (f_M) of the resulting aeroelastic excitation. Gravity has no influence because the pillars block the vertical movements.

By performing the dimensional analysis, the dimensionless numbers are obtained. The Reynolds number from the fluid variables:

$$Re = \frac{\rho U L}{\mu} \tag{3}$$

The structural coefficients from the corresponding structural variables (American Society of Civil Engineers, 2021):

Torsional stiffness coefficient:

$$C_{KT} = \frac{GJ}{\rho U^2 L^4} = \frac{K_T}{\rho U^2 L^3} \tag{4}$$

Rotational inertia coefficient:

$$C_{IR} = \frac{I_R}{\rho L^5} \tag{5}$$

Flexural stiffness coefficient:

$$C_{KF} = \frac{EI}{\rho U^2 L^4} \tag{6}$$

Mass coefficient:

$$C_M = \frac{M}{\rho L^3} \tag{7}$$

And damping coefficient: ζ which is inherently dimensionless.

Regarding the results, the Torque coefficient (Euler number), typically defined in terms of the area and chord:

$$C_T = \frac{T}{\frac{1}{2}\rho U^2 b^2 L} \tag{8}$$

and the Strouhal number:

$$St = \frac{fL}{U} \tag{9}$$

From the similarity point of view, if a prototype and a geometrically similar model have the same structural coefficients, for the same flow coefficient values, the aerodynamic phenomenon is similar; that is, the model and prototype will have the same result coefficients.

Although not specifically considered as a variable, in trackers, angles are important as they define the position and torsional movement. It is noteworthy that unlike other variables requiring similarity transformations, the angle is inherently dimensionless. Under similarity conditions, they are the same in model and prototype.

Regarding flow variables, as a rule, scale model tests require the use of the same Reynolds number. This could be problematic, especially when the scale ratio is large. However, for bluff bodies, aerodynamic phenomena are relatively insensitive to Reynolds number when it is sufficiently high. Therefore, this condition can usually be relaxed, and other dimensionless numbers can be prioritized. Nevertheless, the relaxation is contingent on the extent to which free-stream turbulence (and the associated scales) exert a more pronounced impact. It is also important to highlight that this underscores the importance of conducting comprehensive full-scale measurements to substantiate the findings obtained from the wind tunnel experiments.

With respect to gravity, it is true that the pillars block the vertical movement but, due to the offset of the mass from the torque tube, at high tilt angles there is a rotational deflection. In typical systems such as the one under consideration, this deflection is only 1 or 2° and can be neglected. In more slender systems it may be necessary to take this effect into account.

When gravitational forces are significant, another dimensionless number to comply with is the Froude number. This number usually determines the velocity ratio between model and prototype. When these forces are not significant, the velocity ratio can be defined based on model stiffness. Inertia and mass ratios are fixed by their dimensionless numbers, but the stiffness coefficient also includes the velocity, allowing one degree of freedom. That is, if the model is built with a certain stiffness, the test velocity is determined by it.

Typically, the velocity is made non-dimensional, with the chord and the combination of torsional stiffness and rotational inertia (or bending stiffness and mass), which determine the natural frequency of vibration. The dimensionless form of the velocity is known as the reduced velocity which, in this case, utilizing the natural torsional frequency, is:

$$U^* = \frac{U}{f_T L} \tag{10}$$

In a generic phenomenon, if both torsion and flexion are important, fixing one of the coefficients determines the other. If, as in this case, flexion is much less important than torsion, it is not so necessary for the model to have an exact value of the flexion stiffness. However, it is necessary to ensure that the natural flexural frequency is substantially

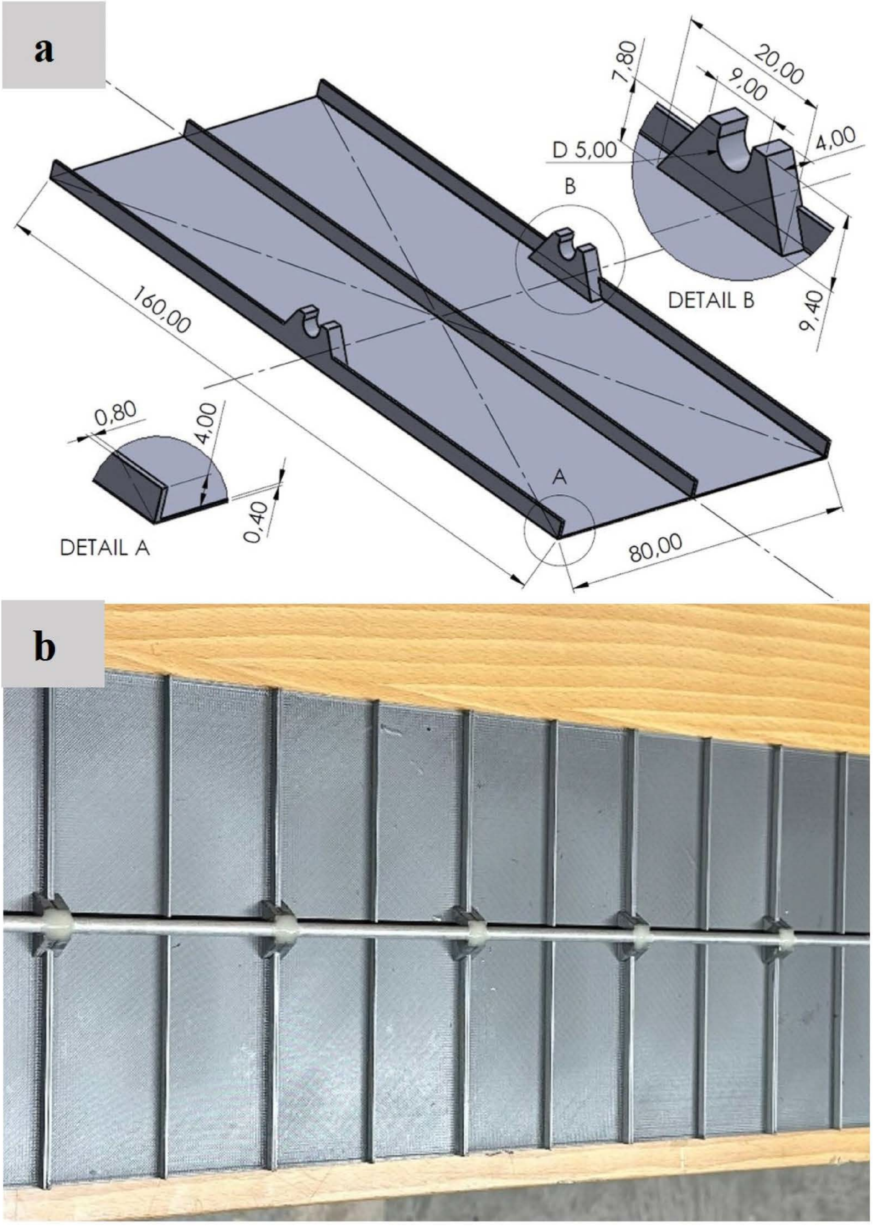

Fig. 2. Scale model panels: a) technical drawing; b) assembly on aluminum torque tube.

higher than the torsional frequency, so that the flexion in the model does not affect the results.

In the absence of external damping systems, the damping effect is determined by the structure and the movement of the torque tube in the support. It is in the range of 5%, somewhat larger than the typical values for steel bridges or buildings. It has been observed that, under these circumstances, the specific value is not significant for the critical velocities of the instability, as long as it is of the same order of magnitude (Martínez-García et al., 2021a). A study by Enshaei (Enshaei et al., 2023) has found that, in cases where external damping is used, higher values of the damping do not have an noticeable effect for tilt angles close to horizontal, but can substantially increase the critical velocity at higher tilt angles.

2.3. *Aeroelastic model specifications*

As the tracker is symmetric with respect to the middle plane at the motor pillar, it has been decided to define the model as a half-tracker. A scale ratio of $\lambda = 1/30$ has been chosen so that the length of the model is less than 1 m. With this scale, the model length is $L_m = 960$ mm, the chord $b_m = 160$ mm, and the height of the axis above the ground $H_m = 100$ mm. The panels and supports have been manufactured using 3D printing with PLA (Polylactic Acid), and a brass tube has been used for the torque tube.

2.3.1. *Panels*

To simplify manufacturing, the panels have been organized into groups of four (2v2h), resulting in a total of 12 groups per wing. A small gap has been maintained between them when mounted on the torque tube. It has been verified that this configuration does not modify the torsional stiffness of the model.

The panels are modeled with a PLA plate with a constant thickness of 0.4 mm, located at a distance of $h_m = 8$ mm from the axis. Three longitudinal purlins have been placed to make the bending stiffness of the plates – in the chord direction – equivalent to that of the prototype. The purlins are 4 mm depth and 0.8 mm width. Brackets have been designed to couple the panels to the tube (see Fig. 2), using epoxy resin.

The thickness of the panels has been calculated to maintain, as best as possible, the ratio of rotational inertia with the prototype, including the purlins and brackets. Assuming that the air density is the same in the model and prototype:

$$\frac{I_{Rm}}{I_{Rp}} = \left(\frac{L_m}{L_p}\right)^5 \tag{11}$$

The total rotational inertia of the model is $I_{Rm} = 2.17\cdot10^{-4}$ kg m^2. This value differs only by 3% from the due ratio.

It is not easy to print a uniform thickness of 0.4 mm, but it can be done if the printer is well calibrated. It would be easier to use a bigger thickness, but then the inertia cannot be maintained. Another solution is to design the panels as a frame on which a lighter material is fixed.

2.3.2. *Torque tube*

A 1-m-long brass tube (EN-CW507L) has been used. According to the scale ratio, the plates occupy $L_m = 960$ mm. The remaining 40 mm have been used to attach the model to the driver fixed end. The outer diameter of the tube is $D_m = 5$ mm, with a wall thickness of $e_m = 0.5$ mm. According to the scale, the diameter should be 6.6 mm, but a slightly smaller tube has been chosen to reduce the necessary air velocities in the wind tunnel. It has been found that the tube diameter does not significantly influence the phenomenon.

With the torque tube dimensions and a Shear Modulus for brass of $G = 40$ GPa, the model's torsional stiffness is $K_{Tm} = 1.51$ N m Eq. (12). The relationship between the stiffnesses of the model and prototype is an equation with a degree of freedom:

$$\frac{K_{Tm}}{K_{Tp}} = \left(\frac{U_m}{U_p}\right)^2 \left(\frac{L_m}{L_p}\right)^3 \tag{12}$$

By choosing a torsional stiffness for the model, the relationship between the real speed and the wind tunnel speed is fixed:

$$\frac{U_m}{U_p} = \sqrt{\frac{K_{Tm}}{K_{Tp}}\left(\frac{L_p}{L_m}\right)^3} = 0.78 \tag{13}$$

As shown below, this results in a minimum velocity for the onset of the instability around 8 m/s. This speed is small enough to accurately measure the phenomenon without applying excessive forces to the model, and large enough to maintain an adequate Reynolds number and reduce uncertainty in the measurement of fluid dynamic variables.

Two other models have been constructed with aluminum and carbon fiber tubes, to perform measurements with different natural damping and to confirm and complement the general stability results. The external diameter of the aluminum (EN-AW6060) is 5 mm and the internal diameter 4 mm. It maintains practically the same properties as the brass tube. However, its yield stress is lower, and the models are easily broken. The external diameter of the carbon fiber tube is 5 mm, and the internal diameter 3 mm. Carbon fiber models have very good durability and lower working speeds. The problem with carbon tubes is that the manufacturing dimensions are usually not as strict, and the mechanical properties are not as well known.

Regarding the shape of the tube, a circular section has been chosen, although it is true that some trackers use square or octagonal tubes, mainly to facilitate the attachment of panels. In the tests conducted, no significant influence of this factor has been found, but, in any case, it is possible to use square tubes or any other section for constructing the model. Additionally, a sleeve can be employed to alter the shape or size of the tube, to simulate its dimensions more accurately. It should be noted that when using non-circular tubes, special pieces are needed in the supports to achieve smooth rotation. Furthermore, for the Benchmark model, tubes with a constant section have been selected, although sometimes real trackers have a variable section.

2.3.3. *Theoretical natural frequencies*

The torsional frequency of the model, using Eq. (14), is $f_{Tm} = 20.85$ Hz, complying with the frequency relationship that must exist between the model and prototype:

$$\frac{f_{Tm}}{f_{Tp}} = \frac{U_m L_p}{U_p L_m} \tag{14}$$

Regarding the parameters involved in the flexural vibration, the mass of the panels and purlins can be calculated from the density of the used PLA (1240 kg/m^3): $M_m = 0.0991$ kg. This also complies with the similarity relationship:

$$\frac{M_m}{M_p} = \left(\frac{L_m}{L_p}\right)^3 \tag{15}$$

And the purlins have been dimensioned to meet the flexural stiffness relationship:

$$\frac{(EI)_m}{(EI)_p} = \left(\frac{U_m}{U_p}\right)^2 \left(\frac{L_m}{L_p}\right)^4 \tag{16}$$

Considering that the Young's modulus of PLA is $E = 3.5$ GPa, the model flexural stiffness obtained from the geometry is $(EI)_m = 0.17$ N m^2, which is only 1.6% lower than required.

2.3.4. *Support pillars*

The support pillars maintain the torque tube at a height $H_m = 100$ mm above the ground. The cross section of the pillars is 11 mm × 6 mm to achieve sufficient stiffness. The bending frequencies of the pillars are an order of magnitude higher than the frequencies previously considered. With more slender pillars, this would need further consideration. These pillars have been printed in PLA, with a conical grip to reduce friction with the tube and minimize the effects of angular misalignments (see Fig. 3). The grips are open to facilitate assembly. Models with bearings have also been built, however, it is difficult to achieve less friction and they have more problems of alignment and assembly (see Fig. 4).

Three pillars have been used, located at the positions corresponding to panels 7, 15, and 23 (counting from the motor), to obtain a relatively uniform distribution without interfering with the purlins. More pillars can be used, but these three, plus the torsion-fixed section at the motor position, are sufficient to minimize the displacement of the torque tube along its entire length. During their placement on the floor of the test chamber, it is crucial that they are correctly aligned with the axis. Otherwise, the forces in the supports can substantially increase friction. PLA clamps have been used to attach the pillars to the floor and simplify positioning. (see Fig. 5).

2.3.5. *Fixed support*

At the end of the tracker corresponding to the position of the drive motor, which is also the plane of symmetry, the torque tube is bound using a cap ending in a cylinder 10 mm wide and 40 mm in diameter. The cap is thick enough to prevent torsion and limit the effective length of the torque tube to 960 mm. The tube is attached to the cap with screws and adhesive (see Figs. 5 and 6).

This cap is supported by a thicker pillar ending in a bracket, completely restricting the displacement and rotational movement of the torque tube at that end. The bracket closes with a screw that allows to change the tracker tilt (see Fig. 7).

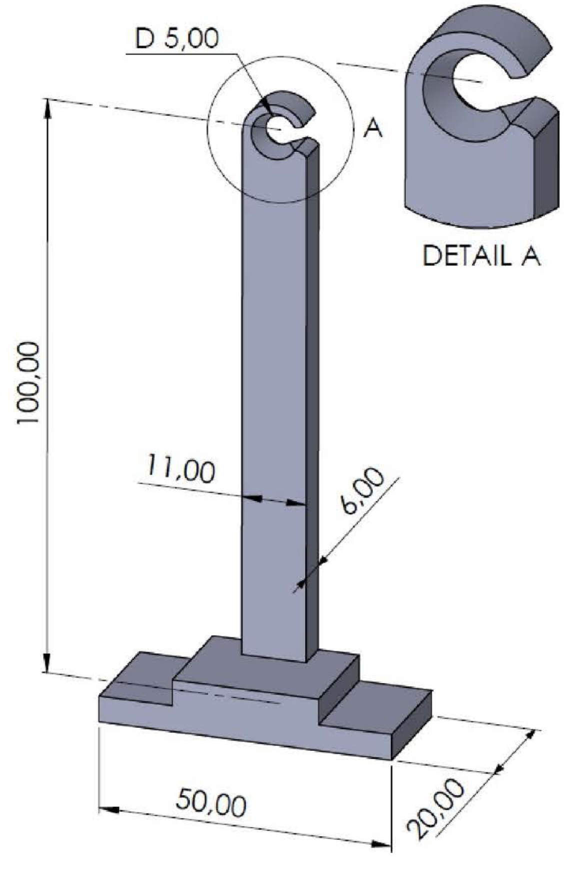

Fig. 3. Technical drawing of the support pillars with a detail of the grip.

Table 1 summarizes the geometric, elastic, mechanical, and dynamic characteristics of the prototype and of the 1/30 scale model.

3. Experimental methodology

The objective of the experimental tests conducted on the previously defined tracker model is to obtain precise and replicable information about its aerodynamic behavior, specifically the critical speeds for the onset of the torsional instability.

To guarantee controlled and easily reproducible conditions, the tests were conducted in uniform flow, with a single tracker, and the tracker's axis perpendicular to the flow. Given the variations depending on the tilt, a wide range of angles was tested, with particular attention to angles close to the horizontal.

The tests were independently performed in two wind tunnels, one at the University of Oviedo and the other at the Polytechnic University of Madrid.

3.1. *Wind tunnel and instrumentation of the University of Oviedo*

The tests of the University of Oviedo were carried out in the ETHAN50-ABLWT wind tunnel, located at the Campus of Mieres. This facility is a closed circuit with a length of 67 m and is equipped with four fans (180 kW). The test chamber is a square section of 1.5×1.5 m with a length of 10 m. The tests were performed in the uniform flow area. In this section of the chamber (see Fig. 8), the flow uniformity is 99%, the turbulence intensity is 0.5%, and the turbulence length scale is 0,04 m. Fig. 11 shows the boundary layer profile (c) and the turbulence non-dimensional power spectrum of the main flow (d). The blockage is 6.6% in the worst-tested configuration (60° angle) and usually less than 4%. The Reynolds number for the instability tests ranged between $8{\cdot}10^4$ and $1.5{\cdot}10^5$, taking the panel chord as the dimension.

A Wenglor CP35MHT80 laser distance sensor was used to measure the angle variation at the tracker's end. It has a resolution of 50 μm and a linearity of 0.15%. The accuracy in angle measurement is 0.07°. Additionally, a video system was available for continuous monitoring of the test and model movements. This system consists of two Ranger RC webcams with a video resolution of 4K.

The moment at the fixed end was measured with a balance designed to substitute for the fixed support (see Fig. 9). The balance has two load cells of 0.78 kg, with an accuracy better than 0.1%. It has been calculated that the complete system, including "in situ" calibration, can perform torque measurements with an uncertainty smaller than 1.8%.

A digital oscilloscope (KEYSIGHT EDUX1052A) was used to analyze the measurements during the test. The data was acquired using an ADLINK USB-2401 DAQ module. The module has a resolution of 24 bits and can sample 4 channels simultaneously at a maximum rate of 2 kS/s.

The measurements were performed with an acquisition frequency of 2000 Hz, and 76,800 data points from each sensor. The data were collected and processed in Matlab, using programs specifically developed by the research team.

3.2. *Wind tunnel and instrumentation of the Polytechnic University of Madrid*

The tests of the University of Madrid were performed in the ACLA16 wind tunnel, located at the Campus of Montegancedo. This facility is a controlled return circuit with a length of 20 m and is equipped with sixteen fans (120 kW). The test chamber is a square section of 2.2×2.2 m with a length of 17 m. The tests were performed in the uniform flow area. In this section of the chamber (see Fig. 10a), the flow uniformity is 99%, the turbulence intensity is 1.8%, and the turbulence length scale is 0.1 m. Fig. 11 shows the boundary layer profile (a) and the turbulence

Fig. 4. Assembly of the panels, torque tube and pillars: a) general view; b) detail of the version with bearings and screw clamping.

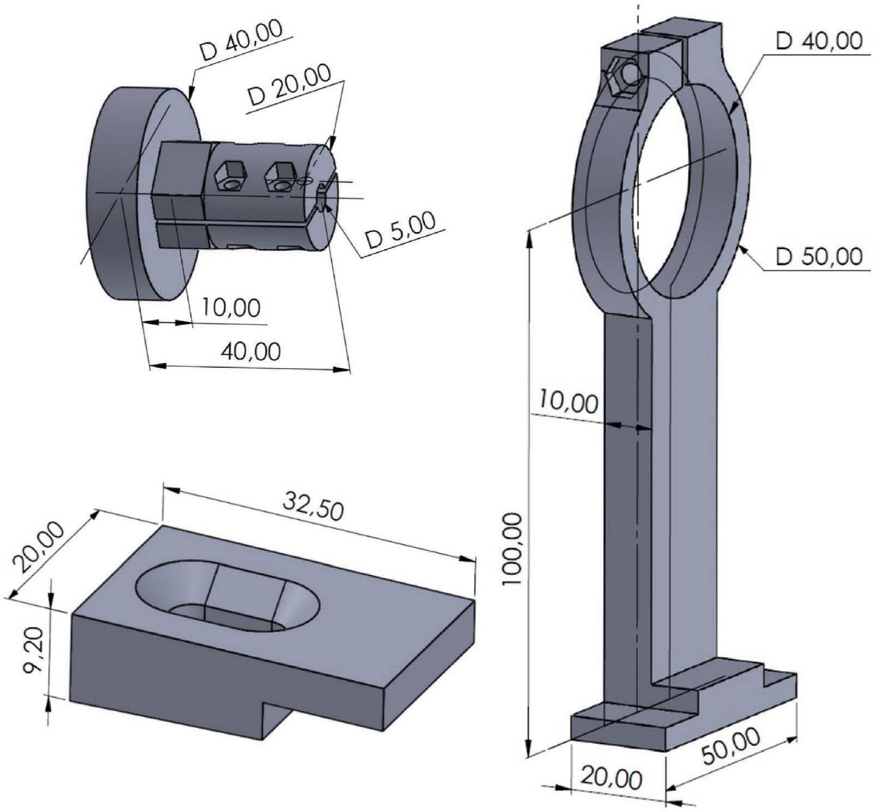

Fig. 5. Technical drawing of the cap, clamp and the fixed support.

Fig. 6. Detail of the fixed support with the cap and tracker.

Table 1
Prototipe and model characteristics.

GENERAL DATA	SYMBOL	PROTOTYPE	SCALE MODEL
N° PV Panels		48	12
N° Pillars		1 (driver) + 3	1 (driver) + 3
Panel size		2.4 × 1.2 m	0.160 × 0.080 m
Arrangement		2P	2P
Length	L	28.8 m	0.960 m
Chord	b	4.8 m	0.160 m
Aspect Ratio	AR	12	12
Height	H	3.0 m	0.100 m
Torque tube diameter	D	0.200 m	0.005 m
Torque tube thickness	e	0.004 m	0.0005 m
Clearance	h_p	0.24 m	0.008 m
Torsional stiffness	K_T	$6.64{\cdot}10^4$ N m	1.51 N m
Natural frequency, torque tube torsion	f_T	5.65 rad/s	131.03 rad/s
Mass	M	2592 kg	0.099 kg
Inertia	I_R	$5.14{\cdot}10^3$ kg m^2	$2.17{\cdot}10^{\ 4}$ kg m^2
Flexural stiffness	EI	$2.30{\cdot}10^5$ N m^2	0.17 N m^2

non-dimensional power spectrum of the main flow (b). The blockage is 3.1% in the worst-tested configuration (60° angle) and usually less than 2%. The Reynolds number for the instability tests ranged between $8{\cdot}10^4$ y $1.5{\cdot}10^5$, taking the panel chord as the dimension. A schematic view of the wind tunnel of the University of Oviedo is also shown in Fig. 10b.

The angular motion of the solar tracker was measured through a laser system using the Mikroelektronik M1L200 sensor, featuring a resolution of 0.4 mm and a measurement range of 5–25 cm. The analog voltage output ranging from 0 V to 5 V was recorded through a LabView analog-to-digital converter at a sampling frequency of 1000 Hz and 30 s.

3.3. *Natural frequency of the model*

The natural frequencies of the model were experimentally determined through free vibration tests. The temporal signal shown in Fig. 12 represents the angular measurement by the laser at the free end of the model, and the torque at the fixed end, after an external excitation in the absence of airflow.

Fig. 13 displays the power spectrum of this free vibration test signal. The peak at 17.25 Hz, corresponding to the largest amplitude, is the principal natural frequency associated with the torsional mode of the structure. This frequency is slightly lower than the theoretically calculated 20.8 Hz. The reason for this discrepancy is that the torsional stiffness, which depends mainly on the Shear Modulus of the material, is lower than expected. The inertia of the panels has been checked weighting the panels. Although the difference is small, these factors underscore the importance of experimentally measuring the torsional frequency, rather than relying on theoretical calculations.

In the power spectrum, the use of a logarithmic scale reveals other low-amplitude excitations at higher frequencies that are related to harmonics of the first natural frequency, and also to higher-order vibration modes. In particular, the frequency peak appearing at 40 Hz in both signals may be a second-order vibration mode of the torque tube.

Regarding the flexion of the panels, experiments were conducted on isolated elements which revealed a plate bending frequency of approximately 69.75 Hz. The peaks in the angular signal at this frequency and at 35 Hz could be related to this flexion. It can be assumed that they do not appear in the torque signal because the excitation was applied near the end, where the laser is located, and not over the entire length of the plate.

In this case, it can be considered that the basic torsional frequency is the only significant frequency, as the amplitudes of the secondary frequencies are an order of magnitude lower.

The damping coefficient can be obtained from the amplitude decay of the temporal signal, (Chopra, 2012):

$$\zeta = \frac{\delta}{\sqrt{4\pi^2 + \delta^2}}, \text{with } \delta = \frac{1}{n} ln\left(\frac{x(t_i)}{x(t_{i+n})}\right) \tag{17}$$

Where $x(t_i)$ and $x(t_{i+n})$ are the amplitudes of peaks i and $i + n$ respectively.

This damping coefficient, $\zeta_m = 0.027$, aligns quite well with the typical values of metallic structures. Previous research has found that, for natural values of damping (without external damping), this dimensionless number does not influence the critical velocity of the instability (Martínez-García et al., 2021a). In this case, aluminum ($\zeta_m = 0.038$) and carbon fiber ($\zeta_m = 0.031$) shafts were also tested, yielding similar results.

4. Results

As previously discussed, the tests were carried out on an isolated tracker, equivalent to a first-row tracker, with the incident wind perpendicular to the axis. Velocities during these tests were uniform (no atmospheric boundary layer), and with the least possible turbulence in the tunnels.

4.1. *Moments and deformation prior to torsional instability*

The deformation and stresses on the tracker, even before the onset of the instability, are rather complex due to the non-linear variation of the angle along the tracker. Even at zero tilt angle, it does not remain perfectly horizontal as the presence of the ground implies an asymmetry of the pressures on the upper and lower surfaces. Torsional deformation along the axis is concentrated in the last third of the axis, with an approximately sinusoidal distribution: it increases rapidly near the anchoring point, but the increase in deformation decreases towards the

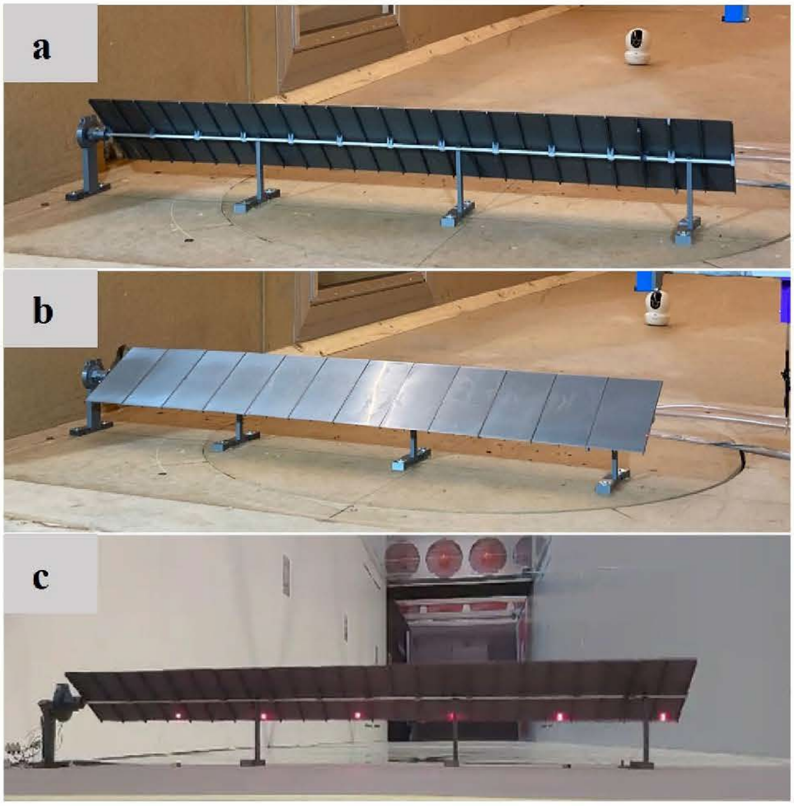

Fig. 7. Tracker setup in the test chamber; a-b) University of Oviedo; c) UPM IDR, Madrid.

Fig. 8. Test setup in the wind tunnel of the University of Oviedo.

free end, where maximum deflection occurs. Due to this twist, the horizontal stresses are greater than those corresponding to a rigid flat plate with the same initial angle. The vertical stresses and moment can be either greater or lesser, depending on the tilt.

Fig. 14 shows, for a model with a 20° tilt, the moment and the angle variation with the velocity, from zero up to the point where the instability begins. The angle variation is the increase in angle at the tracker's end compared to the initial tilt. The distribution of both variables appears to follow a quadratic pattern, and there is no noticeable change in trend as the instability is approached.

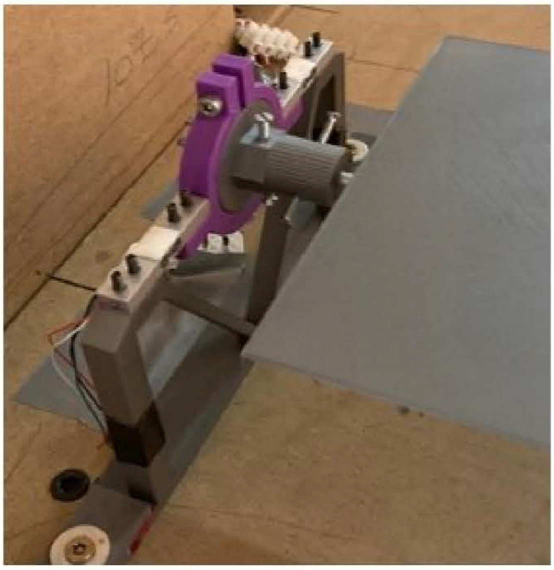

Fig. 9. Detail of the force balance.

In Fig. 15, the moment coefficient at the fixed end for various tilts is plotted as a function of the reduced velocity. The velocities range from near zero up to the torsional instability for each tilt. Except for the lowest velocities, the moment coefficient remains practically horizontal, corresponding to a quadratic relationship between the absolute torque and the velocity. The maximum velocity before the instability is different for each tilt. Except for the 0° angle, there is no change of sign in the values, nor sudden variations when approaching instability. These values can be used for static calculations, but the trends do not allow for the determination of the instability's origin. However, they do confirm that the Reynolds number used is sufficiently high.

Fig. 16 shows the variation of the torque coefficient as a function of the tilt angle for the Benchmark model with a reduced velocity of 2.2. These are compared with experimental values for a sectional tracker model (Taylor et al., 2024) and with a flat plate with an infinite aspect ratio (ESDU70015) and no floor. The values of the Benchmark model fit fairly well with the other two, although some deviations are observed, especially for positive angles. The differences can be attributed to the difference between positive and negative angles with respect to the ground in the models, in contrast to the plate without ground. There is also some variation near the zero angle, attributable to the twist of the Benchmark model with respect to the sectional one and the flat plate.

4.2. Torsional instability

As previously stated, when the air speed increases, the tracker undergoes torsional deformation, resulting in an increase in the angle at the end. For tilt angles ranging from at least +35° to −45°, if the speed continues to increase, an instability point will be reached, and the tracker will begin to oscillate torsionally (see Fig. 17). Above this critical velocity, the amplitude of oscillation is relatively stable if the air speed is constant, but grows very rapidly if the speed increases, potentially compromising the structural integrity of the tracker. For example, in Fig. 18, the Benchmark model can be seen at a moment of strong instability, with a twist of more than 30° from the fixed end to the free end.

The phenomenon is complex and may exhibit different characteristics for various tilt angles. For tilt angles from medium to high (about 10–35 and -10 to −45), it can be said that it is generated by the aeroelastic interaction between the tracker torsion and the vortex at the leeward side of the leading edge. In a simplified way, the vortex oscillation causes the aerodynamic force to fluctuate, thus changing the panel torsion, and the panel torsion generates a larger vortex oscillation. If the amplitude is sufficiently large, the oscillation of the panel forces the separation of the vortices at the extreme positions of the movement, as shown in the smoke visualization performed on a small wind tunnel built for this purpose (see Fig. 19). Technically, as has been described by Martínez-García et al., (2021a, 2021b), Taylor et al. (2024) and Cárdenas-Rondón et al. (2023), for example, the instability occurs when the combination of structural damping and aerodynamic damping reaches negative values, rendering the equation of motion unstable. The frequency of this motion is linked to the structure's natural frequency, although it is slightly lower, as the stiffness, inertia, and damping of the aerodynamic forces combine with the mechanical characteristics. Some authors, Enshaei et al. (2023), describe this instability mechanism as vortex lock-in, characterized by Von Karman vortex-street shedding from alternating edges of the leeward side, which may transition to cyclical torsional divergence if the tracker motion grows significantly.

For tilt angles roughly between −10° to 10° there are several explanations. For example, Cárdenas-Rondón et al. (2023), Zhang et al. (2023) and Martínez-García et al., (2021a, 2021b), assume the mechanism is similar to the aeroelastic mechanism already described, although the last suggest that a minimum tilt angle or kinetic energy may be needed for the instability. Other authors (Taylor et al. (2024); Enshaei et al. (2023)) postulate that in this zone, the mechanism is that of torsional divergence, as described by Scanlan and Sabzevarit (1969) with non-linear effects contributing to the cyclic nature of the phenomenon.

Fig. 20 shows the angle at the free end of the tracker and the moment at the fixed end as a function of time. It was measured simultaneously with the laser distance sensor and the torsion balance. It corresponds to a tilt angle of 20° and a velocity of 8 m/s, where the tracker is in full developed instability. Both sensors equally detect the disturbance, although the displacement signal is usually neater than the load cells signal.

In the power spectrum of these signals (see Fig. 21), the only significant frequency is 11 Hz and its harmonics. This frequency is significantly lower than the natural frequency (17.25 Hz) of the first mode of vibration. The harmonics of this frequency have a relatively large value, indicating that the signal deviates from the ideal sinusoidal waveform. Higher modes of vibration are not appreciable.

Measurements of the angle and the torque have been taken at different wind speeds, from below the critical velocity to well into the oscillation. The cascade and 2D contour plot depicted in Fig. 22 were created using the power spectra of the angle signal. In the cascade, the amplitude is represented on a linear scaler and, in the contour plot on a logarithmic one. The frequency is non-dimensionalized with the natural frequency, and the velocity with the natural frequency and the chord (reduced velocity). The amplitude of the torsional oscillation can be observed to increase rapidly with the velocity. Additionally, it starts at a frequency slightly below the natural frequency and decreases a little with increasing velocity.

4.3. Criteria and methodology for defining critical speed

Fig. 23 shows the variation of the angle at the free end of the tracker, with respect to the original position, as a function of the velocity, for three different tilts. Or, rather, the mean value of the variation, where there is vibration. Also shown is the amplitude of the signal oscillation. At the beginning of the instability, there is a change in the slope of the angle variation, but it is not clear enough to determine the onset. However, the amplitude of the signal oscillation shows a sudden change that is more suitable for this task.

Despite this sharp increase in amplitude, a practical definition of the critical speed presents several challenges. First, when measured with

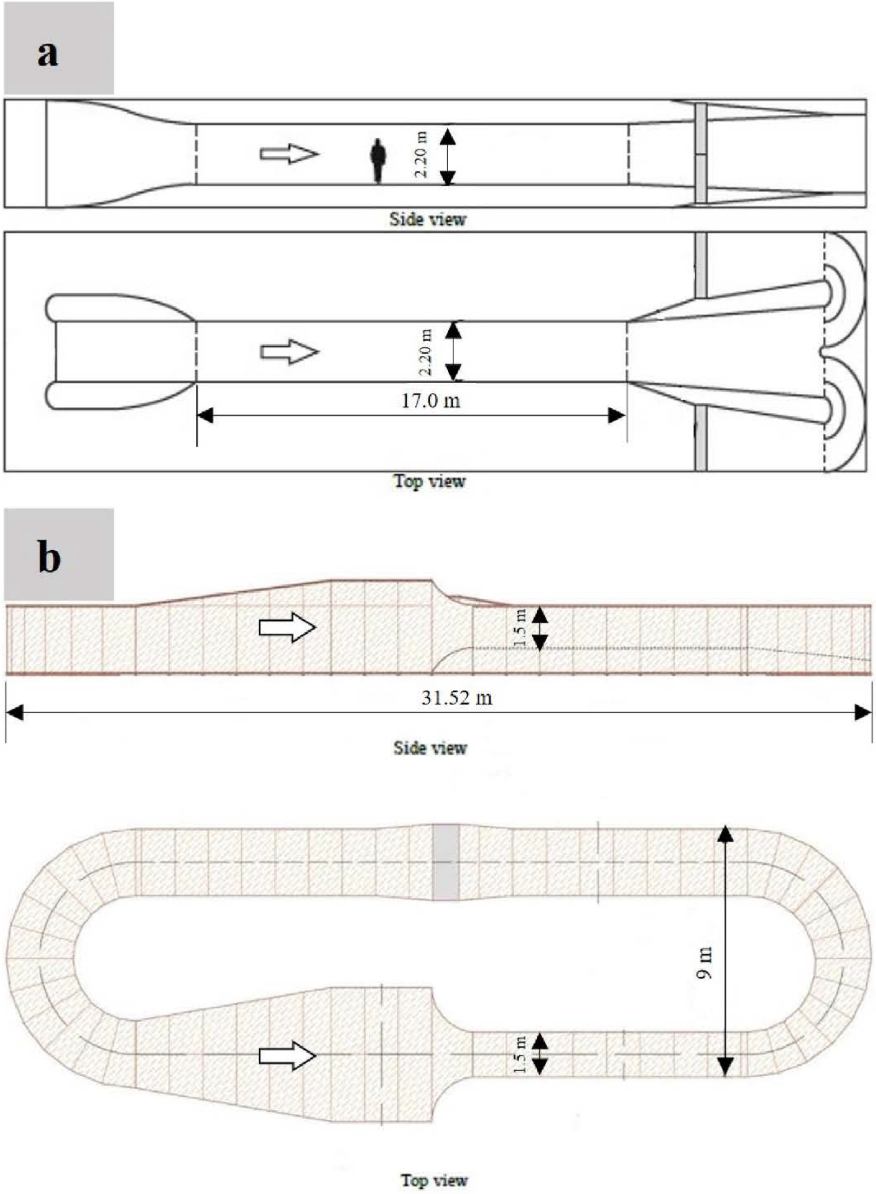

Fig. 10. Wind tunnel sketches: a) Wind Tunnel ACLA16 at UPM IDR, Madrid; b) Wind tunnel ETHAN50-ABLWT at the University of Oviedo.

sufficient precision, the angle is not completely stable, even when the velocity is lower than critical. This is due to electrical noise in the signal, flow turbulence (however low), and other potential mechanical and aerodynamic phenomena.

Second, for certain tilts, the inception of the phenomenon is not entirely continuous. As the critical velocity is approached, cycles of oscillation begin to appear, interspersed with intervals of stability (see Fig. 24).

Finally, there have been instances where hysteresis has been observed. If the air speed is increased until instability appears and then decreased until it disappears, the onset velocity is higher than the cessation velocity. This behavior could be due to friction, but it may also be linked to the characteristics of the aeroelastic phenomenon. Regarding the former, the effect has been clearly observed when the friction in the supports is high due to poor adjustment or misalignment. It is also more evident at large angles, where the horizontal force increases - increasing the net value of the friction force - at the same time as the moment decreases because the aerodynamic force is centered on the panels.

With respect to the noise and other fluctuating effects, it has been decided to define the onset point when the oscillation reaches an RMS value of one degree for at least 10 s. If the force on the axis is being used as the measurement, this one-degree value can be replaced by the equivalent moment value, according to the torsional stiffness of the

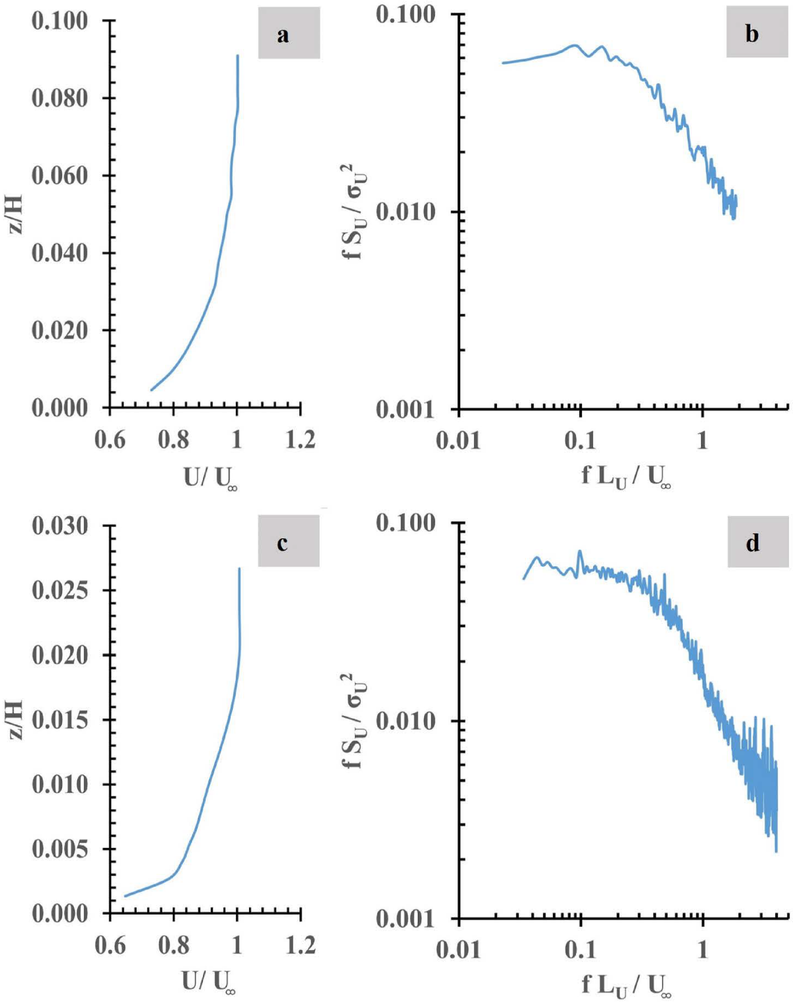

Fig. 11. Wind tunnel boundary layers and turbulence non-dimensional power spectrum of the main flow: a) and b) Wind Tunnel ACLA16 at UPM IDR, Madrid; c) and d) Wind tunnel ETHAN50-ABLWT at the University of Oviedo.

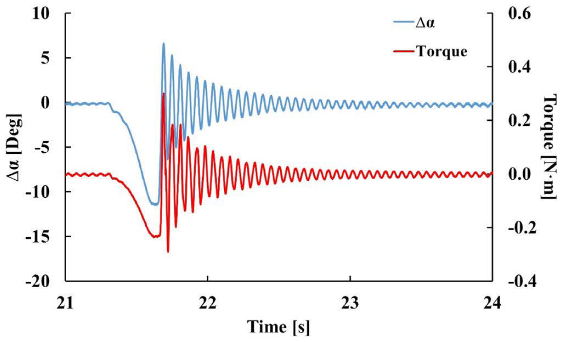

Fig. 12. Time signals of the free vibration test (model with brass torque tube).

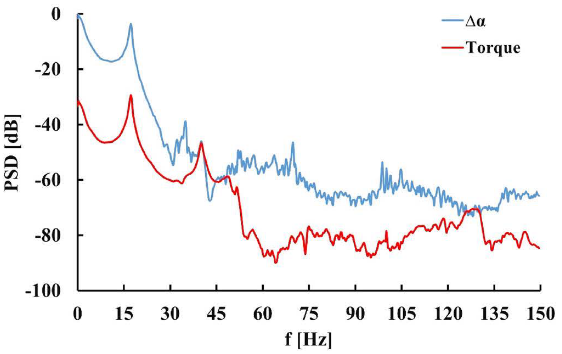

Fig. 13. Power spectrum of the free vibration test (model with brass torque tube). Power spectral density in decibels, units: [deg^2/Hz], [(Nm)^2/Hz].

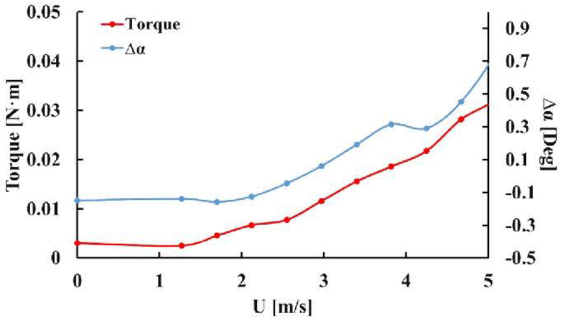

Fig. 14. Variation of angle at the free end, and averaged torque at the fixed end, in function of the velocity before the onset of the torsional instability. Brass tube model, 20° tilt.

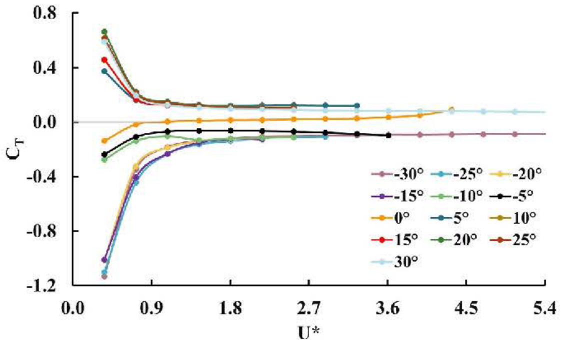

Fig. 15. Moment coefficient at the fixed end as a function of reduced velocity for various tilt angles. Velocities up to the onset of the instability. Brass tube model.

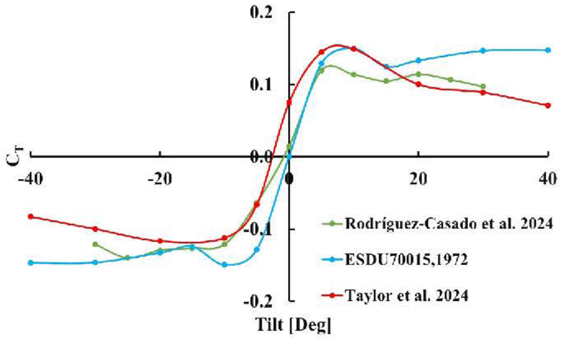

Fig. 16. Moment coefficient as a function of tilt before the onset of instability. Model with brass tube at U* 2.2, flat plate with an infinite aspect ratio and sectional model.

model. The signal should be acquired at least at a frequency ten times higher than the natural frequency. Mathematically speaking, as the oscillation is considered the variation over the mean value, or what would be the RMS of the alternating signal in an oscilloscope, the function to use is the standard deviation. The value of 1° RMS for, at least, 10 s is considered the optimal choice for detecting instability early on, without being affected by signal alterations. With respect to the time, 10 s on the model corresponds to 3.8 min in the prototype. This value has been found to be sufficient for laboratory measurements but perhaps for full-scale measurements it might be better to use 10 min to be more in accordance with the standards. With respect to the magnitude of the angle. The visual assessment matches well with both the wind tunnel and reality, as the angles coincide in both. One degree may seem too strict since an oscillation of a few degrees may not be dangerous for the structure. However, it is considered important to detect the instability as early as possible, because, in the long term, it could lead to fatigue damage.

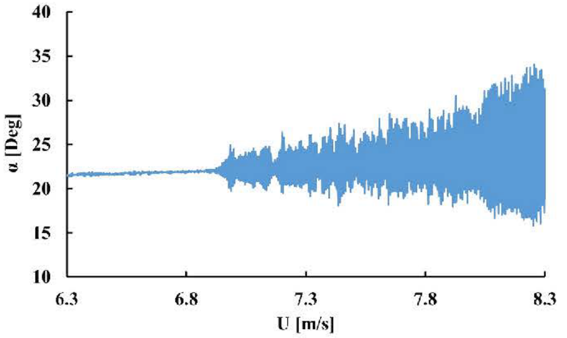

Fig. 17. Angle at the free end of the Benchmark model as the air velocity is continuously increased. Tilt: +20°.

Regarding hysteresis, it has been considered that the most effective method for identifying the critical speed is to increase the speed until instability is reached, and then decrease it until the RMS of the oscillation is less than one degree. In this way, the tracker is in motion, reducing friction, and achieving the lowest possible hysteresis value.

For tilt angles greater than 30° or less than −40°, it has been found that the tracker may become unstable if manually excited, even if the vibration does not trigger with an increase in wind speed in the wind tunnel. This is considered acceptable because, an atmospheric gust or lower friction in the supports could cause a similar effect.

4.4. Stability diagram

The critical speed for the onset of the torsional instability has been determined for the full range of tracker tilt angles using the aforementioned criteria and methodology. The stability diagram in Fig. 25 represents these values, plotting the critical reduced speed for each tilt angle. The reduced speed is defined as non-dimensional using the chord of the tracker and its natural vibration frequency (in Hz).

The figure displays data from the Wind Tunnel of the University of Oviedo and the Polytechnic University of Madrid, using trackers made of both brass and aluminum tubes. The results obtained from both sources are highly coherent, confirming that the proposed Benchmark model allows to obtain repeatable and reliable results.

In the figure, the instability zone above the curve is shaded. The tracker is stable for velocities lower than the critical for each tilt, and unstable for higher velocities. As previously discussed, this instability does not disappear as the velocity increases, but rather the amplitude of oscillation increases, leading to the tracker's failure.

Fig. 26 shows the comparison of the results with some of the published diagrams for experimental models of both 3D and sectional 2D trackers (Banks, 2019; Cárdenas-Rondón et al., 2023; Catalán et al., 2020; De la Viña et al., 2021; Enshaei et al., 2023; Martínez-García et al., (2021a, 2021b); Taylor et al., 2024; Zhang et al., 2023; Zwingmann et al., 2020). To ensure comparability, due to the disparity in the variables used and the lack of specific data, the values of each diagram have been non-dimensionalized with their minimum critical speed. The correlation is very acceptable, especially considering the disparity of geometries and experimental methodologies. The existence of a relative maximum in the vicinity of -1° of tilt is generalized. In the negative tilt

Fig. 18. Twisting of the Benchmark model in developed torsional instability.

branch, there are two groups of results, differing in the relative value of the critical speed minimum (higher or lower than the minimum of the positive branch). The greatest discrepancy found is the determination of the points at which the critical speed begins to increase, for positive tilt angles from +25° and negative from −30°, depending on the authors, and the value of the critical velocity for those tilt values.

Some of the characteristics of the results are discussed in the following sections.

4.4.1. Asymmetry and limits

Despite using a uniform velocity in the tests, the stability diagram is not symmetrical, as can be seen in the figures. The midpoint is towards -1°, the limits reach +35° in the positive zone and −45° in the negative, and the minimum values are somewhat lower in this branch. These effects are a result of the proximity of the ground and the location of the torque tube below the panels.

Above +35° and below −45°, the torsional instability develops with greater difficulty and eventually disappears. The discontinuation may be attributed to the increase in drag force, which generates greater friction in the axis, along with the reduction of moments as the angle increases. It may also be affected by the closer proximity of the panel edges to the ground, and its effect on vortex shedding. Due to the exponential increase of the critical velocity at those angles, the definition of the limits is generally imprecise because models have difficulty withstanding the stresses involved. Typically, this is not a significant issue since the focus is on determining the minimum velocities at which instability occurs. However, it may be crucial in establishing a stow position at high angles.

4.4.2. Angles close to horizontal

In the +-10° zone, the critical velocity values are higher. Not as high as, presumably, at the extremes, but about double the minimum value. This should be taken only as an approximation. It has been determined that in this area, there is a significant amount of uncertainty and variation among trackers (Martínez-García et al., 2021b).

Fig. 27 illustrates the tracker's torsion just before instability for various tilts, indicating the increase in angle at the end compared to the original angle. The variation is typically around two degrees for most tilt angles, but it can reach up to six degrees when close to the horizontal. Although the concrete values are specific to this tracker and depend on the structural variables, a marked difference is always found between the angles close to the horizontal and the rest of the tilt angles. This effect may be attributed to the need for excitation caused by vortex shedding at the leading edge, which requires a minimum angle. It may also be influenced by the fact that the absolute moments are small at angles very close to zero, at least until a certain torsion in the tracker has occurred. Additionally, there may be a requirement for a different minimum kinetic energy for each tilt.

As explained previously, some authors have postulated that the phenomenon is different in this zone. In any case, this topic requires more in-depth research.

4.4.3. Vortex induced vibrations

It has been observed that, for angles greater than 10° and less than −10°, an oscillatory phenomenon appears at velocities lower than the critical ones. This phenomenon can be detected when the amplitude in the power spectra cascades is represented in decibels (logarithmic scale), as shown in Fig. 28. The graph illustrates the instability caused by the 1DOF flutter above a reduced speed of 2.5, with a principal frequency around 0.75 (relative to the natural frequency) and around 1.5 for the first harmonic. Additionally, a vibration occurs at the relative frequency of 1, beginning approximately at the reduced velocity of 1 and disappearing at 1.75.

This phenomenon has been identified as "vortex induced vibration" because it appears very close to the natural frequency of the structure, has a limited amplitude, and disappears as the speed increases. Also, the St number of a flat plate at that angle is 0.6 (Chen and Fang, 1996) which makes the reduced velocity corresponding to the vibration due to vortex shedding 1.6.

For some of the studied angles, especially those with lower critical speeds, before this phenomenon disappears, torsional instability begins to emerge. For other angles, however, a separation between them is noticeable, allowing the assumption that this vortex induced vibration is not necessary for the appearance of torsional instability.

The criterion used for critical speed is above the amplitude of these vibrations. This phenomenon may be important with respect to the fatigue resistance of trackers but does not have the structural dangers of torsional instability.

4.4.4. Magnitude of oscillation variation (RMS bands)

As previously stated, a value of one degree RMS is considered the most accurate for accurately detecting the instability. However, a study has been conducted to determine the influence of this value on defining the critical velocity. Fig. 29 shows the zone between the RMS of 0.1 and 2.5, in addition to the line of critical velocity defined with an RMS of 1.

The distance between 1 and 2.5 can be considered as an indication of the upward gradient of the oscillation. Above 30° and below −30°, as well as in the range of ±5°, there is hardly any separation between these values, indicating a very abrupt instability. The other angles, especially the positive ones, show a relatively more gradual growth.

The RMS 0.1 values, on the other hand, are more influenced by background noise, turbulence, and other aerodynamic phenomena. For example, for angles of −35° and −40°, they occur at a notably lower speed. It has been found that this is because, in that zone, vortex-induced vibrations have a somewhat greater amplitude.

Fig. 19. Smoke visualization of the torsional instability.

4.4.5. *Tracker at the end and in the middle of the row*

The methodology employs symmetry to simulate the embedding of the drive motor in the middle of the tracker, leaving the free end in an open flow area. This makes the model representative of a tracker at the end of the row. Tests have also been conducted using a screen at the end of the model to simulate the behavior of a tracker in the middle of the row (see Fig. 30).

There is no significant difference between both models for the 1-degree RSM. However, the band between RMS 0.1 and 2.5 is narrower at many points for the test with the screen, suggesting that instability occurs more abruptly. It is quite possible that the behavior in oblique winds is quite different, but for the flow perpendicular to the axis, the boundary effect does not seem to have an appreciable impact on the critical velocity.

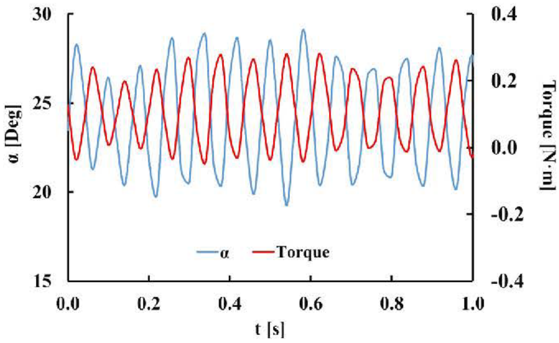

Fig. 20. Angle at the free end of the tracker and moment at the fixed end as a function of time in full developed instability. Brass tube model with a tilt angle of +20° and a velocity of 8 m/s.

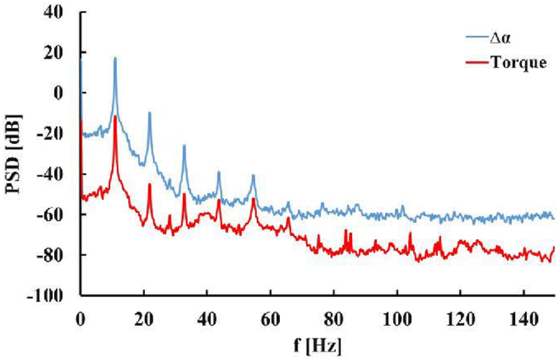

Fig. 21. Power spectrum of the angle and torque for the brass tube model at +20° and a velocity of 8 m/s. Power spectral density, units: [deg^2/Hz], [(Nm) 2/Hz].

5. Conclusions

A Benchmark model of a single axis photovoltaic solar tracker has been defined in the present study. This model reproduces the basic geometry and structure of typical commercial trackers with emphasis on their 3D dynamic characteristics, so that it is suitable to study flow-structure interaction phenomena in wind tunnel, such as aeroelastic torsional instability. The geometrical dimensions and construction details of this canonical model have been specified so that it can be accurately replicated. Besides, an analysis has been presented on the similarity conditions associated to the aeroelastic behavior of the trackers. This includes determining the first natural frequencies for torque tube torsion, both from the structural properties and experimentally, and the non-dimensional coefficients for panel bending.

The proposed canonical model has been tested in two wind-tunnels, one at the Polytechnic University of Madrid (IDR-UPM) and the other at the University of Oviedo (UniOvi). In both cases, models in single row configuration were subjected to low turbulence uniform flow perpendicular to the tracker axis, to obtain detailed and reliable data on the aerodynamic response. In particular, the critical wind velocity above which torsional instability develops was determined for a range of tracker tilts, by means of previously defined methodology and criterion. The plots of reduced critical velocity as a function of tilt obtained from the measurements at both wind tunnels are in good agreement. This plot delimits the stable and unstable regions for torsional instability and therefore it is key to establish safe operation conditions at real PV plants.

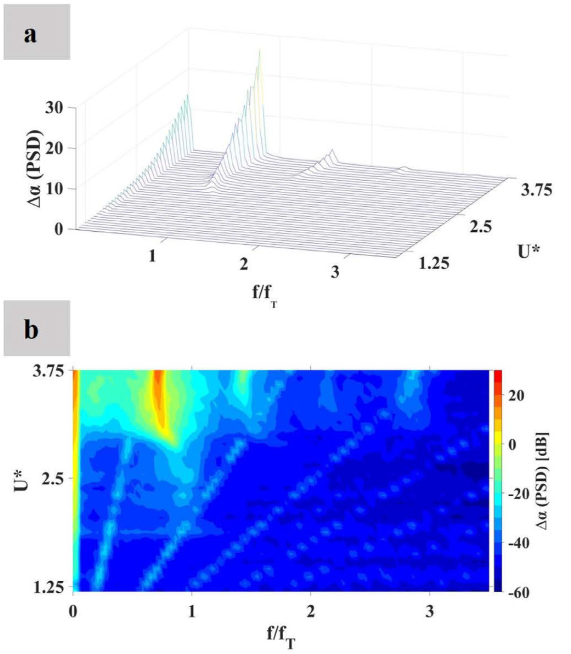

Fig. 22. Power spectra of the angle signal for different reduced velocities. Frequency non-dimensionalized with the natural frequency. Benchmark model at +20°. a) Cascade of power spectral density, magnitude on a lineal scale, units: [deg2/Hz]. b) 2D contour plot of power spectral density, magnitude on a logarithmic scale, units: [dB].

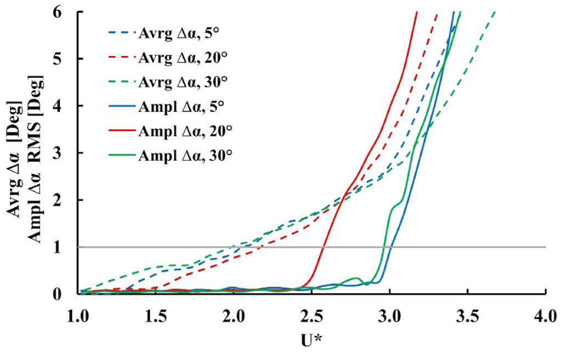

Fig. 23. Mean value of the variation of the angle at the free end of the tracker and amplitude of oscillation, in function of the reduced velocity, for the brass tube model at three tilt angles.

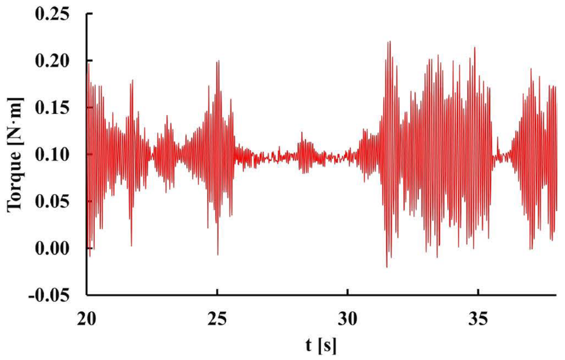

Fig. 24. Temporal signal of pulsatory torsional instability, Benchmark model at 30°, with 2.9 reduced velocity.

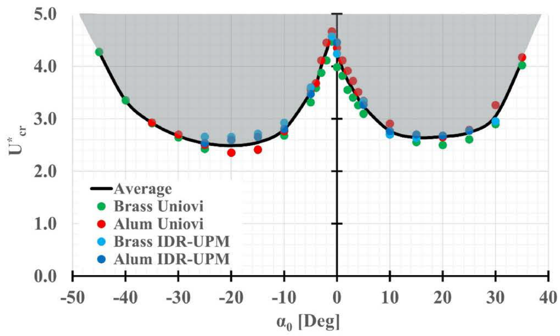

Fig. 25. Stability diagram of the Benchmark Tracker.

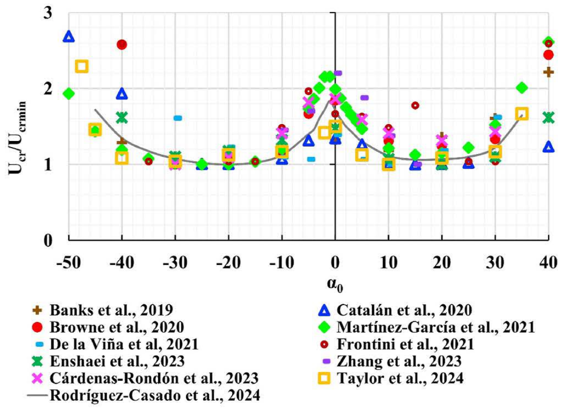

Fig. 26. Comparison of some of the experimental stability diagrams published since 2019.

In addition, several characteristics of the stability diagram were further analyzed, such as the maximum and minimum tilt angle, asymmetry with respect to zero tilt, critical velocity values at low tilts, and vibration amplitude when operating close to threshold conditions. Besides, vortex induced vibrations were identified at wind speeds below the critical values for several tilts. A brief assessment has also been provided on the effect of tracker relative position by comparing mid-row to end-of-row locations.

A stability diagram was adapted to compare the results of the present study to experimental data available in the literature, including both sectional and 3D models. Although the general trends are similar, some significant discrepancies have also shown up in the reported data regarding the critical velocity values. This only confirms the need for a systematic way to validate different testing methodologies, which is the objective of the Benchmark model now proposed.

Therefore, it is expected that this Benchmark will serve as a reference to homologate the studies on tracker aeroelasticity and provide reliability to the resulting data, thus overcoming the current limitations of conventional standards. That will help to optimize the design of PV structures while ensuring safe operating conditions under wind loading,

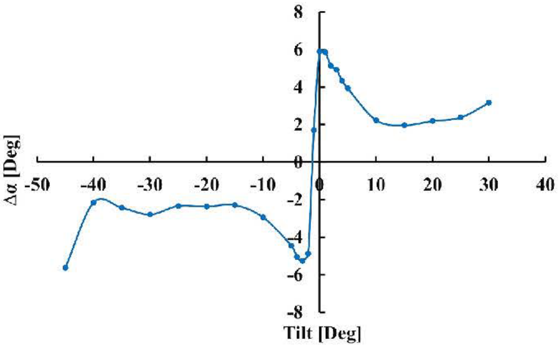

Fig. 27. Torsion of the tracker from fixed-end to free-end at critical speed in function of the tilt.

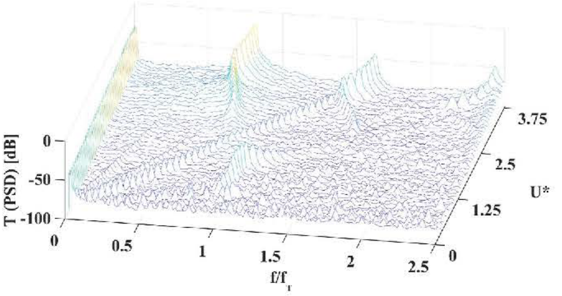

Fig. 28. Cascade of power spectra in decibels (torque signal) for different reduced velocities, showing VIV and 1 DOF Flutter. Benchmark model at +10°. Power spectral density in decibels, units: [$(Nm)^2/Hz$].

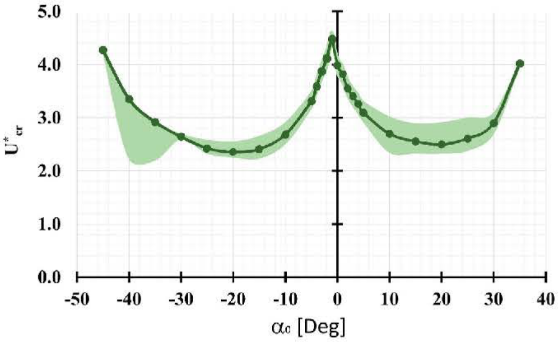

Fig. 29. Stability diagram with line at RMS 1 and shadowed zone between RMS 0.1 and 2.5 RMS. Benchmark model with brass tube tested at the University of Oviedo.

therefore reducing the construction and maintenance costs of solar PV plants.

CRediT authorship contribution statement

Carlos Rodríguez-Casado: Visualization, Software, Resources, Project administration, Methodology. **Eva Martínez-García:** Supervision, Data curation. **Raúl Manzanares-Bercial:** Validation. **José Luis Ruiz-Moral:** Writing – review & editing. **Eduardo Blanco-Marigorta:** Formal analysis, Conceptualization. **Antonio Navarro-Manso:** Writing – original draft, Investigation, Funding acquisition.

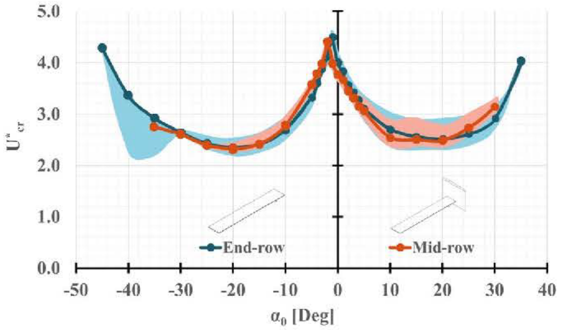

Fig. 30. Comparison of the stability diagram of the model simulating the end of the row and the middle of the row. The lines correspond to RMS 1, and the shadowed zones to the range from RMS 0.1 to 2.5. Benchmark model with brass tube.

Declaration of competing interest

The authors declare that they have no known competing financial interests or personal relationships that could have appeared to influence the work reported in this paper.

Data availability

Data will be made available on request.

Acknowledgments

To Carlos and Eduardo for all the models they made for us (and that we broke). To Maria from the “Taberna Irlandesa” for the beers and the encouragement. The authors would also like to thank Marta Ordóñez García, Claudia González Gutiérrez, Paúl Cruz Llorente, Pedro Gonçalves Caunedo and all the people from ESOLIA-SOLTRACK for their participation in the destruction of the models and their help during the tests. In the elaboration of this work, we have also benefited from the invaluable assistance of Professor Angel Sanz-Andres, IDR/UPM Director, Professor Sebastián Franchini Longhi, Professor Jorge Parrondo Gayo and Professor Juan Andrés Cárdenas-Rondón.

This work is part of the project TED2021-130541B–C21 funded by MCIN/AEI/10.13039/501100011033, the European Union “NextGenerationEU”/PRTR and project PID2022-137630OB-C21 financed by MCIN/AEI/10.13039/501100011033/FEDER, UE.

References

Adeleke, B., 2016. Experimental and Finite Element Analysis of Wind Induced Displacement of a Dual axis Photovoltaic Solar Trackers. University of Ottawa, Ottawa.

American Society of Civil Engineers (ASCE), 2021. Wind Tunnel Testing for Buildings and Other Structures, twenty-first ed. American Society of Civil Engineers, Reston, Virginia, p. 49th.

Armandei, M., Fernandes, A.C., 2014. Torsional instability of an elastic flat plate due to hydrodynamic loads. J. Mechanics 30, 643–650. https://doi.org/10.1017/jmech.2014.28.

Banks, D., 2019. Design Codes and Due Diligence for Wind Resilient Pv Trackers. PVH Webinar.

Barrero-Gil, A., Sanz-Andrés, A., 2009. Aeroelastic effects in a traffic sign panel induced by a passing vehicle. J. Wind Eng. Ind. Aerod. 97, 298–303. https://doi.org/10.1016/j.jweia.2009.07.001.

Bhaduri, S., Murphy, L.M., 1985. Wind Loading on Solar Collectors. Golden, Colorado.

Breuer, M., Jovicic, N., 2001. Separated flow around a flat plate at high incidence: an LES investigation. J. Turbul. 2 https://doi.org/10.1088/1468-5248/2/1/018.

Browne, M.T.L., Taylor, Z.J., Li, S., Gamble, S., 2020. A wind load design method for ground-mounted multi-row solar arrays based on a compilation of wind tunnel experiments. J. Wind Eng. Ind. Aerod. 205 https://doi.org/10.1016/j.jweia.2020.104294.

Bruner, J., Navarro, A., Maas, A., Reed, B., 2022. Locking solar tracker bushing. Mechanical Engineering Department, California Polytechnic State University, San Luis Obispo.

Cain, J.H., Banks, D., Peterka Petersen, C., 2015. Wind loads on utility scale solar PV power plants. In: SEAOC Convention Proceedings, pp. 1–8.

Cárdenas-Rondón, J.A., Ogueta-Gutiérrez, M., Franchini, S., Manzanares-Bercial, R., 2023. Stability analysis of two-dimensional flat solar trackers using aerodynamic derivatives at different heights above ground. J. Wind Eng. Ind. Aerod. 243 https://doi.org/10.1016/j.jweia.2023.105606.

Catalán, et al., 2020. Estrategias de defensa; estudio de inestabilidades en seguidores solares [WWW Document]. Workshop Axial. URL. https://www.youtube.com/watch?v=RmM96xI2Syw. (Accessed 12 November 2023).

Chen, F., Zhu, Y., Wang, W., Shu, Z., Li, Y., 2023. A review on aerodynamic characteristics and wind-induced response of flexible support photovoltaic system. Atmosphere. https://doi.org/10.3390/atmos14040731.

Chen, J.M., Fang, Y.-C., 1996. Strouhal numbers of inclined flat plates. Wind Eng. Indus. Aerodyn. 61, 99–112. https://doi.org/10.1016/0167-6105(96)00044-X.

Cheruku, S., Browne, M.T.L., Eng, M., Eng, P., Asce, M., 2020. Utility-scale photovoltaic power plants: analysis and design. Struct. Magaz. 32–35.

Chopra, A.K., 2012. Dynamics of Structures.

Chowdhury, J., Sauder, H., Banks, D., 2022. Effect of Solar Panel Support Structure on the Wind Loading of Horizontal Single-axis Trackers. 14th Americas Conference on Wind Engineering.

Dana, S., Young, E., 2020. Aeroelastic Modeling and Full-Scale Loads Measurements for Investigation of Single-Axis PV Tracker Wind-Driven Dynamic Instabilities. Golden, Colorado.

De la Viña, G., Cerezo, M., Argüeso Chamorro, C., Balz, M., 2021. Ensuring Tracker Stability in Extreme Weather Conditions. PV Magazine. https://www.youtube.com/watch?v=tmFH6Uc9JjY. (Accessed 12 November 2023).

Enshaei, P., Chowdhury, J., Sauder, H., Banks, D., 2023. Wind tunnel testing of torsional instability in single-Axis solar trackers: summary of methodologies and results. In: 21st Australasian Wind Engineering Society Workshop, pp. 1–6.

Franchini, S., Ogueta-Gutiérrez, M., Gómez-Ortega, O., Manzanares Bercial, R., López Núñez, E., Moralejo, A., 2019. Prediction and controlling torsional instabilities in photovoltaic solar trackers. In: The 15th International Conference on Wind Engineering, pp. 1097–1098.

Frontini, G., Calamelli, F., Muggiasca, S., Argentini, T., Belloli, M., 2022. Solar trackers analysis: a parametric study to evaluate aeroelastic effects inside a photovoltaic park array. In: 8th European-African Conference on Wind Engineering, pp. 371–374.

Gross, F., Luengo, M.R., Hennings, L., Landman, W., Balz, M., 2020. The Impact of Tracker Structure on Bifacial PV Perfomance.

He, X.H., Ding, H., Jing, H.Q., Zhang, F., Wu, X.P., Weng, X.J., 2020. Wind-induced vibration and its suppression of photovoltaic modules supported by suspension cables. J. Wind Eng. Ind. Aerod. 206 https://doi.org/10.1016/j.jweia.2020.104275.

Kaabia, B., Langlois, S., Légeron, F., 2017. Full-scale measurement of the response of a CPV tracker structure prototype under wind load. Sol. Energy 147, 368–380. https://doi.org/10.1016/j.solener.2017.03.010.

Kim, Y.C., Shan, W., Yang, Q.S., Tamura, Y., Yoshida, A., Ito, T., 2020. Effect of panel shapes on wind-induced vibrations of solar wing system under various wind environments. J. Struct. Eng. 146 (6), 04020104 https://doi.org/10.1061/(ASCE)ST.1943-541X.0002642.

Kim, Y.C., Tamura, Y., Yoshida, A., Ito, T., Shan, W., Yang, Q., 2018. Experimental investigation of aerodynamic vibrations of solar wing system. Adv. Struct. Eng. 21 (15), 2217–2226. https://doi.org/10.1177/1369433218770799.

Knisely, C.W., 1990. Strouhal number of rectangular cylinders at incidende: a review and new data. J. Fluid Struct. 4, 371–393. https://doi.org/10.1016/0889-9746(90)90137-T.

Kray, T., Markus, D., 2019. Peak wind loads on single-axis PV tracking systems. In: The 15th International Conference on Wind Engineering.

Leandro, D., Bravo, M., Judez, A., Mariñelarena, J., Falcone, F., Loayssa, A., Lopez-Amo, M., Jimenez, S., Achaerandio, A., 2020. In-field Torsion Measurements on Solar Trackers Using Fiber Optic Sensors. Pamplona.

Ma, W., Zhang, W., Zhang, X., Chen, W., Tan, Q., 2023. Experimental investigations on the wind load interference effects of single-axis solar tracker arrays. Renew. Energy 202, 566–580. https://doi.org/10.1016/j.renene.2022.11.112.

Mannini, C., Marra, A.M., Bartoli, G., 2014. VIV-galloping instability of rectangular cylinders: review and new experiments. J. Wind Eng. Ind. Aerod. 132, 109–124. https://doi.org/10.1016/j.jweia.2014.06.021.

Mannini, C., Marra, A.M., Massai, T., Bartoli, G., 2016. Interference of vortex-induced vibration and transverse galloping for a rectangular cylinder. J. Fluid Struct. 66, 403–423. https://doi.org/10.1016/j.jfluidstructs.2016.08.002.

Mariñelarena, J., Mompó, J.J., Zurita, J., Urricelqui, J., Judez, A., López-Amo, M., Jiménez, S., Achaerandio, A., Loayssa, A., 2019. Structural Health Monitoring of Solar Trackers Using Distributed Fiber Optic Sensors. SPIE-Intl Soc Optical Eng, p. 69. https://doi.org/10.1117/12.2514226.

Marra, A.M., Mannini, C., Bartoli, G., 2015. Measurements and improved model of vortex-induced vibration for an elongated rectangular cylinder. J. Wind Eng. Ind. Aerod. 147, 358–367. https://doi.org/10.1016/j.jweia.2015.08.007.

Martínez-García, E., Blanco Marigorta, E., Parrondo Gayo, J., Navarro-Manso, A., 2021a. Experimental determination of the resistance of a single axis solar tracker to torsional galloping. Struct. Eng. Mech. 78 https://doi.org/10.12989/sem.2021.78.5.000.

Martínez-García, E., Blanco-Marigorta, E., Parrondo Gayo, J., Navarro-Manso, A., 2021b. Influence of inertia and aspect ratio on the torsional galloping of single-axis solar trackers. Eng. Struct. 243 https://doi.org/10.1016/j.engstruct.2021.112682.

Mcbean, R.P., 1985. Wind load effects on flat plate solar collectors. Struct. Eng. Earthq. Eng. 111, 343–352. https://doi.org/10.1061/(ASCE)0733-9445(1985)111:2(343.

Pfahl, A., 2018. Wind Loads on Heliostats and Photovoltaic Trackers.

Pfahl, A., Buselmeier, M., Zaschke, M., 2011. Wind loads on heliostats and photovoltaic trackers of various aspect ratios. Sol. Energy 85, 2185–2201. https://doi.org/10.1016/j.solener.2011.06.006.

Pigolotti, L., Mannini, C., Bartoli, G., 2017. Destabilizing damping effect on flat-plate vibrations due to flow-induced flutter. In: Procedia Engineering. Elsevier Ltd, pp. 790–795. https://doi.org/10.1016/j.proeng.2017.09.076.

Quintela, Juan, Jurado, J.A., Rapela, C., Álvarez, A.J., Hernández, S., 2020. Inclusion of mechanical dampers in the multimodal flutter analysis of slender structures. In: WIT Transactions on Engineering Sciences. WITPress, pp. 125–135. https://doi.org/10.2495/AFM200121.

Quintela, J., Jurado, J.A., Rapela, C., Álvarez, A.J., Roca, M., Hernández, S., Cid Montoya, M., López, J.M., Ruiz, A.J., Moreno, I., Jiménez, S., 2020. Experimental and computational studies on the performance of solar trackers under vortex shedding, torsional divergence, and flutter. Int. J. Comput. Meth. Exper. Measurements 8, 387–404. https://doi.org/10.2495/CMEM-V8-N4-387-404.

Rao, S.S., 2019. Vibration of Continuous Systems. John Wiley&Sons. ed. John Wiley & Sons, Hoboken, NJ, USA.

Ricci, A., 2020. Structural Design of Mono Axial Tracker: Wind Loads and Aerodynamic Design.

Roedel, A., 2021. Extreme weather protection: how to 'weatherise' a solar installation. www.pv-tech.org53-57.

Roedel, A., Butcher, J., 2021. Mitigating extreme weather risk Part 2: surviving high-wind events and dynamic-wind effects with differentiated solar project design and control strategies. Nextracker.

Roedel, A., Upfill-Brown, S., 2018. Designing for the wind: using dynamic wind analysis and protective stow strategies to lower solar tracker lifetime costs. Nextracker.

Rohr, C., Bourke, P.A., Banks, D., 2015. Torsional instability of single-Axis solar tracking systems. In: 14th International Conference on Wind Engineering.

Roschke, E.J., 1984. Wind Loading on Solar Concentrators: Some General Considerations. DOE/JPL-1060/66 NAS 1.26:173896.

Rostami, A.B., Mobasheramini, M., Fernandes, A.C., 2019. Strouhal number of flat and flapped plates at moderate Reynolds number and different angles of attack: experimental data. Acta Mech. 230, 333–349. https://doi.org/10.1007/s00707-018-2292-2.

Scanlan, R.H., Sabzevarit, A., 1969. Experimental aerodynamic coefficients in the analytical study of suspension bridge flutter. Mech. Eng. Sci. 11, 234–242. https://doi.org/10.1243/JMES_JOUR_1969_011_031_02.

Strobel, K., Banks, D., 2014. Effects of vortex shedding in arrays of long inclined flat plates and ramifications for ground-mounted photovoltaic arrays. J. Wind Eng. Ind. Aerod. 133, 146–149. https://doi.org/10.1016/j.jweia.2014.06.013.

Taylor, Z.J., Browne, M.T.L., 2020. Hybrid pressure integration and buffeting analysis for multi-row wind loading in an array of single-axis trackers. J. Wind Eng. Ind. Aerod. 197 https://doi.org/10.1016/j.jweia.2019.104056.

Taylor, Z.J., Feero, M.A., Browne, M.T.L., 2024. Aeroelastic instability mechanisms of single-axis solar trackers. J. Wind Eng. Ind. Aerod. 244 https://doi.org/10.1016/j.jweia.2023.105626.

Valentín, D., Valero, C., Egusquiza, M., Presas, A., Egusquiza, E., 2022. Failure investigation of a solar tracker due to wind-induced torsional galloping induced torsional galloping. Eng. Fail. Anal. 135 https://doi.org/10.1016/j.engfailanal.2022.106137.

Watwe, N.H., Kartik, V., 2021. Damping of wind-induced galloping oscillations of solar trackers. In: Lecture Notes in Mechanical Engineering. Springer, pp. 511–523. https://doi.org/10.1007/978-981-15-4477-4_36.

Wittwer, A.R., Podestá, J.M., Castro, H.G., Mroginski, J.L., Marighetti, J.O., De Bortoli, M.E., Paz, R.R., Mateo, F., 2022. Wind loading and its effects on photovoltaic modules: an experimental–Computational study to assess the stress on structures. Sol. Energy 240, 315–328. https://doi.org/10.1016/j.solener.2022.04.061.

Yağci, A., Belloli, M., Fontanella, A., 2018. Wind tunnel test on full array solar PV trackers. School Indus. Infor. Eng., Politecnico di Milano.

Young, E., He, X., King, R., Corbus, D., 2020. A fluid-structure interaction solver for investigating torsional galloping in solar-tracking photovoltaic panel arrays. J. Renew. Sustain. Energy 12, 063503. https://doi.org/10.1063/5.0023757, 2020.

Zhang, X., Ma, W., Kang, X., Shao, Q., Tang, Z., 2023. Experimental study of the torsional aeroelastic instability of single-axis solar trackers under different turbulence intensities. J. Wind Eng. Ind. Aerod. 240 https://doi.org/10.1016/j.jweia.2023.105486.

Zwingmann, B., Browne, M., Osborne, M., Taylor, Z., 2020. Eliminating catastrophic PV tracker system damage due to extreme wind conditions [WWW Document]. TechTalk Webinar. URL. https://www.youtube.com/watch?v=gxnw2n7cQr4. (Accessed 12 November 2023).

4.3. Métricas del artículo

ARTÍCULO. 3

Revista	Journal of wind Engineering& Industrial Aerodynamics
Título	Experimental benchmark for the 3D wind tunnel testing of torsional aeroelastic instabilities in single-axis solar trackers
Cuartil	Q1
Factor de impacto (JCR)	4.2
Citescore (Scopus)	8.9
N° citas [julio 2024-octubre 2024]] (Web of Science)	0

Capítulo 5: Conclusiones generales

5.1. Innovaciones que aporta este trabajo de investigación.

La presente tesis recoge el desarrollo de una nueva metodología de estudio para el diseño de seguidores solares monoeje, con la finalidad de que sean resistentes a las cargas dinámicas del viento. La metodología abarca:

- Análisis las variables físicas que gobiernan el problema de inestabilidad aeroelástica
- Estudio y descripción de los fenómenos aeroelásticos
- Análisis de los parámetros estructurales de diseño óptimos para evitar la aparición de inestabilidades
- Diseño y descripción de ensayos experimentales conducentes a estudiar el fenómeno de galope torsional en seguidores solares monoeje
- Definición del diagrama de estabilidad del seguidor solar.

Esta tesis, desarrolla una nueva metodología de ensayo experimental para modelos aeroelásticos 3D, capaz de obtener las variables de diseño para estructuras solares monoeje estables. Esta nueva metodología, conforma un método específico y ampliado para el cálculo de cargas dinámicas de viento sobre estructuras solares, que no está recogida en la normativa actual. Además, es capaz de predecir el comportamiento aeroelástico de los seguidores solares monoeje ante ciertas condiciones de viento.

5.2. Fenomenología aeroelástica

Se ha encontrado una concurrencia de varios fenómenos aeroelásticos durante los ensayos, y que varían en función de la velocidad de viento incidente y la inclinación de la estructura. Vibraciones inducidas por vórtices y galope torsional.

Se han identificado vibraciones inducidas por vórtices, a velocidades de viento inferiores a los valores de velocidad crítica, para diversas inclinaciones. Esas vibraciones desaparecen al aumentar la velocidad y no parecen provocar oscilaciones de mucha amplitud.

El galope torsional, es el fenómeno primordial que causa la inestabilidad del seguidor solar y lo lleva a colapso, en la mayoría de los casos. Si el fenómeno cesa pronto y no es de mucha intensidad, los seguidores pueden no sufrir daños significativos.

Los resultados sugieren que, para que se produzca el galope torsional, deben cumplirse dos condiciones: el ángulo del seguidor solar tiene que ser adecuado para el desprendimiento de vórtices; y el flujo debe tener una cierta energía cinética mínima.

5.3. Características estructurales que influyen en un diseño resistente a la inestabilidad aeroelástica

Se ha examinado el efecto de la rigidez en modelos similares y se ha realizado un estudio analítico y experimental de la influencia de la inercia de los módulos y la relación de aspecto del seguidor.

Para determinar los rangos adecuados de estas variables, se han recopilado los valores típicos de los seguidores existentes. Actualmente, estas propiedades se agrupan en su mayoría en función de la longitud total del seguidor: Los seguidores más cortos suelen ser los que tienen coeficientes de inercia más bajos y relaciones de aspecto más bajas, y viceversa.

En cuanto al efecto de la inercia, el inicio de la inestabilidad se ha analizado a partir de la ecuación de movimiento y las fuerzas aeroelásticas. Se ha comprobado que depende principalmente del signo de la derivada aeroelástica correspondiente al amortiguamiento aerodinámico torsional. Este análisis y las pruebas realizadas en modelos a escala con diferentes inercias han comprobado que la velocidad reducida crítica mínima de galope no varía con respecto a la inercia. Asimismo, el comportamiento no estacionario durante el galope también parece estar directamente relacionado con la velocidad reducida.

A partir de esta hipótesis, se han derivado analíticamente las ecuaciones que relacionan las propiedades estructurales entre diferentes relaciones de aspecto. En cuanto a la relación de aspecto, se ha supuesto que las fuerzas aerodinámicas por unidad de longitud del seguidor se mantienen para estructuras con diferentes relaciones de aspecto, pero en diferentes coordenadas longitudinales. Las pruebas realizadas se han centrado en el rango de menor relación de aspecto (el más problemático) y se ha comprobado que, al igual que con la inercia, la velocidad crítica reducida de galope permanece constante. También se han deducido las ecuaciones de transformación de las propiedades estructurales en función de la relación de aspecto y rigidez torsional.

Se ha realizado un análisis del diseño óptimo del seguidor. Los resultados muestran que, para una determinada superficie de captación solar y dimensiones dadas del tubo de torsión, los seguidores más cortos son más estables con respecto a la inestabilidad por galope torsional, aunque las fuerzas del viento por unidad de longitud aumenten.

También se ha proporcionado una breve evaluación del efecto de la posición relativa del seguidor, comparando las ubicaciones de la mitad de la hilera con las del final de la hilera.

5.4. Creación de una nueva metodología experimental para el ensayo de modelos full-aeroelastic para el estudio de la estabilidad de seguidores solares.

Se ha desarrollado un nuevo procedimiento experimental para el estudio de la estabilidad de los seguidores solares monoeje en túnel de viento.

Una parte fundamental del procedimiento consiste en elevar la velocidad de viento sistemáticamente y poco a poco hasta que la inestabilidad torsional aparece. La velocidad a la que aparece la inestabilidad se llama Velocidad crítica. Se mapea la velocidad crítica para los distintos ángulos de inclinación del seguidor.

Las condiciones de flujo han sido: velocidad de viento uniforme, continua y frontal, con bajo nivel de turbulencia perpendicular al eje del seguidor. Esta disposición, favorece la obtención de datos fiables sobre la respuesta aerodinámica de la estructura.

Se ha creado un modelo estandarizado 3D que se espera sirva para homologar los estudios sobre aeroelasticidad de seguidores solares y proporcionar fiabilidad a los datos resultantes, superando así las limitaciones actuales de las normativas vigentes.

Este modelo reproduce la geometría y estructura básica de los seguidores comerciales típicos, con énfasis en sus características dinámicas 3D, de manera que es adecuado para estudiar fenómenos de interacción flujo-estructura en túnel de viento, como la inestabilidad torsional aeroelástica. Se han especificado las dimensiones geométricas y los detalles constructivos de este modelo canónico para que pueda reproducirse con precisión. Además, se ha presentado un análisis sobre las condiciones de similitud asociadas al comportamiento aeroelástico de los seguidores. Esto incluye la determinación de las primeras frecuencias naturales para la torsión del tubo de torsión, tanto a partir de las propiedades estructurales como experimentalmente, y los coeficientes adimensionales para la flexión del panel.

Se busca que esta metodología permita optimizar el diseño de las estructuras fotovoltaicas garantizando unas condiciones de funcionamiento seguras bajo carga de viento, reduciendo por tanto los costes de construcción y mantenimiento de las plantas solares fotovoltaicas.

5.5. Hallazgo de la velocidad crítica y diagramas de estabilidad.

En este trabajo se ha obtenido por primera vez el Diagrama de Estabilidad que determina el comportamiento de un seguidor solar de un eje frente al fenómeno de galope torsional.

La velocidad del viento a partir de la cual empiezan a desarrollarse inestabilidades aeroelásticas se ha utilizado para determinar el valor umbral de la velocidad crítica reducida.

Se ha encontrado que la velocidad crítica de galope varía para cada inclinación, y que la influencia de los principales factores estructurales, dentro de la gama actualmente en el mercado, sólo se produce a través de la velocidad reducida.

Se han realizado numeroso ensayos experimentales variando las características geométricas y dinámicas de los modelos. Estos ensayos se han utilizado para trazar un Diagrama de Estabilidad con una línea de velocidad crítica media y límites de confianza independientes para cada ángulo de inclinación, obtenidos a partir de un estándar. Este diagrama establece el criterio general de estabilidad del seguidor frente al galope torsional.

Se han analizado con detalle varias características del diagrama de estabilidad, como el ángulo de inclinación máximo y mínimo, la asimetría con respecto a la inclinación cero, los valores de velocidad crítica e inclinaciones bajas y la amplitud de vibración cuando se opera cerca de las condiciones umbral.

Se ha llevado a cabo un estudio comparativo entre los resultados experimentales obtenidos y los datos disponibles en la bibliografía de referencia (incluidos modelos seccionales y tridimensionales). Aunque la tendencia general se aprecia similar, se han observado discrepancias significativas en ciertos valores de velocidad crítica, lo que incentiva la necesidad de un método sistemático de validar las distintas metodologías de ensayo.

Referencias

Adeleke, B. (2016). Experimental and finite element analysis of wind induced displacement of a dual axis photovoltaic solar trackers (Tesis doctoral, Université d'Ottawa/University of Ottawa).

Adrián R. Wittwer, Juan M. Podestá, Hugo G. Castro, Javier L. Mroginski, Jorge O. Marighetti, Mario E. De Bortoli, Rodrigo R. Paz, Fernando Mateo. (2022). Wind loading and its effects on photovoltaic modules: An experimental–Computational study to assess the stress on structures. Solar Energy, 240, 315-328.

American Society of Civil Engineers. (2021). Wind Tunnel Testing for Buildings and Other Structures. American Society of Civil Engineers.

Armandei, M., y Fernandes, A. C. (2014). Torsional instability of an elastic flat plate due to hydrodynamic loads. Journal of Mechanics, 30(6), 643-650.

Aydogdu, M., Arda, M., y Filiz, S. (2018). Vibration of axially functionally graded nano rods and beams with a variable nonlocal parameter. Advances in nano research, 6(3), 257.

Bahrami, A., Okoye, C. O., y Atikol, U. (2017). Technical and economic assessment of fixed, single and dual-axis tracking PV panels in low latitude countries. Renewable Energy, 113, 563-579.

Banks, D. Design Codes and Due Diligence for Wind Resilient Pv Trackers (2019). PVH Webinar. URL: https://www.pv-magazine.com/wp-content/uploads/2019/08/DESIGN-CODES-AND-DUE-DILIGENCE-FOR-WIND-RESILIENT-PV-TRACKERS.pdf

Barrero-Gil, A., y Sanz-Andrés, A. (2009). Aeroelastic effects in a traffic sign panel induced by a passing vehicle. Journal of wind engineering and industrial aerodynamics, 97(5-6), 298-303.

Bhaduri, S., y Murphy, L. M. (1985). Wind loading on solar collectors (No. SERI/TR-253-2169). Solar Energy Research Inst.(SERI), Golden, CO (United States).

Blevins, R. D. (1977). Flow-induced vibration. Van Nostrand Reinhold Company Inc.

Breuer, M., y Jovicic, N. (2001). Separated flow around a flat plate at high incidence: an LES investigation. Journal of Turbulence, 2(1), 018.

Browne, M. T., Taylor, Z. J., Li, S., y Gamble, S. (2020). A wind load design method for ground-mounted multi-row solar arrays based on a compilation of wind tunnel experiments. Journal of Wind Engineering and Industrial Aerodynamics, 205, 104294.

Cain, J. H., Banks, D., y Petersen, C. P. (2015). Wind loads on utility scale solar PV power plants. International conference on wind engineering SEAOC convention proceedings. Seattle, Washington, USA

Cárdenas-Rondón, J. A., Ogueta-Gutiérrez, M., Franchini, S., y Manzanares-Bercial, R. (2023). Stability analysis of two-dimensional flat solar trackers using aerodynamic derivatives at different heights above ground. Journal of Wind Engineering and Industrial Aerodynamics, 243, 105606.

Catalán, et al. (2020). Estrategias de defensa; estudio de inestabilidades en seguidores solares. URL: https://youtu.be/RmM96xI2Syw?feature=shared

Chen, F., Zhu, Y., Wang, W., Shu, Z., y Li, Y. (2023). A Review on Aerodynamic Characteristics and Wind-Induced Response of Flexible Support Photovoltaic System. Atmosphere, 14(4), 731.

Chen, J. M., y Fang, Y. C. (1996). Strouhal numbers of inclined flat plates. Journal of wind engineering and industrial aerodynamics, 61(2-3), 99-112.

Cheruku, S. Browne, M.T.L. Eng, P. Eng, M. (2020). Utility-scale photovoltaic power plants: analysis and design Structures. Structure Magazine, pp. 32-35.

Chopra, A. K. (2007). Dynamics of structures. Pearson Education India.

Dana, S. Young, E. (27 de febrero del 2020). Aeroelastic Modeling and Full-Scale Loads Measurements for Investigation of Single-Axis PV Tracker Wind-Driven Dynamic Instabilities. NREL PV Reliability Workshop. Golden, Colorado.

Davenport, A. G. (1964). The buffeting of large superficial structures by atmospheric turbulence. Annals of the New York Academy of Sciences, 116(1), 135-160.

Dyrbye, C. and Hansen, S.O. (1997), Wind Loads on Structures, John Wiley & Sons, Ltd.

Ebrahimi, F., Barati, M. R., y Civalek, Ö. (2020). Application of Chebyshev–Ritz method for static stability and vibration analysis of nonlocal microstructure-dependent nanostructures. Engineering with Computers, 36, 953-964.

Enshaei, P., Chowdhury, J., Sauder, H., y Banks, D. (2023). Wind Tunnel Testing of Torsional Instability in Single-Axis Solar Trackers: Summary of Methodologies and Results. In AWESW2022: 21th Australasian Wind Engineering Society Workshop.

Fan, X., Wang, Z., Chen, X., Wang, Y., y Tan, W. (2020). Experimental investigation on flow-induced vibration of flexible multi cylinders in atmospheric boundary layer. International Journal of Mechanical Sciences, 183, 105815.

Franchini, S. Ogueta-Gutiérrez, M. Gómez-Ortega, O. Manzanares Bercial, R. López Núñez, E. y Moralejo, A. Prediction and controlling torsional instabilities in photovoltaic solar trackers. The 15th International Conference on Wind Engineering (2019), pp. 1097-1098.

Frontini, G., Calamelli, F., Muggiasca, S., Argentini, T., y Belloli, M. (2022). Solar trackers analysis: a case study to evaluate aeroelastic effects inside a photovoltaic park array. In 8th European-African Conference on Wind Engineering 20-23 September 2022 | Bucharest, Romania.

G. De la Viña, M. Cerezo, C. Argüeso Chamorro, M. Balz. (21 de Julio del 2021). Ensuring Tracker Stability in Extreme Weather Conditions. PV Magazine. URL: https://youtu.be/tmFH6Uc9JjY?si=_R8w8dPw9ZMgqHKL

Galuppi, L., y Royer-Carfagni, G. (2020). Enhanced Effective Thickness for laminated glass beams and plates under torsion. Engineering Structures, 206, 110077.

Gross, F., Luengo, M., Hennings, L., Landman, W., y Balz, M. (2020). The impact of tracker structure on bifacial PV performance.

Hanson, P. W. (1985). Aeroelasticity at the NASA Langley Research Center.Technical Memorandum(TM). Recent progress, new challenges (No. NASA-TM-87660).

Hao, Y., Kopp, G. A., Wu, C. H., y Gillmeier, S. (2020). A wind tunnel study of the aerodynamic characteristics of a scaled, aeroelastic, model tree. Journal of Wind Engineering and Industrial Aerodynamics, 197, 104088.

He, X. H., Ding, H., Jing, H. Q., Zhang, F., Wu, X. P., y Weng, X. J. (2020). Wind-induced vibration and its suppression of photovoltaic modules supported by suspension cables. Journal of Wind Engineering and Industrial Aerodynamics, 206, 104275.

Jia, J. (2011). Wind and structural modelling for an accurate fatigue life assessment of tubular structures. Engineering structures, 33(2), 477-491.

Johnson, F. T., Tinoco, E. N., y Yu, N. J. (2005). Thirty years of development and application of CFD at Boeing Commercial Airplanes, Seattle. Computers & Fluids, 34(10), 1115-1151.

Jubayer, C. M., y Hangan, H. (2014). Numerical simulation of wind effects on a stand-alone ground mounted photovoltaic (PV) system. Journal of Wind Engineering and Industrial Aerodynamics, 134, 56-64.

Kaabia, B., Langlois, S., y Légeron, F. (2017). Full-scale measurement of the response of a CPV tracker structure prototype under wind load. Solar Energy, 147, 368-380.

Katariya, P. V. (2019). Numerical frequency analysis of skew sandwich layered composite shell structures under thermal environment including shear deformation effects. Structural Engineering and Mechanics, An Int'l Journal, 71(6), 657-668.

Kim, Y. C., Shan, W., Yang, Q. S., Tamura, Y., Yoshida, A., e Ito, T. (2020). Effect of panel shapes on wind-induced vibrations of solar wing system under various wind environments. Journal of Structural Engineering, 146(6), 04020104.

Kim, Y. C., Tamura, Y., Yoshida, A., Ito, T., Shan, W., y Yang, Q. (2018). Experimental investigation of aerodynamic vibrations of solar wing system. Advances in Structural Engineering, 21(15), 2217-2226.

Knisely, C. W. (1990). Strouhal numbers of rectangular cylinders at incidence: a review and new data. Journal of fluids and structures, 4(4), 371-393.

Kopp, G. A., Farquhar, S., y Morrison, M. J. (2012). Aerodynamic mechanisms for wind loads on tilted, roof-mounted, solar arrays. Journal of Wind Engineering and Industrial Aerodynamics, 111, 40-52.

Koussa, M., Cheknane, A., Hadji, S. M. H. S. N., Haddadi, M., y Noureddine, S. (2011). Measured and modelled improvement in solar energy yield from flat plate photovoltaic systems utilizing different tracking systems and under a range of environmental conditions. Applied Energy, 88(5), 1756-1771.

Kray, T., y Markus, D. (2019, September). Peak wind loads on single-axis PV tracking systems. In Proceedings of the 15th International Conference on Wind Engineering, Beijing, China.

Lastra, M. R., Oro, J. M. F., Vega, M. G., Marigorta, E. B., y Morros, C. S. (2013). Novel design and experimental validation of a contraction nozzle for aerodynamic measurements in a subsonic wind tunnel. Journal of Wind Engineering and Industrial Aerodynamics, 118, 35-43.

Lave, M., & Kleissl, J. (2011). Optimum fixed orientations and benefits of tracking for capturing solar radiation in the continental United States. Renewable Energy, 36(3), 1145-1152.

Lazard. (2018). Lazard’s Levelized Cost of Energy Analysis – Version 12.0. Lazard, New York, USA; URL: https://www.lazard.com/media/0hqfye2m/lazards-levelized-cost-of-energy-version-120-vfinal.pdf

Leandro, D., Bravo, M., Judez, A., Mariñelarena, J., Falcone, F., Loayssa, A., y Jimenez, S. (2020, June). In-field Torsion Measurements on Solar Trackers Using Fiber Optic Sensors. In Optical Fiber Sensors (pp. 4-35). Optica Publishing Group.

León Alonso, A. Jurado, José A. Hernández, Santiago. Nieto, Félix. Comparación de diversas funciones indiciales para la resolución del flameo de una placa plana en el dominio del tiempo. Conference paper: CMNE/CILAMCE (2007).

Ma, W., Zhang, W., Zhang, X., Chen, W., y Tan, Q. (2023). Experimental investigations on the wind load interference effects of single-axis solar tracker arrays. Renewable Energy, 202, 566-580.

Mannini, C., Marra, A. M., y Bartoli, G. (2014). VIV–galloping instability of rectangular cylinders: Review and new experiments. Journal of wind engineering and industrial aerodynamics, 132, 109-124.

Mannini, C., Marra, A. M., Massai, T., y Bartoli, G. (2016). Interference of vortex-induced vibration and transverse galloping for a rectangular cylinder. Journal of Fluids and Structures, 66, 403-423.

Mariñelarena, J., Mompó, J. J., Zurita, J., Urricelqui, J., Judez, A., Amo, M. L., y Loayssa, A. (2019, March). Structural health monitoring of solar trackers using distributed fiber optic sensors. In Sensors and Smart Structures Technologies for Civil, Mechanical, and Aerospace Systems 2019 (Vol. 10970, pp. 565-574). SPIE.

Marra, A. M., Mannini, C., y Bartoli, G. (2015). Measurements and improved model of vortex-induced vibration for an elongated rectangular cylinder. Journal of Wind Engineering and Industrial Aerodynamics, 147, 358-367.

Martínez García, E., Blanco Marigorta, E., Parrondo Gayo, J. L., y Navarro Manso, A. (2021). (a). Experimental determination of the resistance of a single-axis solar tracker to torsional galloping. Structural Engineering and Mechanics. Volume 78, Number 5, June10 2021, pages 519-528.

Martínez-García, E., Blanco-Marigorta, E., Gayo, J. P., y Navarro-Manso, A. (2021). (b). Influence of inertia and aspect ratio on the torsional galloping of single-axis solar trackers. Engineering Structures, 243, 112682.

Masson, G., & Kaizuka, I. (2019). Trends in Photovoltaic Applications (IEA) International Energy Agency. Report IEA PVPS T1:36:2019. Photovoltaic Power Systems Technology Collaboration Programe. URL: https://iea-pvps.org/wp-content/uploads/2020/02/5319-iea-pvps-report-2019-08-lr.pdf

McBean, R. P. (1985). Wind load effects on flat plate solar collectors. Journal of Structural Engineering, 111(2), 343-352.

Miller, R. D., & Zimmerman, D. K. (1981). Wind loads on flat plate photovoltaic array fields (nonsteady winds). Contractor Report (CR) (No. NASA-CR-164745).

Mohammadnejad, M. (2015). A new analytical approach for determination of flexural, axial and torsional natural frequencies of beams. Structural engineering and mechanics, 55(3), 655-674.

Païdoussis, M. P., Price, S. J., y De Langre, E. (2010). Fluid-structure interactions: cross-flow-induced instabilities. Cambridge University Press.

Pfahl, A. (2018). Wind loads on heliostats and photovoltaic trackers (Tesis doctoral).

Ricci, S., Marchetti, L., Riccobene, L., De Gaspari, A., Toffol, F., Fonte, F., y Livne, E. (2021). An active flutter suppression (AFS) project: Overview, results and lessons learned. In AIAA Scitech 2021 Forum (p. 0908).

Pfahl, A., Buselmeier, M., y Zaschke, M. (2011). Wind loads on heliostats and photovoltaic trackers of various aspect ratios. Solar Energy, 85(9), 2185-2201.

Pickerel, K. (2018). How the solar industry is responding to the increasing intensity of natural disasters. Solar Power World. URL: https://www.solarpowerworldonline.com/2018/01/solar-industry-responding-increasing-intensity-natural-disasters/

Pigolotti, L., Mannini, C., y Bartoli, G. (2017). Destabilizing damping effect on flat-plate vibrations due to flow-induced flutter. Procedia engineering, 199, 790-795.

Quintela, J., Jurado, J. A., Rapela, C., Álvarez, A. J., yHernández, S. (2020). Inclusion of Mechanical Dampers in the Multimodal Flutter Analysis of Slender Structures. Advances in Fluid Mechanics, 13, 125.

Quintela, J., Jurado, J. A., Rapela, C., Álvarez, A. J., Roca, M., Hernández, S., y Jiménez, S. (2020). Experimental and computational studies on the performance of solar trackers under vortex shedding, torsional divergence, and flutter. International Journal of Computational Methods and Experimental Measurements, 8(4), 387-404.

Rao, S.S. (2019). Vibration of Continuous Systems. John Wiley&Sons. ed. John Wiley &Sons, Hoboken, NJ, USA.

Rodríguez-Casado, C., Martínez-García, E., Manzanares-Bercial, R., Ruiz-Moral, J. L., Blanco-Marigorta, E., y Navarro-Manso, A. (2024). Experimental Benchmark for the 3D wind tunnel testing of torsional aeroelastic instabilities in single-axis solar trackers. Journal of Wind Engineering and Industrial Aerodynamics, 253, 105838.

Roedel, A. (Mayo del 2021). Extreme weather protection: how to 'weatherise' a solar installation.URL:https://f.hubspotusercontent40.net/hubfs/1856748/Extreme%20weather%20protection%20FINAL.pdf

Roedel, A. Butcher, J. (2021). Mitigating extreme weather risk Part 2: surviving high-wind events and dynamic-wind effects with differentiated solar project design and control strategies. Nextracker whitepaper. URL: https://info.nextracker.com/mitigating-extreme-weather-risk-part-2

Roedel, A., y Uphill-Brown, S. (2018). Designing for the Wind. White Paper, NEXTracker Corporation.

Rohr, C., Bourke, P. A., y Banks, D. (2015, June). Torsional instability of single-axis solar tracking systems. In Proceedings of the 14th international conference on wind engineering, Porto Alegre (pp. 21-26).

Roschke, E. J. (1984). Wind loading on solar concentrators: some general considerations. NASA. Technical Report N° JPL-PUB-83-101.

Rostami, A. B., Mobasheramini, M., y Fernandes, A. C. (2019). Strouhal number of flat and flapped plates at moderate Reynolds number and different angles of attack: experimental data. Acta Mechanica, 230, 333-349.

Scanlan, R. H., y Sabzevari, A. (1969). Experimental aerodynamic coefficients in the analytical study of suspension bridge flutter. Journal of Mechanical Engineering Science, 11(3), 234-242.

Scanlan, R. H., y Tomko, J. J. (1971). Airfoil and bridge deck flutter derivatives. Journal of the engineering mechanics division, 97(6), 1717-1737.

Seo, D. W., y Caracoglia, L. (2011). Estimation of torsional-flutter probability in flexible bridges considering randomness in flutter derivatives. Engineering structures, 33(8), 2284-2296.

Simiu, E., y Scanlan, R. H. (1996). Wind effects on structures: fundamentals and applications to design. New York: John Wiley.

Stathopoulos, T., Zisis, I., y Xypnitou, E. (2014). Local and overall wind pressure and force coefficients for solar panels. Journal of wind engineering and industrial aerodynamics, 125, 195-206.

Strobel, K., y Banks, D. (2014). Effects of vortex shedding in arrays of long inclined flat plates and ramifications for ground-mounted photovoltaic arrays. Journal of Wind Engineering and Industrial Aerodynamics, 133, 146-149.

Talavera, D. L., Muñoz-Cerón, E., Ferrer-Rodríguez, J. P., y Pérez-Higueras, P. J. (2019). Assessment of cost-competitiveness and profitability of fixed and tracking photovoltaic systems: The case of five specific sites. Renewable Energy, 134, 902-913.

Taylor, Z. J.,y Browne, M. T. (2020). Hybrid pressure integration and buffeting analysis for multi-row wind loading in an array of single-axis trackers. Journal of Wind Engineering and Industrial Aerodynamics, 197, 104056.

Taylor, Z. J., Feero, M. A., y Browne, M. T. (2024). Aeroelastic instability mechanisms of single-axis solar trackers. Journal of Wind Engineering and Industrial Aerodynamics, 244, 105626.

Terrés Nicoli, J. M. (2008). Different mechanisms of vortex induced vibration of bridges.Tesis doctoral. Universidad de Granada.

Timoshenko, S. Gere, J.M. (1963). Theory of elastic stability. Mc-Graw Hill, New York

US Energy Information Administration. (2022). Levelized avoided cost of new generation resources in the annual energy outlook 2022. URL: https://www.eia.gov/outlooks/aeo/electricity_generation.php

Valentín, D., Valero, C., Egusquiza, M., y Presas, A. (2022). Failure investigation of a solar tracker due to wind-induced torsional galloping. Engineering Failure Analysis, 135, 106137.

Wardlaw, R. L. (1994). Flutter and torsional instability. Wind-excited vibrations of structures (pp. 293-319). H.Sockel Technical University.

Watwe, N. H., y Kartik, V. (2021). Damping of Wind-Induced Galloping Oscillations of Solar Trackers. In Mechanism and Machine Science: Select Proceedings of Asian MMS 2018 (pp. 511-523). Springer Singapore.

Wesoff E. 2020.Solar Trackers in Wind and the Terror of Torsional Gallopoing. PV Magazine USA. January 17th. https://pv-magazine-usa.com/2020/01/17/dan-shugar-nextracker-ceo-on-solar-trackers-in-wind-and-the-terror-of-torsional-galloping/

Willuhn M. 2019. Tracking in the wind. PV Magazine Australia, September 7th. https://www.pv-magazine-australia.com/2019/09/07/long-read-pt-1-tracking-in-the-wind/

Wood Mackenzie, (2022), https://www.woodmac.com/market-insights/power-and-renewables/

Yagci, A. (2018). Wind tunnel test on full array solar PV trackers.Trabajo fin de master. Instituto Politécnico de Milano.

Yang, Y. (2012). *Experimental investigations of vortex induced vibration of a flat plate in pitch oscillation* (Doctoral dissertation, Texas A & M University). URL: https://oaktrust.library.tamu.edu/server/api/core/bitstreams/6d7244fb-3c5d-482a-94d7-6714a096d46c/content

Young, E., He, X., King, R., y Corbus, D. (2020). A fluid-structure interaction solver for investigating torsional galloping in solar-tracking photovoltaic panel arrays. Journal of Renewable and Sustainable Energy, 12(6).

Zhang, X., Ma, W., Kang, X., Shao, Q., y Tang, Z. (2023). Experimental study of the torsional aeroelastic instability of single-axis solar trackers under different turbulence intensities. Journal of Wind Engineering and Industrial Aerodynamics, 240, 105486.

Zwingmann, B. Browne, M. Osborne, M. Taylor, Z. (2020). Eliminating catastrophic PV tracker system damage due to extreme wind conditions. URL: https://youtu.be/gxnw2n7cQr4?feature=shared . Accessed 12th Nov 2023.

Anexo. Comunicaciones en congresos relacionadas con la tesis

En este apartado se recogen varias comunicaciones hechas en congresos internacionales, relacionadas con la construcción de túnel aerodinámico para realización de ensayos y sobre los estudios aeroelásticos en los que se basa esta tesis.

Recoge 3 artículos de dos congresos internacionales diferentes:

- Congreso internacional de estructuras de la asociación española de ingeniería estructural
- 12th international conference on flow-induced vibration

1. Congreso internacional de estructuras de la asociación española de ingeniería estructural

Diseño y construcción de un nuevo túnel Aerodinámico de capa límite

HORMIGÓN y ACERO

REVISTA CUATRIMESTRAL DE ACHE ASOCIACIÓN ESPAÑOLA DE INGENIERÍA ESTRUCTURAL

Mayo 2022 | Volumen 73 - Especial Congreso

Cartel ganador del concurso de carteles para el VIII Congreso de ACHE

Disponible en www.hormigonyacero.com
Volumen 73, Especial VIII Congreso ACHE, Junio 2022
https://doi.org/10.33586/hya.2022.SANTANDER

Volumen 73 - Especial Congreso, Junio 2022

SUMARIO | CONTENTS

VIII Congreso Internacional de Estructuras

Congreso de la Asociación Española de Ingeniería Estructural (ACHE)
Santander, 20-22 de junio de 2022

E.T.S.I. de Caminos, Canales y Puertos. Laboratorio de Estructuras. Avda. del Profesor Aranguren, s/n. 28040 Madrid
Tel.: (+34) 91 067 41 64 - www.e-ache.com

DISEÑO Y CONSTRUCCIÓN DE UN NUEVO TÚNEL AERODINÁMICO DE CAPA LÍMITE

Autor 1: **Antonio NAVARRO MANSO**
Dr. Ingeniero de Caminos, Canales y Puertos
Área de Ing. Hidráulica, Universidad de Oviedo
Profesor Ayudante Doctor
navarroantonio@uniovi.es

Autor 2: **Ricardo UCHE GARCÍA**
Graduado en Ingeniería Civil
Área de Ing. Hidráulica, Universidad de Oviedo
Estudiante Máster de I.C.C.P.
uo232541@uniovi.es

Autor 3: **Nicolás VALLINA PITA**
Graduado en Ingeniería Civil
Área de Ing. Hidráulica, Universidad de Oviedo
Estudiante Máster de I.C.C.P.
uo231036@uniovi.es

Autor 4: **Eduardo ÁLVAREZ ÁLVAREZ**
Dr. Ingeniero Industrial
Área de Ing. Hidráulica, Universidad de Oviedo
Profesor Ayudante Doctor
edualvarez@uniovi.es

Autor 5: **Rodolfo ESPINA VALDÉS**
Ingeniero de Caminos, Canales y Puertos
Área de Ing. Hidráulica, Universidad de Oviedo
Profesor Asociado
espinarodolfo@uniovi.es

Autor 6: **Eva MARTÍNEZ GARCÍA**
Graduada en Ing. Rec. Energéticos y Mineros
Universidad de Oviedo
Estudiante Máster de I.C.C.P.
uo267991@uniovi.es

RESUMEN

El Área de Ingeniería Hidráulica del Departamento de Energía de la Universidad de Oviedo ha impulsado la construcción de un túnel aerodinámico en la Escuela Politécnica de Mieres.

Existen muchas situaciones en las que el proceso de diseño de una estructura en Ingeniería Civil, aplicando las normas de cálculo de las acciones de viento, no se pueden predecir con la precisión necesaria las cargas aerodinámicas sobre la misma. En tales circunstancias de incertidumbre, el proceso de diseño deberá avanzar bien asumiendo los riesgos que supone el desconocimiento de las cargas del viento, bien aplicando factores de seguridad exagerados que den lugar a un diseño en extremo conservador (y, casi con toda seguridad, más caro); o bien intentando determinar con más precisión las cargas aerodinámicas, para lo que habrá que acudir, normalmente, a ensayos con modelos a escala en túneles aerodinámicos.

Así pues, en consonancia con todo lo anterior se puede decir que la finalidad de los ensayos en túnel aerodinámico de modelo a escala reducida de construcciones es suministrar a los ingenieros información sobre las particularidades del viento en las proximidades del cuerpo en consideración, sobre la distribución de presiones, y sobre las cargas globales producidas por el viento en el objeto de interés y, si fuera el caso, su respuesta aeroelástica.

El objetivo del presente artículo es describir el proceso de diseño y construcción de esta infraestructura, de grandes prestaciones, y que supera a los otros cuatro túneles aerodinámicos de los que ya disponemos en nuestra Universidad. Un aspecto innovador y enriquecedor es la participación de los propios alumnos en la ejecución del túnel, lo que les facilita un extraordinario complemento práctico a la asignatura Ingeneiría del Viento, que se imparte en nuestro Máster de Ingeniería de Caminos Canales y Puertos.

El túnel aerodinámico que se ha diseñado para nuestra Escuela Politécnica está orientado tanto a la enseñanza como a la investigación; es de configuración cerrada, consiguiéndose una mejor estabilidad del flujo y mayores velocidades que si fuese de configuración abierta. La extensión del túnel aerodinámico cerrado comprende un anillo de 31,1 m. de longitud, con una sección de ensayo de 2,25 m^2. Asimismo, a continuación de la cámara de remanso, posee un tramo de entrada con tobera de 1,5 m. que conecta con la cámara de ensayo.

Está tiene una longitud de 10 m., permitiendo realizar ensayos a diferentes distancias de la tobera de entrada, en función de la uniformidad del perfil o el desarrollo de la capa límite (BL boundary layer, capa límite terrestre) que se desee obtener. Un ventilador colocado a la mitad del circuito permite alcanzar unas velocidades de entorno 40-50 m/s.

PALABRAS CLAVE: Wind Tunnel, Computational Fluid Dynamics, Wood structures, Construction

1. Introducción y objeto

Este artículo tiene como finalidad presentar el proyecto de diseño y construcción de un túnel aerodinámico de capa límite en la Escuela Politécnica de Mieres (EPM), en la Universidad de Oviedo, llevado a cabo por el Área de Ingeniería Hidráulica y el Área de Mecánica de Fluidos del Departamento de Energía. La construcción se está realizando por parte de profesores y alumnos del Grado de Ingeniería Civil y el Máster de Ingeniería de Caminos, Canales y Puertos.

El objetivo buscado con su construcción es el desarrollo de investigación básica y el desarrollo de prácticas para los alumnos, enfocadas al estudio de la interacción del viento con estructuras civiles: puentes, edificios, aerogeneradores, paneles, cubiertas, etc.

Es bien sabido que en muchas ocasiones las normas técnicas menosprecian en demasía los efectos del viento, y en muchas ocasiones estas cargas de naturaleza dinámica son las responsables del dimensionamiento de puentes muy expuestos y flexibles, edificios singulares, cubiertas, fachadas, etc. Es también frecuente por parte de la normativa el sobredimensionamiento de ciertos efectos aerodinámicos. Es por ello, que con la finalidad de estudiar estos efectos sobre las estructuras, en modelos reales o a escala, los túneles aerodinámicos se han desarrollado como herramienta fundamental del proceso de diseño de esas construcciones.

Los inventores de las primeras máquinas voladoras, fueron también los pioneros en la construcción de los primitivos túneles aerodinámicos. En un momento determinado fueron conscientes de que necesitaban comprender la física del problema al que se enfrentaban y con ello construyeron instrumentos para ensayar sus modelos. Las primeras medidas de las fuerzas aerodinámicas, llevadas a cabo en el siglo XVII, se basaban en un aparato llamado “whirling arm” (brazo giratorio), el cual hacia girar el objeto del ensayo alrededor de un eje, es decir, era el modelo el que se movía mientras el aire se mantenía estático. Este ingenio generaba demasiada turbulencia debido al brazo de conexión, y por tanto, resultaba muy difícil determinar la verdadera velocidad entre el modelo y el aire. Hoy en día, mejorando ese marco relativo, el paradigma se basa en que el modelo permanezca estacionario mientras se acelera un flujo de aire alrededor del mismo.

Los túneles de viento pueden ser de diferentes tipos: aeronáuticos, de baja turbulencia, de humo, automovilísticos, climáticos, de capa límite, etc.; y además, estos pueden presentar distintas configuraciones, tanto abierto como cerrado. Sin embargo, todos ellos presentan un elemento en común: un potente ventilador (o matriz de ventiladores) que se encarga de aspirar o impulsar el aire a través del sistema de conductos. Con todo ello, se emplean diferentes técnicas e instrumentos de medición para auscultar el modelo ensayado, buscando conocer velocidades, distribución de presiones, fuerzas aerodinámicas y otras variables del flujo.

El empleo de modelos a escala requiere a su vez el uso de las leyes de semejanza, con la finalidad de poder traducir los resultados experimentales a las condiciones reales. Los requisitos para poder extrapolar los resultados experimentales al prototipo se basan en el cumplimiento de la semejanza geométrica, cinemática y dinámica. Dado que en general es imposible cumplir con todos los parámetros que intervienen en el fenómeno que se está estudiando, en la práctica basta con asegurar que ciertos números adimensionales se encuentran dentro de un rango definido, en función de las características del problema.

Los ensayos experimentales llevados a cabo en túneles aerodinámicos son además fundamentales para validar las técnicas de simulación numérica. Sin estas pruebas, los modelos de volúmenes finitos no podrían contrastar sus resultados. Cabe recordar que los ensayos experimentales son los que realmente reflejan la realidad presentada en la interacción del objeto con el viento.

2. Diseño

El diseño general del túnel de viento propuesto se muestra en la Figura 1. El flujo de aire circula en el sentido contrario a las agujas del reloj. Aguas arriba de la cámara de ensayo encontramos los dos componentes principales del túnel de viento: la contracción y la cámara de remanso. El otro componente crucial es, por supuesto, la fuente de potencia. El resto de componentes solo sirven para cerrar el circuito y minimizar la pérdida de energía. Sin embargo, el difusor 2 y el diseño de la curva contigua también tienen una influencia importante en la calidad del flujo y son responsables de más del 50% de las pérdidas totales.

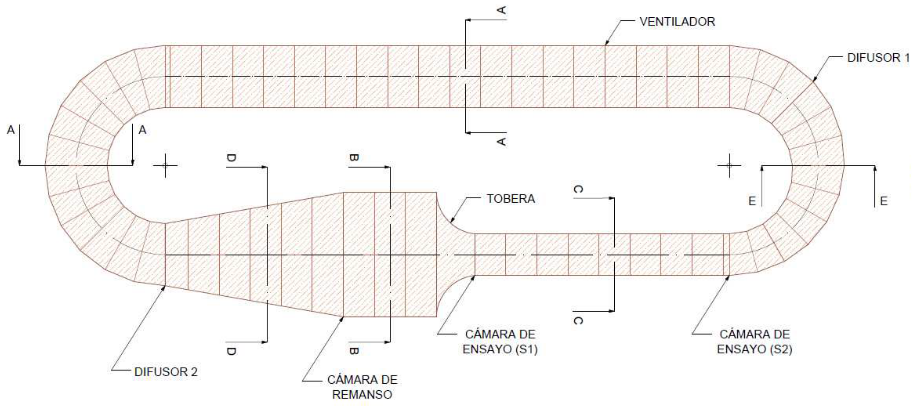

Figura 1. Planta del túnel aerodinámico de la EPM.

A continuación, se describen los componentes principales del túnel aerodinámico y los parámetros de diseño que se han elegido.

2.1. Cámara de ensayo

El tamaño de la cámara de prueba debe definirse de acuerdo con las especificaciones principales del túnel aerodinámico, que también incluyen la velocidad de operación y la calidad de flujo deseada. El tamaño de la cámara de prueba y la velocidad de operación determinan el tamaño máximo de los modelos y el número máximo alcanzable de Reynolds.

La forma de la sección transversal depende de las aplicaciones. En el caso de aplicaciones civiles o industriales, en la mayoría de los casos, se recomienda una sección transversal cuadrada o rectangular. En este caso, las muestras de prueba generalmente son cuerpos romos y su área frontal equivalente no debe ser superior al 10% del área de la sección transversal de la cámara de prueba para evitar la necesidad de realizar correcciones de bloqueo no lineales.

El túnel aerodinámico de la EPM tiene una cámara de ensayo de 1,5 m. x 1,5 m. y una longitud de 10 m., lo que permite realizar ensayos de capa límite terrestre (ABL,"Atmospheric Boundary Layer").

Se ha especificado como velocidad nominal a la entrada de la cámara de ensayo un valor de 50 m/s., lo cual garantiza poder de prueba con números de Reynolds superiores a 10^5.

Por tanto, el caudal que debe circular por el túnel se muestra en la siguiente expresión (1):

$$\mathrm{Q} = \mathrm{V} \cdot \mathrm{S} = 50\,\frac{\mathrm{m}}{\mathrm{s}} \cdot 1{,}5\ \mathrm{m} \cdot 1{,}5\ \mathrm{m} = 112{,}5\ \frac{\mathrm{m}^3}{\mathrm{s}} \qquad (1)$$

2.2. Contracción

La contracción o tobera puede ser la parte más crítica en el diseño de un túnel de viento; tiene el mayor impacto en la calidad de flujo de la cámara de ensayo. Su objetivo es acelerar el flujo desde la cámara de remanso a la cámara de ensayo, reduciendo aún más la turbulencia del flujo y las irregularidades en la cámara experimental. Las atenuaciones de aceleración de flujo y no uniformidad dependen principalmente de la llamada relación de contracción, N, entre las áreas de sección de entrada y salida. Aunque, debido a la mejora de la calidad del flujo, la relación de contracción, N, debe ser lo más grande posible, este parámetro influye fuertemente en las dimensiones generales del túnel de viento. Por lo tanto, dependiendo de las aplicaciones esperadas, se debe alcanzar un equilibrio para este parámetro.

En nuestro caso, la principal restricción para la cámara de remanso era el espacio disponible. Se ha construido una cámara de 4,74 m. x 3,78 m. y 3,76 m. de largo, lo cual implica una N (2) de:

$$\mathrm{N} = \frac{A_S}{A_t} = \frac{4{,}74\ m \cdot 3{,}78\ m}{1{,}5\ m \cdot 1{,}5\ m} = 7{,}1 \qquad (2)$$

Para el diseño de la contracción se ha elegido una curva logarítmica (Figura 2). Esta curva tiene un funcionamiento bueno y resuelve los problemas de falta de espacio (ya que puede ser más corta que las contracciones clásicas con dos curvas) e implica una mayor facilidad constructiva. Para minimizer el posible vórtice que se pueda producir en el ángulo de encuentro entre la cámara de remanso y la contración se ha rematado el encuentro con un chaflán a 45º. La longitud de está contracción es de 1,5 m.

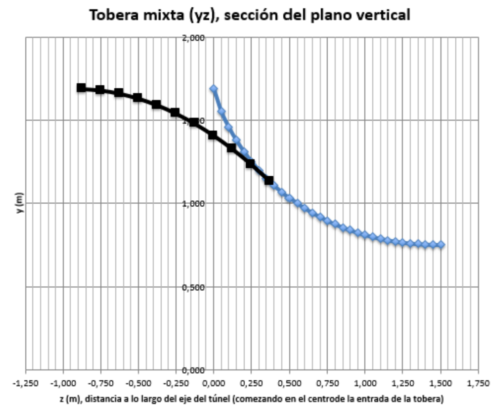

(REFERENCIA, GRÁFICAS Y ECUACIONES).

2.3. Cámara de remanso y difusor 2

Once the flow exits the fan (better if a fixed straightener are placed downstream), the diffuser drives the flow and the uniformization process starts in the settling chamber. Here the flow increases the pressure by reducing his speed. It is a simple constant section duct, which connects the exit of the diffuser with the entrance of the contraction. The diffuser (a low angle is required) should guarantee a smooth developing of the flow, avoiding the separation of the boundary layer on their walls.

Para el primer difusor, que une la sección de salida del ventilador con la cámara de remanso, se ha optado por diseñar un difusor recto después de la primera curva cuyo parámetro crítico es el ángulo. La longitud del difusor es de 7 m y el ángulo finalmente obtenido es de 13º. El valor de este ángulo así como la existencia de la primera curva hacen preveer posibles separaciones y distribuciones no uniformes de flujo, por lo que habrá que instalar algún tipo de enderezador.

Nevertheless, when a high quality flow is required, some devices can be installed to increase the flow uniformity and to reduce the turbulence level at the entrance of the nozzle. The most commonly used devices are honeycombs and screens. The former reduces drastically the lateral turbulence and does not introduce great pressure loss; the screens instead are very efficient at reducing the longitudinal turbulence and imply a relatively high losses.

El honeycomb está hecho a mano y tiene una porosidad aproximada del 83,7 %, un tamaño de celda de 3,5 cm y una longitud de 25 cm. Una vez realizadas las primeras pruebas se instalará al menos una screen.

2.4. Ventilador

According to our experience, for an closed circuit wind tunnel, eventually including settling chamber screens or/and honeycomb, the power plant should provide above 100% of the dynamic pressure in the test chamber, apart the efficiency of the motor.

Esto significa que:

$$\Delta \mathrm{P} = \frac{1}{2} \cdot \rho \cdot {U_0}^2 = \frac{1}{2} \cdot 1{,}2 \frac{kg}{m^3} \cdot \left(50 \frac{m}{s}\right)^2 = 1.500\ Pa$$

$$\mathrm{Pot} = \mathrm{Q} \cdot \Delta \mathrm{P} = 112{,}5\ \frac{\mathrm{m}^3}{\mathrm{s}} \cdot 1500\ Pa = 168.750\ W$$

Para proporcionar el salto de presión y el caudal requeridos para la velocidad de diseño e han contemplado dos alternativas:

- Un único ventilador de aproximadamente 3 m de diámetro y con una potencia de 200 kW.
- Cuatro ventiladores de 1,3 m de diámetro y 45 kW cada uno dispuestos en una matriz de 2x2.

Finalmente, tanto por motivos económicos como por el espacio disponible se han instalado los cuatro ventiladores.

(CURVA VENTILADORES Y PLANO)

2.5. Difusor 1

El último elemento que cierra el circuito es un difusor en curva que une la salida de la cámara de ensayo con la sección de los ventiladores. Se ha decidido situar el difusor dentro de la propia curva para comenzar a disminuir cuanto antes la velocidad del flujo y por las condiciones geométricas del lugar.

Al igual que sucedía en el difusor 1 será necesario la construcción de algún enderezador como veremos en el capítulo posterior de cálculo numérico.

Con el objeto de presentar el proyecto a distintos organismos oficiales que puedan colaborar con la financiación del túnel se ha realizado una maqueta del túnel mediante impresión 3D (Figura X). Esta maqueta también es empleada para la docencia de esta materia en la Escuela, permitiendo a los alumnos una comprensión rápida e intuitiva de la instalación.

3. Fluent

3.1. Calibración del modelo CFD

Se presenta a continuación el modelo CFD realizado específicamente para afinar el diseño del túnel. Este modelo debe de reproducir de la forma más exacta los distintos elementos del túnel aerodinámico descritos anteriormente.

Se ha modelizado el túnel a escala 1:1, con un tamaño de elemento de XXX, lo que permite realizar un número de casos elevado con un coste computacional razonable. El número de elementos (volúmenes finitos) empleado está en el orden de los XXX; y el tiempo de cálculo de cada uno de los casos es de unos XXX s.

Se simula el aire atmosférico como un gas a 25°C, con sus propiedades de viscosidad dinámica, densidad, etc., constantes, comportamiento adiabático e incompresible.

- Descripción del material = Aire a 25 °C y 1 atm (seco).
- Densidad ρ= 1,185 [kg m^{-3}]. (en los modelos de comparación, se actualiza al valor real en túnel, aproximadamente 1,2 [kg m^{-3}]).
- Masa molar = 28,96 [kg·$kmol^{-1}$].
- Viscosidad dinámica = 1,831E-05 [kg·m^{-1}·s^{-1}].

La simulación se realiza en estado estacionario y régimen subsónico.

Se ha optado por utilizar una malla no estructurada, fundamentalmente porque garantiza la convergencia de la solución en una gran mayoría de condiciones iniciales y de contorno para el problema planteado. Se ha realizado un estudio de sensibilidad del mallado encontrando que los valores de las variables fundamentales del problema son independientes del número de elementos del modelo a partir del millón de elementos. Actualmente los alumnos están desarrollando varios Trabajos Fin de Máster en los que se analiza entre otras cosas la posibilidad de realizar refinamientos en algunas zonas del túnel.

El modelo de turbulencia adoptado ha sido el k- ε. Los errores residuales máximos (RMS) se han limitado a un valor de 10^{-5}.

Las condiciones de contorno son las siguientes:

- Fan: la condición de contorno correspondiente al ventilador se introduce aproximando la curva de la máquina a dos tramos rectos que se cortan en el punto óptimo de funcionamiento. Para facilitar la convergencia final de la solución, se realiza una inicialización estándar de todo el dominio. Se comprueba que la influencia del modo de introducir esta condición de contorno tiene poca influencia para el análisis que aquí se pretende.
- Paredes: se imponen como condición de muro, siendo por tanto la velocidad nula. El valor de la rugosidad tiene poca influencia debido a que estamos en un flujo turbulento completamente desarrollado.

Las Figuras muestran los resultados obtenidos en la simulación para la inclinación de 45º y velocidad de viento de 50 m/s.

Finalmente, se recogen las comparaciones entre los valores experimentales recogidos en la práctica y los valores de las simulaciones para la fuerza axial y el coeficiente de arrastre, según la expresión (1):

$$Cd = \frac{Faxial}{\frac{1}{2} \cdot V^2 \cdot A \cdot \rho} \qquad (1)$$

4. Conclusiones

This wind tunnel is normally used for teaching purposes, although some research projects and students competitions could be done there as well. When using for research the choice of an appropriate measurement equipment (force balance, Pitot tube, hot wire anemometers, and scanner pressure), is therefore crucial in obtaining reliable and accurate measurements (Fig. 4).

In the case of the so called Civil Aerodynamics or even educational applications in any field, the requirements related to flow quality may be relaxed, in comparison to aeronautical ones. Although relaxed does not mean ignored.

The main specifications for a wind tunnel are the dimensions of the test section and the desired maximum operating speed. Together with this the flow quality, in terms of turbulence level and flow uniformity, must be specified in accordance with the applications.

Flow quality, which is one of the main characteristics, is a result of the whole final design, and can only be verified during calibration tests. However, according to previous empirical knowledge, some rules can be followed to select adequate values of the variables that affect the associated quality parameters.

Aerodynamic forces (drag, lift and moment coefficients as well as their oscillations) (Fig. 5 a, b & c), pressure distribution along the faces of the object and the velocity field around it can be “exactly” determined, taking into account the proper similarity laws: geometric, kinematic and dynamic. Some aeroelastic phenomena can be also analysed, as Vortex Induced Vibration (VIV) (Fig. 6).

So the design of the wind tunnels depends mainly on their final purpose. Thus two types of velocity profiles can be reproduced: the first one, the uniform profile we have talked about; however in engineering&architecture constructions, due to the fact that buildings are placed on the ground and are usually of relatively low height, they are well within the Atmospheric Boundary Layer (ABL), a longer and closed test chamber could be implemented in order to simulate of the equivalent boundary layer, in terms of average speed and turbulence level. This becomes a more challenging problem.

Nº de puntos por canal	4.000
Frecuencia de adquisición	400 Hz
Rango de adquisición	-2,5 V a 2,5 V
Temperatura del aire	17,5º

Tabla 2. Datos de entrada

En este artículo se ha descrito el proceso de diseño de construcción de un túnel aerodinámico llevado a cabo por los alumnos y profesores de la Universidad de Oviedo, en la Escuela Politécnica de Mieres.

Desde el punto de vista del alumno, este proyecto supone la oportunidad de comprender la necesidad de estudiar la influencia del viento en las estructuras civiles, y desarrollar con ello el conocimiento necesario para investigar en este campo de la mecánica de fluidos. A su vez, la propia construcción de un túnel aerodinámico permite fomentar el aprendizaje concreto sobre este tipo de herramientas de investigación.

5. Referencias

[1] P.J. García Nieto, J.J. del Coz Díaz, D. Castro-Fresno, F. Ballester Muñoz, Numerical simulation of the performance of a snow fence with airfoil snow plates by FVM, J. Comput. Appl. Math. 234 (2010) 1200-1210.

[2] AQUÍ HAY QUE METER ALGÚN PAPER DE EDUARDO, Y ALGUNA REFERENCIA DONDE SE DESCRIBAN LAS CARACTERÍSTICAS DEL TÚNEL ???

[3] A. Navarro Manso, J.J. Del Coz Díaz, D. Fresno Castro, M. C. López Tirados, A. Navarro Bidegain, J M. Simón-Talero, Análisis de pasarela giratoria en la desembocadura del río Nalón mediante Dinámica de Fluidos Computacional apoyada con un Diseño de Experimentos, V Congreso ACHE, Barcelona, España, 25 al 27-10-2011.

[4] J.J. del Coz Díaz, P.J. García Nieto, F.J. Suárez Domínguez, Numerical analysis of pressure field on curved self-weighted metallic roofs due to the wind effect by the FEM, J. Comput. Appl. Math. 192 (1) (2006) 40-50.

[5] J.J. del Coz Díaz, P.J. García Nieto, J.A. González Pérez, A. Martín Navarro, Numerical analysis of the pressure field on curved and open self-weighted metallic roofs due to the wind effect by the finite volume method, Appl. Math. Comput. 209 (1) (2009) 31-41.

2. Congreso internacional de estructuras de la asociación española de ingeniería estructural

Efectos aeroelásticos sobre seguidores solares de un solo eje.

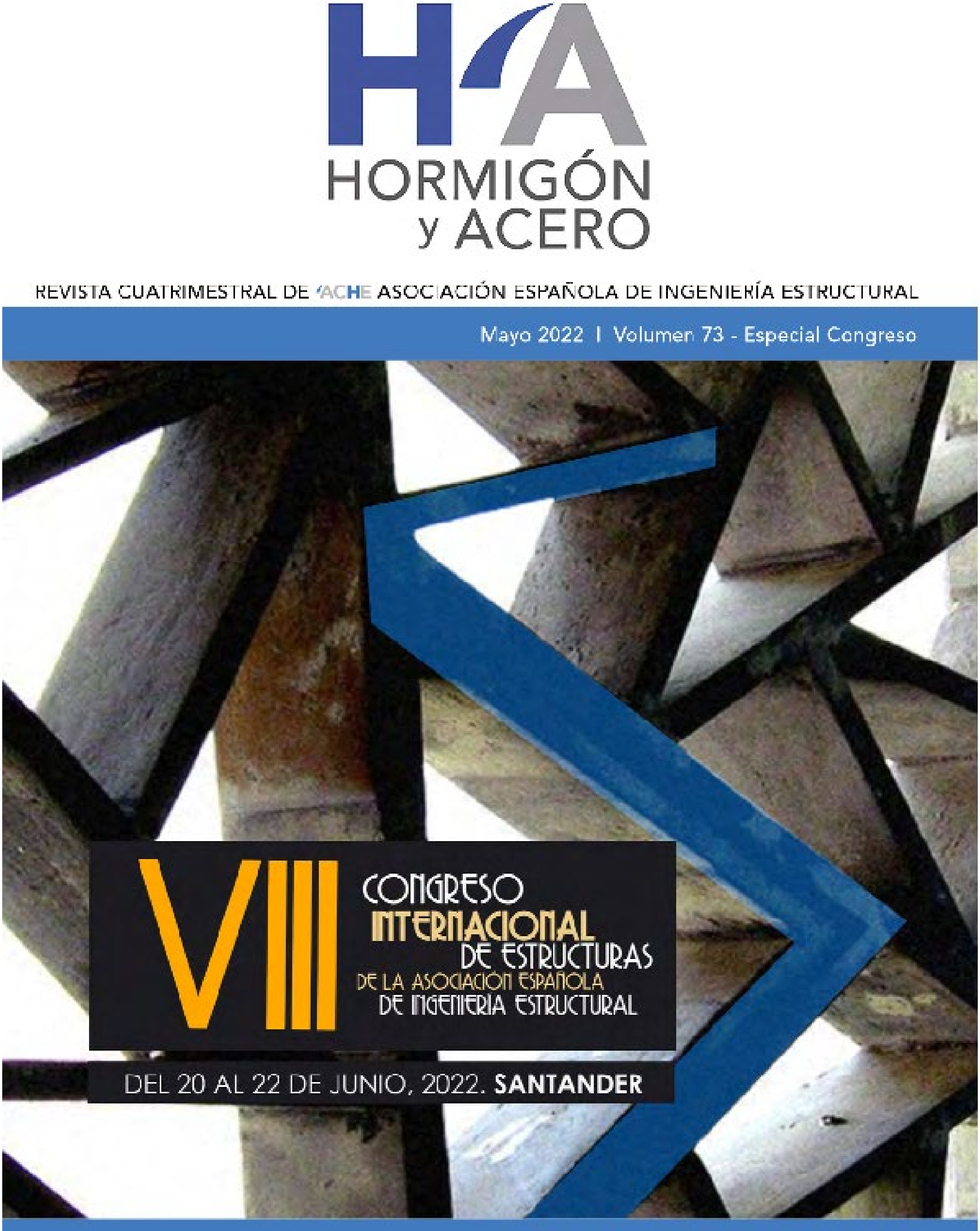

HORMIGÓN
y ACERO

REVISTA CUATRIMESTRAL DE ACHE ASOCIACIÓN ESPAÑOLA DE INGENIERÍA ESTRUCTURAL

Mayo 2022 | Volumen 73 - Especial Congreso

VIII CONGRESO INTERNACIONAL DE ESTRUCTURAS DE LA ASOCIACIÓN ESPAÑOLA DE INGENIERIA ESTRUCTURAL

DEL 20 AL 22 DE JUNIO, 2022. SANTANDER

Cartel ganador del concurso de carteles para el VIII Congreso de ACHE

Disponible en www.hormigonyacero.com
Volumen 73, Especial VIII Congreso ACHE, Junio 2022
https://doi.org/10.33586/hya.2022.SANTANDER

Volumen 73 - Especial Congreso, Junio 2022

SUMARIO | CONTENTS

VIII Congreso Internacional de Estructuras

Congreso de la Asociación Española de Ingeniería Estructural (ACHE)
Santander, 20-22 de junio de 2022

Publicado por Cinter Divulgación Técnica S.L.
E.T.S.I. de Caminos, Canales y Puertos. Laboratorio de Estructuras. Avda. del Profesor Aranguren, s/n. 28040 Madrid
Tel.: (+34) 91 067 41 64 - www.e-ache.com

Efectos aeroelásticos sobre seguidores solares de un solo eje

Aeroelastic phenomena on solar trackers with a single torque tube axe

Eva Martínez García[a], **José Luis Suárez Sierra**[b], **Eduardo Blanco Marigorta**[c], **Antonio Navarro-Manso**[*,d]

[a] Ms. Energy Engineering. Project Manager. Táctica Industrial, S.L. emartinez@tacticaindustrial.com
[b] Assistant Prof. Dr. Mechanical Engineer. CEO. Táctica Industrial, S.L. jlsuarez@tacticaindustrial.com
[c] Full Prof. Dr. Mechanical Engineer. Energy Department. University of Oviedo. eblanco@uniovi.es
[d] Associate Prof. Dr. Civil Engineer. Energy Department. University of Oviedo. navarroantonio@uniovi.es

RESUMEN

Los seguidores solares de un solo grado de libertad (disposición de los paneles de forma longitudinal sobre un tubo a torsión, "torque tube", accionado por un motor en la sección central) han evolucionado a estructuras extremadamente esbeltas, debido a la competitividad y la optimización que el mercado está llevando a cabo. Este artículo profundiza en el conocimiento e identificación de los fenómenos aeroelásticos (la divergencia torsional, las vibraciones inducidas por desprendimiento de vórtices y el galope o flameo torsional, i.e. de un solo grado de libertad) mediante ensayo completo de modelos a escala en túnel aerodinámico.

ABSTRACT

Solar trackers of a single degree of freedom (longitudinally arranged panels on a torque tube, driven by a motor in the central section) have evolved to extremely slender structures, due to competitiveness and optimization that the market is carrying out. This article deepens the knowledge and identification of aeroelastic phenomena (torsional divergence, vibrations induced by vortex shedding and galloping or torsional flutter, i.e. single degree of freedom) by means of a full aeroelastic test of scale models in a wind tunnel.

PALABRAS CLAVE: Galope, Túnel Aerodinámico, Análisis Dimensional, Seguidor Solar Fotovoltaico.
KEYWORDS: Aeroelasticity, Wind Tunnel, Dimensional Analysis, Photovoltaic Solar Tracker.

1. Introducción

La tendencia actual en la captación de energía fotovoltaica es utilizar seguidores solares de un solo grado de libertad, en vez de dos. Esto se consigue, en la práctica, con la disposición de los paneles de forma longitudinal sobre un tubo a torsión ("torque tube"), accionado por un motor en la sección central. De esta forma, se reduce en algo la energía obtenida, pero sigue siendo alrededor de un 30% superior que la obtenida con placas fijas [1].

Debido a la evolución y optimización estructural que el mercado está llevando a cabo, estas instalaciones resultan extremadamente esbeltas; si bien el diseño frente a las cargas estáticas y situaciones accidentales no extremas está correctamente resuelto, es posible que se produzcan inestabilidades aeroelásticas para algunas situaciones particulares [2].

La tipología estructural estos captadores consiste en un tubo empotrado-libre a torsión, de diámetro D, con varios soportes verticales en función de la longitud de los paneles; estos soportes coartan los desplazamientos, no los giros. El captador solar analizado tiene una longitud de L de largo, un ancho b, con un único motor o "driver" en el centro. Cada ala tiene 3 soportes anclados al suelo, de altura h. La Figura 1 muestra las dimensiones y esquema estructural del seguidor solar, con los valores geométricos dispuestos de forma paramétrica (igualmente se hará con los resultados, debido a que los prototipos son propiedad de las diversas empresas del sector energético):

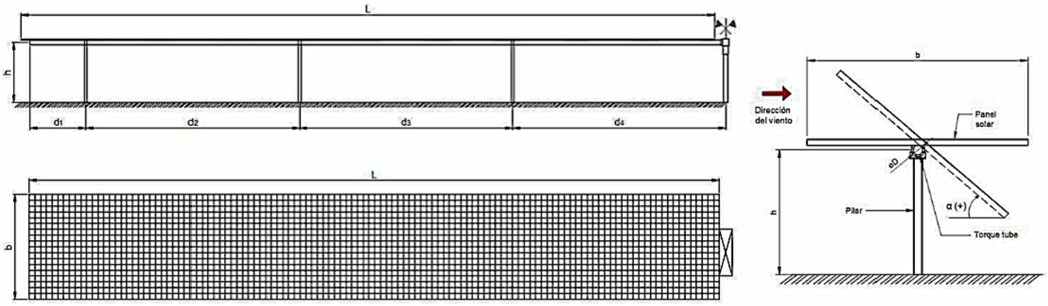

Figura 1. Esquema y dimensiones del seguidor solar.

Así, los fenómenos fluidodinámicos que se pueden esperar son la divergencia torsional, las vibraciones inducidas por desprendimiento de vórtices y el galope o flameo (de un solo grado de libertad) torsional [3, 4]. Se han realizado numerosos estudios sobre placa plana (estática y giratoria) [5], tanto en túnel aerodinámico [6] como con Dinámica Computacional de Fluidos (CFD) [7]. También existen recientes ensayos de campos (al menos, unas cuantas filas) de seguidores solares, con la particularidad de que los modelos son estáticos y se utilizan para estudiar el efecto de la direccionalidad del viento e interferencias entre captadores [6].

Por estos motivos, dado que el estado de la técnica está todavía en una fase inicial con respecto a esta tipología estructural, se ha hecho un análisis inspeccional de la ecuación diferencial del movimiento torsional del eje [8], obteniendo así los parámetros adimensionales descriptivos del fenómeno aerodinámico y estructural. Con ellos se ha desarrollado uno de los primeros modelos aeroelásticos completos [9] a escala reducida y se ha ensayado en un túnel aerodinámico.

2. Objetivos

Los objetivos de la campaña experimental desarrollada en el túnel aerodinámico son los siguientes:

- Análisis dimensional de los modelos a utilizar en los ensayos aeroelásticos de seguidores solares de un solo eje ("tracker").

- Obtención y evaluación de los coeficientes de momento estáticos, en función de la velocidad de viento y del ángulo inicial del "tracker"; teniendo en cuenta la variación no lineal (a lo largo del eje del tubo) del ángulo del panel en cada instante.

- Explicación fenomenológica de los episodios aeroelásticos que causan inestabilidad en la estructura del seguidor solar, determinando las velocidades críticas para cada posición inicial.

- Estudio de medidas correctoras para los seguidores construidos; y establecimiento de criterios de diseño seguros, en términos de velocidad de viento de Proyecto y rigidez de la estructura, para la tipología analizada.

3. Análisis dimensional del fenómeno acoplado fluidodinámico-estructural

A continuación, se identifican las variables que intervienen en el fenómeno acoplado fluido-estructura; y se discute la adimensionalización del mismo para obtener la semejanza geométrica, cinemática y dinámica, requerida para que los ensayos en túnel aerodinámico puedan ser extrapolados al fenómeno real (prototipo) [10].

3.1 Variables

La fuerza aerodinámica tiene dos variables: la magnitud y la frecuencia, dependientes del resto de factores: F [kg·m/s^2], [MLT^{-2}]; f [s^{-1}], [Hz], [T^{-1}]. Las variables debidas al fluido son: densidad, viscosidad y velocidad: ρ [kg/m^3], [ML^{-3}]; μ [kg/(s·m)], [ML^{-1}T^{-1}]; U [m/s], [LT^{-1}]. La principal variable del objeto es la geometría, que, para la semejanza geométrica, se puede reducir a una variable de tamaño. En caso de permanecer estático e indeformable, es la única variable: L [m], [L].

Cuando se trata de un objeto que se mueve, hay que tener en cuenta su inercia, y en el caso de que se deforme, su elasticidad. Para un seguidor solar de un solo eje con deformación por torsión, la inercia viene representada por el momento de inercia con respecto al eje de giro, I, y la deformación por la constante de deformación angular, K ("rigidez", que es función del momento, momento por unidad de giro): I [kg·m^2], [ML^2]; K [N·m/rad], [kg·m^2/s^2], [ML^{2}T^{-2}].

Se ha asumido que el amortiguamiento es pequeño $C << 2\cdot(KI)^{1/2}$, y que no influye en ese rango de valores. Si no fuese así, habría que incluir esta variable. Tampoco se ha considerado la influencia de la turbulencia del aire incidente, lo cual no quiere decir que se esté eliminando, sino simplemente que no se está escalando.

3.2 Números adimensionales

Con las 8 variables (F, f, ρ, μ, U; L; I, K) y 3 dimensiones básicas (M, L, T), se obtienen 5 números adimensionales.

Los números adimensionales típicos para fuerza, frecuencia y viscosidad (F, f, μ) son Euler, Strouhal y Reynolds, que representan, respectivamente, la fuerza sobre la estructura debida al viento, frecuencia de vibración del desprendimiento de vórtices debido al fluido, y la importancia de las fuerzas viscosas frente a las de inercia:

$$E_u = \frac{F}{{}^{1}\!/_{2}\rho U^2 L^2} \tag{1}$$

$$S_t = \frac{fL}{\mathrm{U}} \tag{2}$$

$$R_e = \frac{\rho \mathrm{UL}}{\mu} \tag{3}$$

Para el momento de inercia y la deformación, se pueden elegir la frecuencia reducida f$_r$, función de la frecuencia propia ω (para una barra empotrada-libre a torsión) y la variante del número de Euler para momentos E$_m$, punto de aplicación de la fuerza:

$$f_r = \frac{\omega \mathrm{L}}{\mathrm{U}} = \frac{\pi}{2}\frac{L}{U}\sqrt{{}^{K}\!/_{I}} = \frac{\pi}{2}\frac{L}{U}\sqrt{{}^{GJ}\!/_{LI}} \tag{4}$$

$$E_m = \frac{k}{{}^{1}\!/_{2}\rho U^2 L^3} \tag{5}$$

Los mismos grupos se obtendrían adimensionalizando la ecuación general del movimiento, donde el subíndice c y el superíndice * denotan magnitudes características:

$$\frac{U_c^2}{L_c^2}\frac{I}{K}\frac{d^2\theta}{\mathrm{d}t^{*2}} + \frac{U_c}{L_c}\frac{C}{K}\frac{\mathrm{d}\theta}{\mathrm{d}t^{*}} + \theta = \frac{T}{K} \tag{6}$$

3.3 Parámetros del modelo

En un modelo a escala, el tamaño debería ser lo mayor posible que permita el túnel de viento, mientras no haya efectos de bloqueo, borde, etc.

Así se obtendría L_m/L_p. La velocidad también debería ser lo más alta posible para que los números de Re sean lo más parecidos posible, aunque hay un cierto margen en este aspecto por lo que U_m/U_p queda libre. A partir de la igualdad del número de Euler del momento entre modelo y prototipo E_{mm} y E_{mp}:

$$K_m = K_p \frac{U_m^2 L_m^3}{U_p^2 L_p^3} \tag{7}$$

Igualando f_m y f_p, y substituyendo las K:

$$I_m = I_p \frac{L_m^5}{L_p^5} \tag{8}$$

La constante de torsión K_m del modelo determinará la relación de velocidades. Sin embargo, el momento de inercia está totalmente definido por la escala. En el caso estudiado en este artículo, se han utilizado hasta tres materiales diferentes, uno para el eje de torsión y dos para el panel solar y su estructura de soporte, para conseguir la semejanza total entre modelo y prototipo.

Para el fenómeno que nos ocupa, las oscilaciones del flujo y del objeto están íntimamente relacionadas, por lo que se puede afirmar que el caso analizado es totalmente no estacionario, demostrando los experimentos que se está fuera del rango de aplicación de la teoría cuasi-estática, y con una fuerte componente 3D [11].

4. Túnel aerodinámico y modelos a escala

En este apartado se describirán las características del túnel aerodinámico, la construcción de los modelos a escala y el diseño de los experimentos realizados.

4.1 Equipamiento experimental

Los ensayos se han realizado en el túnel aerodinámico EB40-oWT del Departamento de Energía [12] de la Universidad de Oviedo (Figura 2). Es un túnel de circuito abierto en impulsión, con cámara de ensayo abierta [13]. Las velocidades máximas alcanzan los 35 m/s (potencia nominal del ventilador de 30 kW). Tiene una longitud de 14.25 m con una cámara de ensayo de 0.68 x 0.68 m. La turbulencia del flujo en la cámara de ensayo es del 3%.

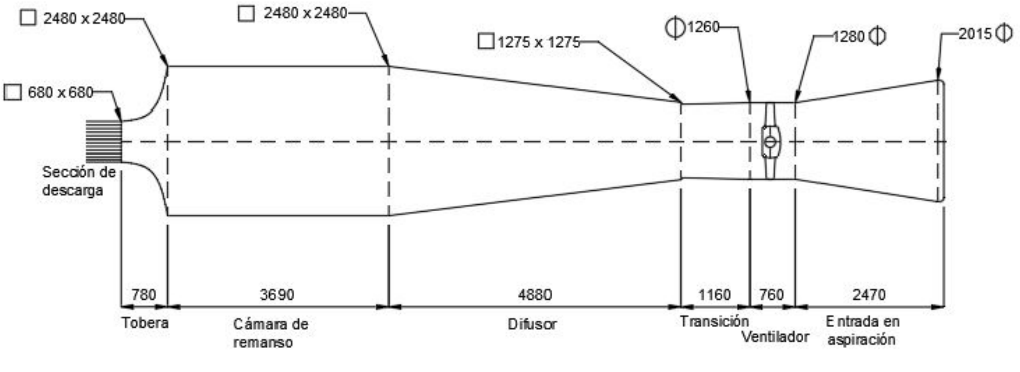

Figura 2. Esquema y dimensiones del túnel aerodinámico EB40-oWT (cotas en mm).

4.2 Modelos

Se presentan aquí los dos modelos finalmente ensayados, cuya única diferencia es que (cumpliendo ambos los criterios de semejanza anteriormente descritos y con valores adimensionales iguales) incorporan varilla de diferente material para la reproducción del "torque tube" (Figura 3).

Para el modelo a escala 1/E utilizado, se imprime para medio "tracker" (en virtud de la simetría) cada marco de panel en 3D, incluidas las correas y grapas de anclaje al "torque tube", materializando la superficie del mismo con unas láminas de cinta adhesiva ultra delgadas, y que permiten llevar los valores de masa e inercia a su correcta escala. Se fabrican dos varillas, una de madera y otra de acero, de área llena, con rigideces muy parecidas, función del diámetro; lo que implica que podremos evaluar la importancia de los amortiguamientos (ξ del 2.2% y 1.0%, respectivamente). Como para la varilla de acero se cumple $\xi_m = \xi_p$ [14], se ha comprobado en los experimentos la escasa influencia del valor de la amortiguación (para valores bajos de amortiguamiento) en las velocidades críticas de disparo de la inestabilidad.

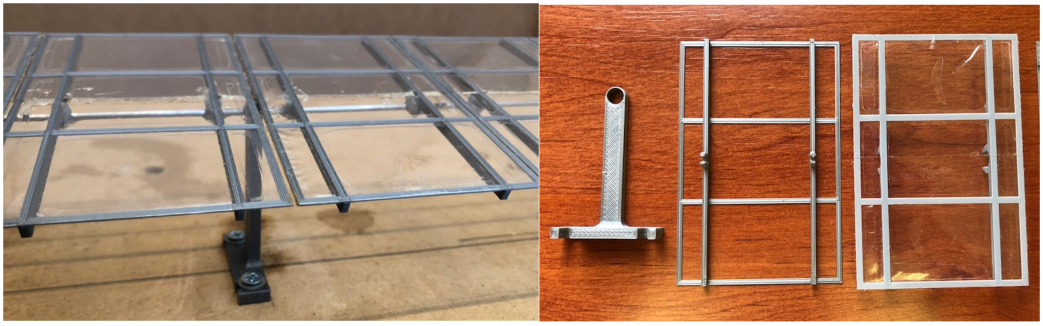

Figura 3. Modelo a escala 1/E y vista de un soporte, un marco y un panel completo.

Los valores de longitud, inercia a torsión y rigidez de cada modelo vienen determinados por el eje, porque la disposición de los paneles no contribuye a dar rigidez a torsión a la estructura; por el contrario, la inercia (masa) del sistema, viene determinada fundamentalmente por la superficie horizontal de los paneles, ya que la masa del tubo es muy pequeña y concentrada en el eje de giro. Se ha considerado un eje medio, ya que la variación en dos tramos de la sección del tubo real no tiene influencia práctica en los valores obtenidos en los ensayos. Y en ambos casos se ha escalado la distancia entre el eje y la superficie del panel.

Las siguientes Tablas 1, y 2 recogen los valores geométricos y mecánicos de los modelos, así como la relación de velocidades entre modelo y prototipo:

Tabla 1. Características de las varillas del modelo.

Material eje	**D (m)**	**L (m)**	**J (m^4)**	**K (G·J/L) ($kg \cdot m^2/s^2$)**	**Masa (kg/m)**	**I ($kg \cdot m^2$)**	**ξ**
Madera	0.006	0.670	1.270E-10	0,180	0.020	6.020E-08	0.022
Acero	0.002	0.670	1.570E-12	0,200	0.025	8.220E-09	0.010

Tabla 2. Características de los paneles del modelo.

Material eje	**Ancho correa (m)**	**Canto correa (m)**	**Hueco panel (m)**	**Masa (kg/m^2)**	**f (Hz)**	**I ($kg \cdot m^2$)**	**U_m/U_p**
Madera	0.002	0.003	0.005	0.525	19.400	2.990E-05	0.550
Acero	0.002	0.003	0.005	0.525	20.500	2.990E-05	0.579

4.3 Metodología experimental

Se realizan varias series de ensayos (3), partiendo el panel de cada posición inicial θ_0; al ir aumentando de forma gradual la velocidad del aire en la cámara de ensayo desde los 1.70 m/s hasta los 35.90 m/s, el modelo comienza a girar (divergencia), con ángulo variable a lo largo del tubo, reproduciendo perfectamente el giro diferencial de cada panel, en función de su distancia a la sección de empotramiento (Figura 4). Este comportamiento es radicalmente diferente al de placa plana con inclinación constante que se describe en toda la literatura [15], y se considera fundamental para la explicación del fenómeno.

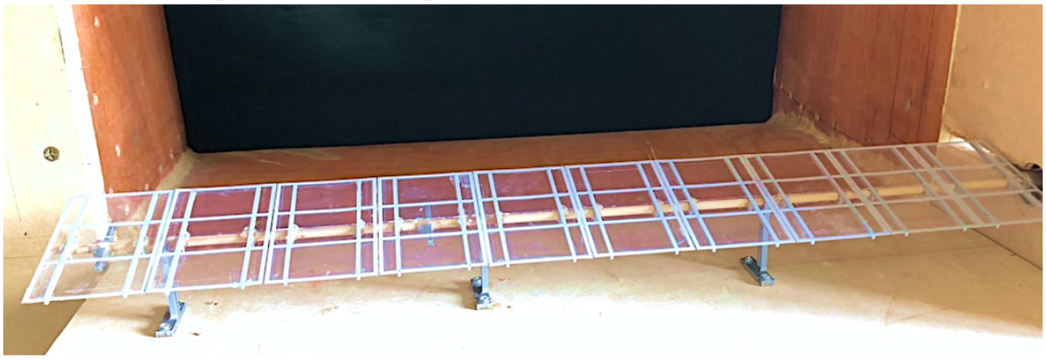

Figura 4. Modelo en la sección de ensayo del túnel aerodinámico.

Se elige como variable de medida el giro total en el extremo libre del panel, así como su amplitud cuando empiezan las oscilaciones. A partir de una determinada velocidad, el seguidor comienza a oscilar a su frecuencia natural (de forma espontánea en la mayoría de los casos analizados o mediante la excitación exterior por medio de una oscilación inicial, en función del ángulo de posicionamiento inicial y del grado de rozamiento del modelo). No hay diferencia de comportamiento ya se suba la velocidad de golpe o gradualmente. Al detener el ventilador del túnel, el modelo recupera bien la deformación por torsión, volviendo a la posición original de partida. Para determinar con la mayor exactitud posible la velocidad crítica, una vez que el seguidor a empezado a oscilar, se disminuye la velocidad de aire en la cámara en escalones muy pequeños (0,07 m/s) hasta que cesa el movimiento. Se considera entonces que esa es la velocidad que provoca la inestabilidad V_{crit}. Así, se tiene seguridad de que para velocidades inferiores - o ángulos superiores a los marcados - no se produce galope, incluso con las peores condiciones de ráfagas o turbulencia.

5. Resultados

Las velocidades en el prototipo han sido calculadas considerando una rigidez K_p N·m/rad, que sería el valor real del seguidor solar analizado.

5.1 Velocidad crítica de galope en función del ángulo de posicionamiento inicial

La Figura 5 muestra el mapa de estabilidad del “tracker”, para todos los ángulos iniciales, expresando las diferentes velocidades críticas adimensionales en función de $V_{crit,mín}$:

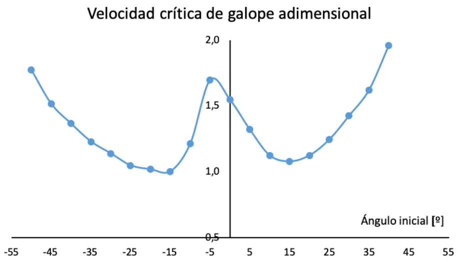

Figura 5. Velocidad crítica de galope.

Por encima de la velocidad crítica, el galope no desaparece una vez establecido, aunque se detecta que puede ser más difícil su incepción, sobre todo para ángulos iniciales grandes. El hecho de que no haya galope por encima de las posiciones indicadas, se puede explicar por la cercanía del borde al suelo (de sotavento y barlovento, respectivamente), que dificulta la alternancia de vórtices de desprendimiento de la capa límite.

5.2 Ángulo girado por el extremo libre en función del ángulo de posicionamiento inicial

El análisis conjunto de los datos de la Figura 6 y de la anterior, sugiere que para que comience el galope del "tracker" hacen falta dos condiciones: un ángulo de giro mínimo en el extremo (θ_{crit}, mínimo=100%) y una velocidad mínima del aire (V_{crit}, mínima=100%).

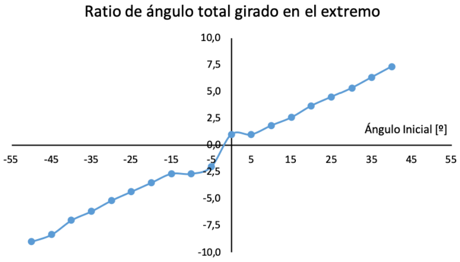

Figura 6. Ángulo total girado a velocidad crítica.

También parece hacer falta una oscilación mínima para que el fenómeno comience, tal y como se ha visto en el apartado anterior. En la práctica, esta oscilación se produciría por desprendimiento de vórtices, ráfagas o turbulencia. En el túnel aerodinámico, con condiciones muy estables, en ocasiones se puede conseguir entrar en la zona de galope sin que se dispare el fenómeno espontáneamente.

Fuera de los ángulos centrales (5º, 0º, -5º y -10º) y de las dos posiciones extremas, el giro de torsión en el extremo del "tracker" es lineal con el ángulo inicial y relativamente pequeño cuando se llega al galope, entre uno y dos grados.

5.3 Coeficiente de momento en función de la velocidad para distintos ángulos iniciales

El coeficiente de momento se ha calculado usando como referencia de dimensión el área del panel (L·b) y la cuerda (b). La Figura 7 muestra los valores medios de C_m para varias posiciones iniciales del seguidor en función de la velocidad de viento, hasta el punto de galope, adimensionalizado con $C_{m,máx}$:

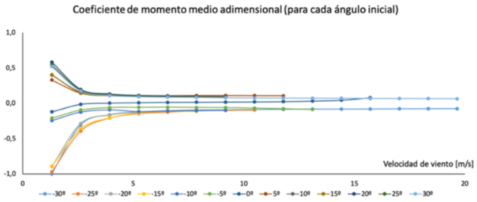

Figura 7. Coeficiente de momento en función de la velocidad de viento.

En la Figura 8 se dibuja el coeficiente de momento medio a la velocidad crítica de galope, para cada posición inicial:

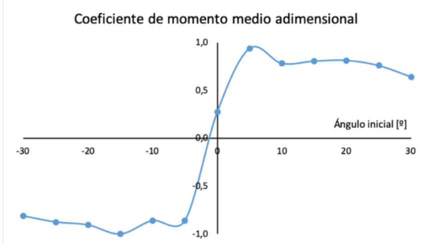

Figura 8. Coeficiente de momento medio para la velocidad crítica de galope.

Para la mayoría de los ángulos iniciales, el valor del coeficiente de momento es bastante constante, a partir de una cierta velocidad del aire. Esto ha resultado sorprendente ya que se esperaba una mayor deformación torsional del "tracker", acompañada de una mayor variación del coeficiente.

Se ha encontrado una influencia importante del rozamiento en los apoyos, sobre todo para valores bajos de la velocidad. Los datos representados aquí son los que se consideran menos afectados por este efecto, de entre todos los modelos que se han ensayado.

Para muchos ángulos iniciales no hay cambio del signo de la pendiente del momento en las proximidades de V_{crit}. Además, en general los ángulos iniciales positivos muestran pendientes negativas, mientras que para los negativos son positivas. Debido a estas consideraciones, se cree que la derivada del coeficiente de momento con respecto al ángulo de ataque no afecta directamente al fenómeno, al menos los valores medios medidos. Se han realizado algunas medidas de momento por encima de las velocidades críticas de galope, sin que se llegara a disparar el galope (debido al rozamiento, como se ha explicado anteriormente). Estos valores fuera de la zona estable parecen continuar con las tendencias de sus respectivas curvas.

Las consideraciones sobre la incepción del fenómeno, y el análisis de los coeficientes de momento descartan que el fenómeno pueda ser explicado por una teoría cuasi-estática. También se ha encontrado que no son aplicables las ecuaciones definidas por el Eurocódigo [16] actualmente.

Como se puede ver en la Figura 7, los ángulos iniciales de 0°, -5° y -10° muestran tendencias que no son totalmente conformes con los otros ángulos, y refuerzan la hipótesis comentada anteriormente.

5.4 Coeficiente de momento en el punto crítico de galope en función del ángulo inicial

Los valores del coeficiente del momento a la V_{crit} (estrictamente hablando, un escalón anterior al disparo del galope) parecen indicar que este valor es relativamente constante, con un valor parecido para ángulos positivos y negativos, aunque con distinto signo, tal y como se observa en la Figura 8, con la salvedad del ángulo inicial de 0°.

5.5 Otras consideraciones

Para intentar retrasar el fenómeno de galope se han tanteado diversas medidas:

- Alerones y bloqueo del flujo entre los soportes, con distintas configuraciones: no se han obtenido resultados eficaces.

- Pantallas aguas arriba del seguidor: la determinación del tamaño mínimo necesario, porosidad y la distancia protegida aguas abajo requeriría un estudio aparte.

- Enclavamientos: se ha demostrado que el bloqueo del giro a torsión en los soportes medio 2 y extremo 3 (especialmente, en el 2), es una medida muy eficaz.

Los efectos del rozamiento y del amortiguamiento (para pequeños valores) no se han cuantificado de forma exhaustiva. Sin embargo, en una prueba puntual y puramente cualitativa, se ha encontrado que amortiguaciones grandes pueden retrasar significativamente la velocidad crítica de galope. Poner valores a este efecto requiere un estudio complementario.

6. Conclusiones

Se ha caracterizado el comportamiento de un seguidor solar de un solo eje horizontal, mediante ensayo en túnel aerodinámico de un modelo completo "full aeroelastic", obteniendo inestabilidad aeroelástica, en este caso, galope torsional.

La inestabilidad se puede producir para la mayoría de las posiciones en el rango de operación del sistema, siendo la estructura susceptible de sufrir oscilaciones catastróficas para dichos ángulos iniciales.

El fenómeno de inestabilidad se originaría debido al desprendimiento de vórtices o a cualquier otra causa que inicie las oscilaciones torsionales del panel, como imperfecciones geométricas, turbulencia atmosférica, ráfagas de viento u otros. En cualquier caso, la estructura no parece sufrir vibraciones inducidas por vórtices (VIV), toda vez que el fenómeno oscilatorio no desparece al aumentar la velocidad, una vez iniciado.

Las oscilaciones se producen a la primera frecuencia natural de la estructura, salvo un caso particular detectado en la posición inicial de -5° en el modelo con varilla de madera (alto rozamiento), en que se detecta una oscilación forzada a una frecuencia menor.

La amplitud de las oscilaciones es creciente con la velocidad, con valores inadmisibles generalmente, para los grados de amortiguamiento estudiados. Se han observado, para algunas posiciones, la aparición de amplitudes variables.

Se ha calculado la velocidad mínima necesaria para que se manifieste inestabilidad en el "tracker", para cada ángulo inicial. Para ángulos fuera del rango marcado, no se detecta inestabilidad de galope torsional.

Se han obtenido los coeficientes de momento estáticos medios, en función de la velocidad de viento y del ángulo inicial del "tracker", así como los ángulos girados en el extremo (divergencia) en el comienzo de la inestabilidad. Se detectan dos comportamientos fenomenológicos claramente diferentes.

Se han analizado, de forma somera, algunas medidas correctoras para los seguidores, con distinto grado de eficacia; así como establecido el valor de una rigidez crítica por encima de la cual no se dispararía la inestabilidad, para una velocidad de viento de Proyecto determinada. No obstante, se necesitan ensayos complementarios para analizar exhaustivamente esta tipología estructural y determinar las medidas correctores más pertinentes, en su caso.

Agradecimientos

Los Autores agradecen de forma especial la colaboración de Francisco José Álvarez González y de Jorge Parrondo Gayo, así como la ayuda recibida del personal de las Áreas de Mecánica de Fluidos y de Ingeniería Hidráulica del Departamento de Energía de la Universidad de Oviedo.

Referencias

[1] R. Bruno, P. Bevilacqua, L. Longo, N. Arcuri, Small Size Single-axis PV Trackers: Control Strategies and System Layout for Energy Optimization, Energy Procedia 82 (2015) 737 – 743.

[2] M. T. L. Browne, DY-WIND, Dynamic Wind Analysis for Solar Trackers, Soltec/RWDI.

[3] M. P. Païdoussis, S. J. Price, E. de Langre, Fluid-Structure Interactions - Cross-Flow-Induced Instabilities, Cambridge University Press, New York, 2011.

[4] R. D. Blevins, Flow-Induced Vibration, Van Nostrand Reinhold, 2nd edition, New York, 1990.

[5] Y. Yang, Experimental Investigations of Vortex Induced Vibration of a Flat Plate in Pitch Oscillation, MSc. Thesis, Texas A&M University, December, 2010.

[6] K. Strobel, D. Banks, Effects of Vortex Shedding in Arrays of Long Inclined Flat Plates and Ramifications for Ground-Mounted Photovoltaic Arrays, J. Wind Eng. Ind. Aerodyn. 133 (2014) 146–149.

[7] C. M. Jubayer, H. Hangan, Numerical Simulation of Wind Effects on a Stand-Alone Ground Mounted Photovoltaic (PV) System, J. Wind Eng. Ind. Aerodyn. 134 (2014) 56–

64.

[8] C. Rohr, P. A. Bourke, D. Banks, Torsional Instability of Single-Axis Solar Tracking Systems, ICWE14, Porto Alegre, Brasil, Junio de 2015.

[9] A. Roedel, S. Upfill-Brown, Designing For The Wind, Using Dynamic Wind Analysis And Protective Stow Strategies To Lower Solar Tracker Lifetime Costs, Nextracker Whitepaper, MKT-000073, 2018.

[10] N. Isyumov et Al., Wind Tunnel Studies of Buildings and Structures, ASCE Manuals and Reports on Engineering Practice, N 67, Virginia, 1999.

[11] N. Nikitas, J.H.G. Macdonald, Misconceptions and Generalizations of the Den Hartog Galloping Criterion, Journal of Engineering Mechanics, 140 (4) (2014).

[12] A. Navarro Manso et Al. Enhancing Civil Aerodynamics Learning: Solar Panel Testing Carried Out in a Wind Tunnel, III International Conference Learning of Structural Engineering, ACHE, Valencia, España, 2013. ISBN 978-84-89670-77-8.

[13] M. Rodríguez Lastra, J. M. Fernández Oro, M. Galdo Vega, E. Blanco Marigorta, C. Santolaria Morros, Novel Design and Experimental Validation of a Contraction Nozzle for Aerodynamic Measurements in a Subsonic Wind Tunnel, Journal of Wind Engineering and Industrial Aerodynamics, 118, (2013), 35–43

[14] Y. Ge, J. Xia, L. Zhao, S. Zhao, Full Aeroelastic Model Testing for Examining Wind-Induced Vibration of a 5,000 m Spanned Suspension Bridge, Frontiers on Build Environment. doi: 10.3389/fbuil.2018.00020 (2018).

[15] X. Xia, K. Mohseni, Lift Evaluation of a 2D Flapping Flat Plate, Phys. Fluids. 25 (9), 091901 (2013).

[16] Eurocódigo 1, Bases de Proyecto y Acciones en Estructuras, Parte 2-4: Acciones en Estructuras. Acciones del Viento, UNE-ENV 1991-2-4, AENOR, España, 2018.

3. 12th international conference on flow-induced vibration

Dimensioning of a solar tracker torque tube for torsional galloping

12th International Conference on Flow-Induced Vibration

Charbel Habchi, Pierre Moussou, Laurent Zimmer

To cite this version:

Charbel Habchi, Pierre Moussou, Laurent Zimmer. 12th International Conference on Flow-Induced Vibration. 2022. hal-03715702v2

HAL Id: hal-03715702

https://hal.science/hal-03715702v2

Submitted on 9 Nov 2022 (v2), last revised 29 Feb 2024 (v3)

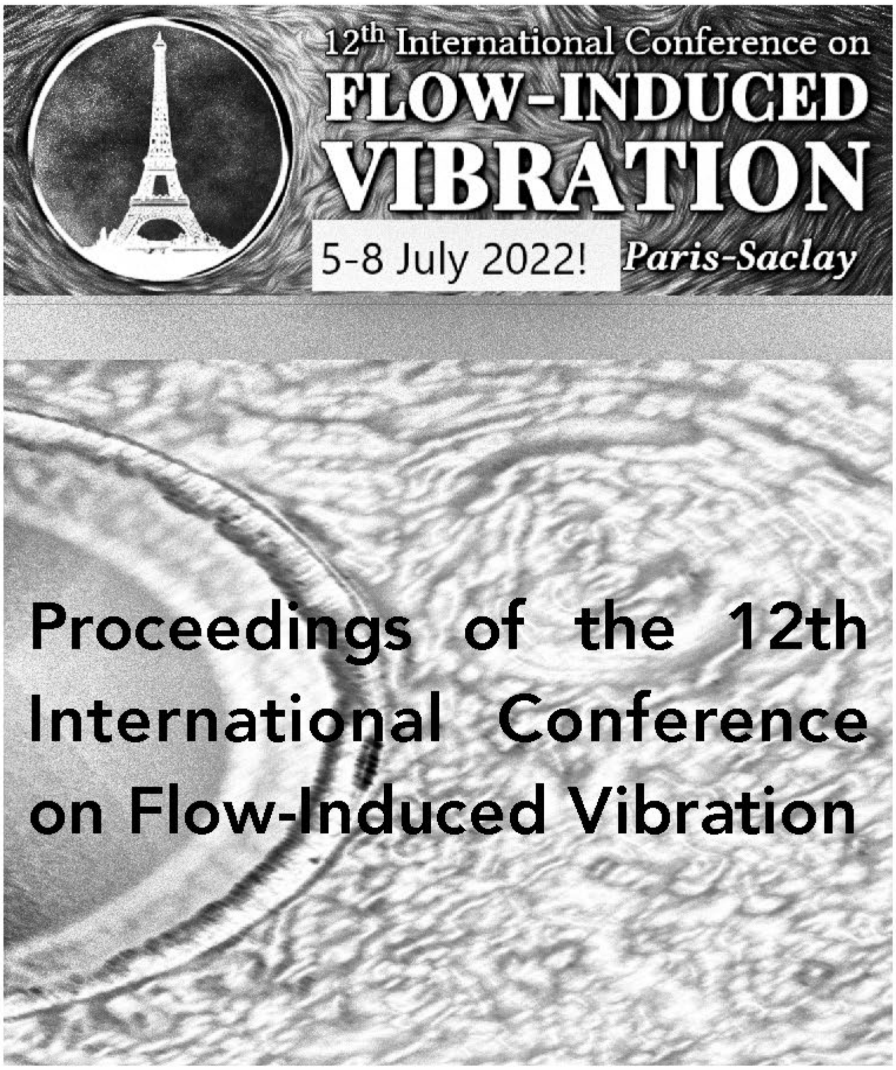

12th International Conference on

FLOW-INDUCED VIBRATION

5-8 July 2022! Paris-Saclay

Proceedings of the 12th International Conference on Flow-Induced Vibration

Table of contents

DIMENSIONING OF A SOLAR TRACKER TORQUE TUBE FOR TORSIONAL GALLOPING

Eva Martínez García
Energy Department. University of Oviedo, Asturias, Spain
Eduardo Blanco Marigorta
Energy Department. University of Oviedo, Asturias, Spain
Jorge Parrondo Gayo
Energy Department. University of Oviedo, Asturias, Spain
Antonio Navarro Manso
Energy Department. University of Oviedo, Asturias, Spain

ABSTRACT

Solar trackers with a single axis (longitudinally arranged panels on a torque tube, driven by a motor in the central section) have evolved to extremely slender structures, due to the competitiveness and optimization that the market is carrying out. In the present work, an analytical and experimental approach has been developed about the aeroelastic phenomena found in these solar trackers with one degree of freedom. On the one hand, the analytical study has identified the dimensionless parameters governing the differential equation of movement. On the other hand, systematic wind tunnel experiments have been carried out with a 3D full aeroelastic scale model. It has been found that the tests reproduce correctly the aeroelastic phenomena found on a real situation. The main result has been the critical galloping velocity for every tilt angle, and a calculation methodology for the solar tracker shaft.

1. INTRODUCTION

Nowadays the trend for increasing profits on solar photovoltaic energy is the use of single axis solar trackers with one degree of freedom. The design of these trackers places the solar panels longitudinally on a tube ("torque tube"), driven by a motor in the central section. This system makes possible the orientation of the azimuth but not the altitude. Although the energy obtained is smaller than with a two degree of freedom solar tracker, is still a 30% higher than the obtained with fixed solar panels (Bruno et.al, 2015).

The structural typology of these solar trackers consists on several solar panels distributed longitudinally over a torsional axis. The shaft is supported by several pillars that allow only the rotational movement. One end of the shaft is free, and the other is fixed to a gearmotor (driver) in charge of angular positioning. Usually, these structures are in a symmetrical arrangement with a row of panels on each side of the driver. Figure 1, shows an example of the structural scheme and dimensions of this kind of solar tracker.

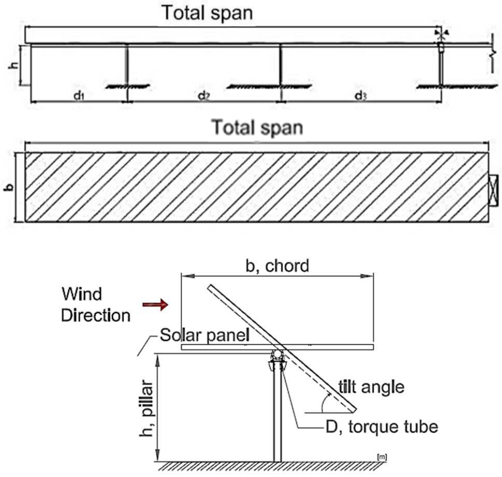

Figure 1. Scheme of single axis solar tracker.

Due to the evolution and mechanical optimization that the market is carrying out, these structures are extremely slender; although the design against static loads and non-extreme accidental situations is correctly solved, aeroelastic instability may occur for some particular situations (Zachary et al, 2020).

Figure 2. Single axis solar tracker facilities collapse (Source: www.pv-magazine-australia.com).

The failures occurring all over the world during the last years are attributed to torsional galloping, flutter or torsional divergence. The components most commonly subjected to fatigue and collapse are the positioning motor, the driver supports and the main axis. Although usually, this also means the panels destruction (Figure 2).

Basic aeroelastic effects (Païdoussis et.al, 2011) (Blevins, 1990) are normally covered by current construction standards (Dyrbye et al, 1997), however, it is increasingly clear that they do not consider the specific effects of wind on single-axis solar trackers. For the correct calculation of these structures, a deeper understanding of the aeroelastic phenomenon is necessary, usually based or complemented with wind tunnel tests (Zachary et al, 2020). Along this line, this work develops a method of analysis and calculation that allows to determine the necessary resistance of the structure to avoid the failures due to these phenomena.

During the experimental test, it could be expected to find aeroelastic phenomena such as induced vibrations by vortex shedding, torsional galloping and flutter. The torsional galloping is a kind of flow-induced oscillation instability with one degree of freedom. Many studies on flat plate aerodynamics have been done, for instance analytical studies on single degree of freedom models (Yang, 2010). There is also experimental aerodynamic tunnel (Strobel et.al, 2014) and Computational Fluid Dynamics, CFD (Jubayer et.al, 2014) researches, including tests of single and complete solar photovoltaic fields of solar trackers. The latter, have been usually made with static models and study the effect of wind directionality and the interferences between different rows of trackers. Only a few of these investigations have also developed full aeroelastic tests (Roedel et.al, 2018).

As the state of the technique is still in a young phase (Rohr et al, 2015), regarding this structural typology, in this research an inspectional analysis of the differential equation of the axis torsional motion has been done, obtaining the descriptive dimensionless parameters for the aerodynamic and structural phenomena. Based on these analyses full scaled aeroelastic models have been developed and tested in an aerodynamic wind tunnel.

The experimental campaign was focused on the following objectives:

- Phenomenological explanation of the aeroelastic phenomena causing instability in the solar tracker structure.
- Finding out the critical velocities for different tilt angles.
- Developing of a safe design criterion in terms of project wind velocities and rigidity of the structure, for the analyzed case.

2. NON-DIMENSIONAL ANALYSIS

In this specific case, for the dimensionless analysis it is necessary to take in account nine variables. Three of them, correspond to the fluid: velocity, density and viscosity (U, ρ, μ). Four are related to the structure: characteristic length (L), typically span or chord), torsional stiffness (K); moment of inertia with respect to the axis (I); and structural damping (c). The last variables arise from the aerodynamic forces, which in this case can be reduced to the torque magnitude (T), and frequency (ω).

From the relationship between the variables corresponding to the fluid and aerodynamic forces, come up the typical dimensionless numbers of Euler (C_m), in this case as the moment coefficient), Strouhal (St) and Reynolds (Re).

$$C_m = \frac{T}{\frac{1}{2}\rho U^2 L^3} \tag{1}$$

$$S_t = \frac{\omega L}{U} \tag{2}$$

$$R_e = \frac{\rho UL}{\mu} \tag{3}$$

On the other hand, these numbers related to the properties of the structure derive from the equation of torsional motion of the structure:

$$I\frac{d^2\theta}{dt^2} + c\frac{d\theta}{dt} + K\theta = T \tag{4}$$

These numbers are, first the torsional stiffness coefficient (C_k):

$$C_K = \frac{K}{1/_2\,\rho U^2 L^3} \tag{5}$$

Second, the reduced frequency (ωr), which has the same structure than St but relating to the natural frequency of the structure instead of the aerodynamic phenomenon frequency.

$$\omega_r = \frac{\pi}{2}\frac{L}{U}\sqrt{K/I} \qquad (6)$$

And finally, the damping ratio (ξ), corresponding to the relationship between structural and critical damping:

$$\xi = \frac{c}{\sqrt{2(KI)}} \qquad (7)$$

Typically, using these groups, the aerodynamic forces can be expressed as St and Cm as a function of the other four:

$$C_m = (Re, C_K, \omega_r, \xi) \qquad (8)$$

$$St = (Re, C_K, \omega_r, \xi) \qquad (9)$$

Thus, if a scale model maintains these four dimensionless numbers, is possible to achieve the similarity of the aerodynamical phenomenon.

Regarding the scaled model for wind tunnel tests, as usual in many of these cases, the Reynolds number is not compatible with the other dimensionless groups. However, in this specific case, the most important aerodynamic effects are generated by vortex shedding of bluff body separation instead of boundary layer detachment. Because of this, the Reynolds number influence is expected to be smaller for fully developed turbulent flows.

In other to preserve the dimensionless numbers Ck, ωn and ξ when making the scale model, it is necessary to maintain the damping ratio between model and prototype, usually through the mechanical properties of the materials.

$$\xi_m = \xi_p \qquad (10)$$

And there is also a fixed relationship between the model and prototype inertia, determined by the scale.

$$I_m = I_p\left(\frac{L_m}{L_p}\right)^5 \qquad (11)$$

However, for the torsional stiffness coefficient, (Ck), the relation obtained from the prototype is:

$$K_m = K_p\left(\frac{U_m}{U_p}\right)^2\left(\frac{L_m}{L_p}\right)^3 \qquad (12)$$

In this way, there is a certain freedom between the scale and the torsional stiffness ratio in the model and prototype. Which also, allows to use different stiffness in the materials to adjust the velocities at which the aerodynamic phenomena occur in the wind tunnel.

3. EXPERIMENTAL METHODOLOGY

The experimental tests were developed in the aerodynamic wind tunnel, named EB40-Owt, at the Energy Department of the University of Oviedo (based on Rodríguez Lastra et. al, 2013). It has a maximum velocity of 35 m/s, nominal power of 30 kW; 14.25 m length and a test section of 0.7 x 0.7 m; the turbulence is below 3% at the test chamber.

The single axis solar tracker prototype studied has the basic morphology of this kind of structures, with the features indicated in the table 1.

Description	Value
Tracker shaft length [m]	30
Shaft diameter [m]	0.210
Shaft thickness [mm]	6
Shaft stiffness [Nm]	113450
Inertia [kg·m²]	1668
Panel chord [m]	3
Panel thickness [m]	0.0135

Table 1. Prototype solar tracker dimensions.

In this kind of solar trackers, damping ratios are low and correspond to the natural value of the materials, mostly of the shaft. The torsion values of the structure are determined only by the shaft because the panel's stiffness has little influence on this property of the structure. However, the inertia of the system comes determined by the panels surface because the shaft mass is small and concentrated on the axis. The solar tracker is supported by four pillars and the height from the torsional axis respect to the floor is 20% bigger than half of the panel chord.

Taking advantage of the symmetry of the solar tracker, the experimental model represents only half of the structure from the driver (fixed end) to the free end. In order to take full advantage of the test section, the scale is 1/45, meaning a blockage below 7 or 8% in any azimuthal position. Figure 3 show the experimental model installed on the open test section.

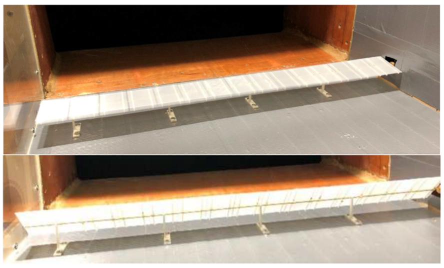

Figure 3. Full aeroelastic scale model.

The model has been built mostly with PLA material, using additive manufacturing technologies. In the case of model's shaft, two materials were chosen: steel and brass, in order to study the influence of the torsional stiffness in the critical velocity. Table 2 contains detailed information of the complete model.

Description	Value
Tracker shaft length [m]	0.67
Panel chord [m]	0.067
Support height [m]	0.04
Purlin thickness [m]	0.003

Table 2. Solar tracker model: panels and supports main features.

Two different models have been built for evaluation on the wind tunnel. Both have the same features except for the torsional stiffness of their shaft since one is made of steel, with K=0.092 Nm, and the other of brass with a K= 0.2 Nm. Table 3 collects the properties of the models based on the type of shaft.

Concept	Brass	Steel
K[Nm]	0.092	0.200
I [kg·m²]	9.02e-6	9.02e-6
ξ[%]	1.6	2.4
ω_n[Hz]	25.3	37.2

Table 3. Principal features of the models.

Several impact tests have been performed to obtain the natural frequency of the structure and its damping ratio. One of the test temporal signal is represented on figure 4, in which the logarithmic decrement of the moment on the driver can be appreciated

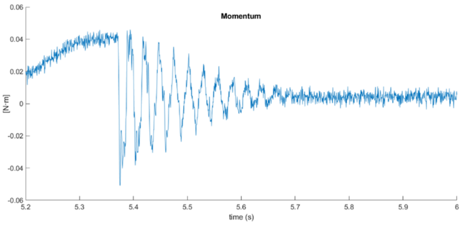

Figure 4. Time signal of the impact test. Moment at the driver.

A frequency analysis of an impact test signal can be seen in the figure 5. The first peak at 37 Hz corresponds the main natural frequency of the structure with the steel shaft. The second peak about 110 Hz, corresponds to the third harmonic and there are also smaller excitations at higher frequencies, representing higher order harmonics and other less important vibration modes.

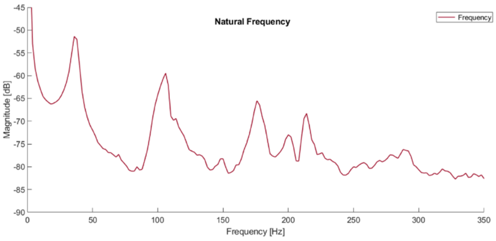

Figure 5. Frequency analysis of the impact test.

Because inertia of the structure is distributed along the axis, the natural frequencies of the vibration correspond to the expression (Rao, S.S., 2007):

$$\omega_n = \frac{(2n+1)\pi}{2}\sqrt{\frac{K}{I}} \qquad (13)$$

The experimental procedure consists on setting the solar tracker on a determined tilt angle (solar azimuthal orientation) and test increasing speeds until the instabilities are found. The tested azimuthal angles range from +75° degrees to -75°.

4. EXPERIMENTAL RESULTS-

In the different models tested, as the velocity increases, small vibrations can be observed, due to the inflow turbulence. These oscillations are somewhat random, but in any case they involve only small amplitudes. Nevertheless, a much more intense vibration develops from a certain velocity upwards. Figures 6 and 7.

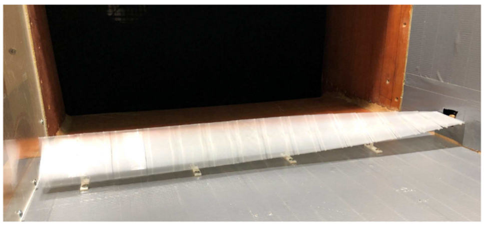

Figure 6. Non-linear deformation of structure - torsional galloping

Figure 7. Maximum deformation angle of the structure on the free end.

Essentially, the oscillation occurs centered in the original azimuthal angle and it is caused by the torsional moment because of the vortex shedding on the leading and trailing edges. Figure 8 represents the numerical simulation of this phenomenon where vortex shedding on the leading edge is stronger and seems to be the main factor in the phenomenon (Rohr et al, 2015).

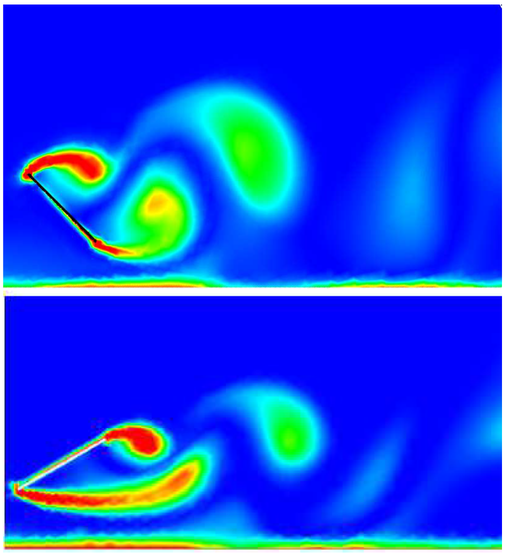

Figure 8. Numerical simulation of the torsional galloping (contours of vorticity).

Once the phenomenon begins, the oscillation frequency corresponds to the structural natural frequency not changing with the velocity increase. With a higher velocity, the oscillation doesn't disappear and its amplitude and strength seems to be amplified up to the collapse of the structure. This fact allows to discard that the phenomenon is a vortex induced vibration (VIV).

From a structural perspective, torsional divergence (TD) is also discarded because this divergence is mainly a steady state phenomenon. Another reason is that regarding the specific bibliography of flat plates twisting on their axis, it is noted that torsional moment decreases inversely to the tilt angle, reaching zero on the vertical position (Meseguer et.al, 2013). Hence, these structures topology does not seem to be susceptible to suffer this kind of instability.

Actually, based on the tests findings, the present instability has been identified as torsional galloping, or one degree of freedom flutter (Scannlan, H.R, 1986).

The amplitude of the oscillation varies along the axis of the solar tracker from zero at the driver side to its maximum value at the free end, producing a longitudinal sinusoidal twist of the panel (in contrast with a linear distribution when the momentum is concentrated on the free end), see figure 9.

As commented before, in the beginning of the oscillation the amplitude is small, and when the velocity increases the amplitude intensifies exponentially. If the solar tracker is maintained in the range of oscillations of small amplitude, fatigue effects may appear in the structure. However, with a small increase in the wind velocity, larger amplitudes will appear, generating loads on the structure (much higher than the static loads usually considered), and the solar tracker can reach structural collapse.

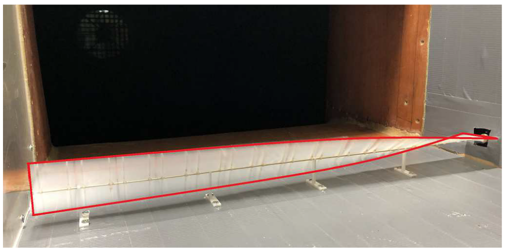

Figure 9. Full aeroelastic model torsional galloping.

For this investigation, the most important part of the wind tunnel tests is the definition of the critical velocity at which the torsional galloping phenomenon appears. This velocity depends on the azimuthal position angle of the solar tracker. Figure 10 illustrates these values expressed as non-dimensional reduced velocity.

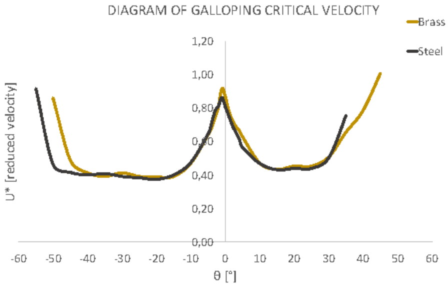

Figure 10. Evolution of reduced critical velocity as a function of the azimuthal angles.

The reduced velocity corresponds to the wind speed adimensionalized by the chord and natural frequency.

$$U^* = \frac{U}{b}\frac{\pi}{2}\sqrt{\frac{K}{I}} \tag{14}$$

The oscillation phenomenon does not appear on every azimuthal angle, it is restricted between approximately +50° and -55° degrees. The minimum critical velocities show up in the range of -45° to -15° and from 20° to 40°, this velocity is more or less uniform in these ranges; and it has a value of 0.37 on the negative side and 0.43 for the positive one. For azimuthal angles closed to zero, the critical velocities are higher, up to 0.86 for an angle of -1°. The maximum value is not zero centered due to the asymmetry induced by the ground. The critical velocities also increase at the extremal angles (± 50°), where the phenomenon disappears.

The plot behavior shows several aspects of the phenomenon:

1) Considering the stable velocity on the angles ranging from -45° to -15° and from 20° to 40°, it seems to indicate that it is necessary a certain kinetic energy for the oscillatory phenomenon to develop.

2) At small tilt angles, between -10° and +5° approximately, the critical velocity is considerably higher. It is known that a flat plate with small angles of inclination does not shows the vortex shedding phenomenon (Robert Blevins, 2003). However, due to the structure flexibility, when the velocity grows, the angle of the free end deviates with respect to the driver end; the higher the velocity, the higher the difference. For example, if the azimuthal position of the model solar tracker is 5°, when the wind velocity is 15 m/s, the free end angle is around 8°or 9°. What it means is that vortex shedding can be triggered on the free end with a velocity high enough. If this velocity is sufficient for the necessary kinetic energy, the tracker will then go into the torsional galloping phenomenon.

3) When the absolute value of the azimuthal angles is high enough, the torsional galloping phenomenon does not activate. It is possible that the flow detachment at the leading or trailing edge close to the ground is much less energetic and is not sufficient to develop the instability. Or perhaps, the lack of symmetry makes more difficult the beginning of the instability.

Another aspect of the experimental results is that the values for the critical reduced velocity are basically the same on the two tested models in spite of the difference of the shaft's torsional stiffness (K). In fact, this is a consequence of the fact that the expression used for reduced velocity maintains the dimensionless torsional stiffness coefficient (C_k). In other words, two test with the same reduced velocity keep the similarity (with respect to the stiffness).

Only models with the same value of moment of inertia (I) have been tested, so it is still unknown its possible effect on the galloping critical velocity.

The damping ratio (ξ) values in both models are rather different but both are also quite small. Although not included in this work, other tests with different materials have been inchoated, and the preliminary results corroborate the idea that, when the damping ratio is small, it has little influence on the onset of torsional galloping.

5. SHAFT DIMENSIONING

This previous analysis and experimental results allows to calculate the maximum wind velocity that a determined prototype of solar tracker will stand before the onset of the torsional galloping.

For instance, for the prototype of solar tracker in this study, if the threshold value of the reduced critical velocity is set at 0.37, the galloping critical velocity is:

$$U_{cr} = U_{cr}^* \cdot \frac{b \cdot \pi}{2} \cdot \sqrt{\frac{K}{I}} \approx 14.4\ m/s \tag{15}$$

Alternatively, it is also possible to calculate the shaft stiffness for a specified critical galloping velocity or maximum project wind speed, for example, for 100 km/h:

$$K_{cr} = \frac{U_{cr}^2}{U_{cr}^{*2}}\frac{4I}{L^2\pi^2} = \approx\ 420998\,Nm \tag{16}$$

Which corresponds to a shaft thickness of 33 mm, instead of 6 mm of the original prototype.

Normally, operation procedure in a photovoltaic facility calls for the solar tracker to assume a stow position when the wind is above a certain value; usually zero or a slightly negative tilt angle. In this case, the reduced critical velocity can reach a value around 0.8. This corresponds to a galloping critical velocity of 31.13 m/s, for the original prototype, or for a shaft thickness of 5 mm to withstand up to 100 km/h.

6. CONCLUSIONS

An analytical and experimental analysis of the aeroelastic instabilities of single axis solar trackers has been carried out. The analytical procedure has identified an evaluated the dimensionless variables related to the phenomenon. Based on this study, a scaled experimental model has been developed and tested in a wind tunnel. The model has been able to reproduce the phenomenon of torsional galloping that shows up when wind velocities reach relatively high values. The results show that in order for torsional galloping to appear, it is necessary, on the one hand, that the azimuthal angle of the solar tracker be adequate for the vortex shedding condition and, on the other hand, that the flow contains the necessary kinetic energy.

The measurements have identified the galloping critical velocities for the whole range of azimuthal positions. It has been found that the stable value of the reduced critical velocities, have a minimum on the entire range which can be used as a threshold. These velocities are higher when close to horizontal angles. In addition, there is a certain positive and negative angle, from which the instability no longer develops. The threshold value of the reduced critical velocity has been used to determine the wind speed at which the aeroelastic instabilities begin to develop and the necessary shaft thickness for a given project wind speed.

7. ACKNOWLEDGEMENTS

This research has been developed in the framework of the FC-GRUPIN- IDI/2018/000205 project, supported by the Principado de Asturias – Plan de Ciencia, Tecnología e Innovación-, co-financed by FEDER funds.

8. REFERENCES

Blevins, R. D., 1990, Flow-Induced Vibration, Van Nostrand Reinhold, 2nd edition, New York.

Bruno, R., Bevilacqua, P., Longo, L., Arcuri, N, 2015, Small Size Single-axis PV Trackers: Control and System Layout for Energy Optimization, Energy Procedia 82: 737 – 743.

Dyrbye, C. and Hansen, S. O., 1997, Wind Loads on Structures, John Wiley and Sons, Chichester (UK). ISBN: 978-0-471-95651-8.

Jubayer, C. M., Hangan, H., 2014, Numerical Simulation of Wind Effects on a Stand-Alone Ground Mounted Photovoltaic (PV) System, J. Wind Eng. Ind. Aerodyn., 134: 56–64.

Païdoussis, M. P., Price, S. J., De Langre, E., 2011, Fluid-Structure Interactions - Cross-Flow-Induced Instabilities, Cambridge University Press, New York.

Rao, S.S. Vibration of Continuous Systems, 2007, John Wiley & Sons, Inc. New Jersey.

Rodríguez Lastra, M., Fernández Oro, J. M., Galdo Vega, M., Blanco Marigorta, E., Santolaria Morros, C., 2013, Novel Design and Experimental Validation of a Contraction Nozzle for Aerodynamic Measurements in a Subsonic Wind Tunnel, Journal of Wind Engineering and Industrial Aerodynamics, 118: 35–43.

Roedel, A., Upfill-Brown, S., 2018, Designing for The Wind, Using Dynamic Wind Analysis and Protective Stow Strategies to Lower Solar Tracker Lifetime Costs, Nextracker Whitepaper, MKT-000073.

Rohr, C., Bourke, P. A., Banks, D., 2015, Torsional Instability of Single-Axis Solar Tracking Systems, ICWE14, Porto Alegre, Brazil.

Scannlan R.H.; Simiu E.; 1986, Wind Effects on Structures, John Wiley&Sons,Inc.

Strobel, K., Banks, D., 2014, Effects of Vortex Shedding in Arrays of Long Inclined Flat Plates and Ramifications for Ground-Mounted Photovoltaic Arrays, J. Wind Eng. Ind. Aerodyn., 133: 146–149.

Yang, Y., 2010, Experimental Investigations of Vortex Induced Vibration of a Flat Plate in Pitch Oscillation, MSc. Thesis, Texas A&M University.

Zachary, J.Taylor; Mathew, T.L. Browne., 2020. Hybrid pressure integration and buffeting analysis for multi-row wind loading in an array of single axis trackers. Journal of Wind engineering and Industrial Aerodynamics, 197:104056.